Light Management for Silicon and Perovskite Tandem Solar Cells

by

Salman Manzoor

A Thesis Presented in Partial Fulfillment
of the Requirements for the Degree
Doctor of Philosophy

Approved October 2019 by the
Graduate Supervisory Committee:

Zachary Holman, Chair
Richard King
Michael Goryll
Yuji Zhao

ARIZONA STATE UNIVERSITY

December 2019

ABSTRACT

The emergence of perovskite and practical efficiency limit to silicon solar cells has opened door for perovskite and silicon based tandems with the possibility to achieve >30% efficiency. However, there are material and optical challenges that have to be overcome for the success of these tandems. In this work the aim is to understand and improve the light management issues in silicon and perovskite based tandems through comprehensive optical modeling and simulation of current state of the art tandems and by characterizing the optical properties of new top and bottom cell materials. Moreover, to propose practical solutions to mitigate some of the optical losses.

Highest efficiency single-junction silicon and bottom silicon sub-cell in silicon based tandems employ monocrystalline silicon wafer textured with random pyramids. Therefore, the light trapping performance of random pyramids in silicon solar cells is established. An accurate three-dimensional height map of random pyramids is captured and ray-traced to record the angular distribution of light inside the wafer which shows random pyramids trap light as well as Lambertian scatterer.

Second, the problem of front-surface reflectance common to all modules, planar solar cells and to silicon and perovskite based tandems is dealt. A nano-imprint lithography procedure is developed to fabricate polydimethylsiloxane (PDMS) scattering layer carrying random pyramids that effectively reduces the reflectance. Results show it increased the efficiency of planar semi-transparent perovskite solar cell by 10.6% relative.

Next a detailed assessment of light-management in practical two-terminal perovskite/silicon and perovskite/perovskite tandems is performed to quantify reflectance, parasitic and light-trapping losses. For this first a methodology based on spectroscopic

ellipsometry is developed to characterize new absorber materials employed in tandems. Characterized materials include wide-bandgap ($CH_3NH_3I_3$, $Cs_yFA_{1-y}Pb(Br_xI_{1-x})_3$) and low-bandgap ($Cs_{0.05}FA_{0.5}MA_{0.45}(Pb_{0.5}Sn_{0.5})I_3$) perovskites and wide-bandgap CdTe alloys (CdZnSeTe). Using this information rigorous optical modeling of two-terminal perovskite/silicon and perovskite/perovskite tandems with varying light management schemes is performed. Thus providing a guideline for further development.

DEDICATION

I dedicate my dissertation work to my family, friends and teachers. Especially to my parents, for their unconditional love and encouragement. Also to my siblings, for their belief in my abilities, for their support and love.

Lastly, I would like to dedicate this dissertation to my Lord and Saviour Jesus Christ.

ACKNOWLEDGMENTS

I would like to express my deepest appreciation to my advisor, Prof. Zachary Holman, for his guidance and unwavering support but above all for his endless patience with me throughout my time in Holman research group. I also sincerely thank him for inspiring me to strive for excellence and for giving me many opportunities to attend research conferences to further my knowledge. Importantly, I am grateful to him for teaching me to choose important and practical research problems.

Next I would like to extend my gratitude to Dr. Miha Filipič for optical simulations of random pyramids and to Dr. Marko Topič for allowing access to CROWM simulator. I would also like to thank Ken Mossman and Diana Convey for training me on AFM, SEM, FIB, optical profilometer and ellipsometer tools. I would also like to express my deep appreciation for all the help given to me by Ron Synowicki from JA Woollam to collect reliable and accurate ellipsometric spectra of samples and his help with subsequent fitting to obtain the optical constants. I am also indebted to McGehee research group at CU Boulder (previously at Stanford), especially Prof. Mike McGehee, Dr. Kevin Bush, Dr. Rohit Prasanna, Dr. Alex Palmstrom and Prof. Stacey Bent for helpful discussions and for supplying numerous samples for ellipsometric analysis and perovskite solar cells, without which this dissertation would not have been possible. Special thanks to Prof. Jinsong, Dr. Bo Chen and Dr. Zhibin Yang from Huang research group at Univ. of North Carolina (UNC) for providing narrow-bandgap films and cells. Many thanks to Carey Reich from CSU for providing wide-bandgap CdTe films.

Now I would like to extend my sincere thanks to people I had the pleasure to work with and learn from in the Holman research group, Dr. Mathieu Boccard for helpful discussions,

Dr. Jianwei Shi for his friendship and for providing a-Si:H films and humorous group meeting slides, Dr. Zhengshan Yu for creating new opportunities and bringing forth interesting ideas, Dr. Arthur Onno for insightful discussions and for reviewing my research papers, Dr. Ashling for giving me the first ellipsometry problem, Joe Carpenter for doing SEM and FIB on my samples and board game nights, Peter Firth for inspiring me to work hard and for funny discussions, Jonathan for friendship and allowing me to collaborate on thermal management, Will for keeping the baseline running, Dr. Shannon for bringing desserts to the group meetings, Dr. Shalinee for development of soft deposition tool for perovskites and last but not the least many visiting scholars from whom I had the opportunity to learn from and mentor.

TABLE OF CONTENTS

Page

CHAPTER Page

LIST OF FIGURES

Figure Page

CHAPTER

1 INTRODUCTION

Currently, the photovoltaic (PV) industry is dominated by silicon solar cells, taking approximately 90% of the market share [1]. Among them silicon solar cells based on mono crystalline silicon (c-Si) are gaining popularity due to their potential to produce high efficiency (>25%) solar cells [2]. Even then silicon solar cells are subject to maximum theoretical efficiency of 29.4% due to absorption losses, thermalization losses, thermodynamic losses and intrinsic recombination losses [3]. Silicon solar cells close to 27% efficiency have already been achieved by Kaneka [4, 5]. Such high efficiency is a result of years of research into improving device design and better light management schemes. Therefore, any major achievements in terms of efficiency improvement in future are unlikely.

Besides silicon, other technologies and materials that hold the PV market share are polycrystalline cadmium telluride (CdTe) and copper indium-gallium diselenide (CIGS). These technologies are thin-film based which allows simplified manufacturing process potentially lowering the cost of production. In addition, CdTe is a direct bandgap material which means thinner absorber could be used and thus less material usage. Despite these advantages, CdTe and CIGS too are subject to the single junction Shockley-Queisser limit and practically their efficiencies are saturating close to 23% [6].

1.1 Why Tandem Solar Cells?

For the mainstream PV technology, i.e c-Si, the cost of module is only a fraction of the total cost of installed system [7]. Balance of system costs scale with the installed area and not the output power [8]. Therefore, the only way to decrease the dollar per watt metric

and to make PV more competitive with conventional methods of producing electricity is by achieving higher efficiencies beyond the single junction Shockley-Queisser limit [9]. Similar trend in cost is observed in other solar technologies as well.

One way to increase the efficiency of single junction solar cell is to make multi-junction solar cells by combining more than one bandgap [10]. This allows to reduce the thermalization loss which occurs due to relaxation of high energy electrons to the conduction band edge. Addition of more than one bandgap allows extraction of electrons at a higher voltage thus raising the open-circuit voltage (*Voc*) and efficiency of tandem solar cell. This is depicted in Figure 1-1.

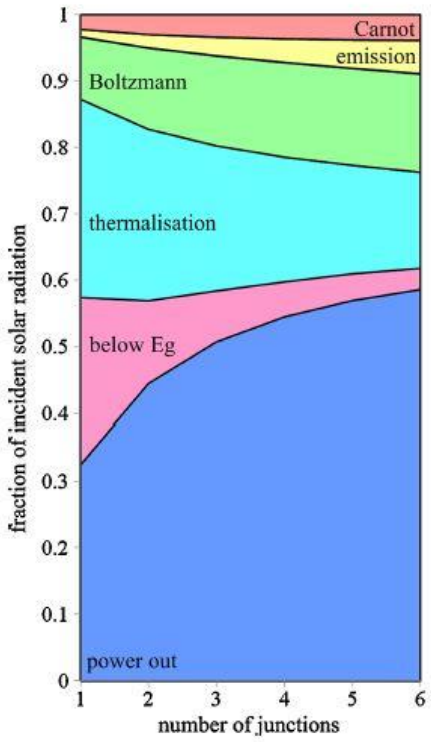

Figure 1-1. Fundamental efficiency limit and losses for multi-junction solar cell with varying number of junctions [10].

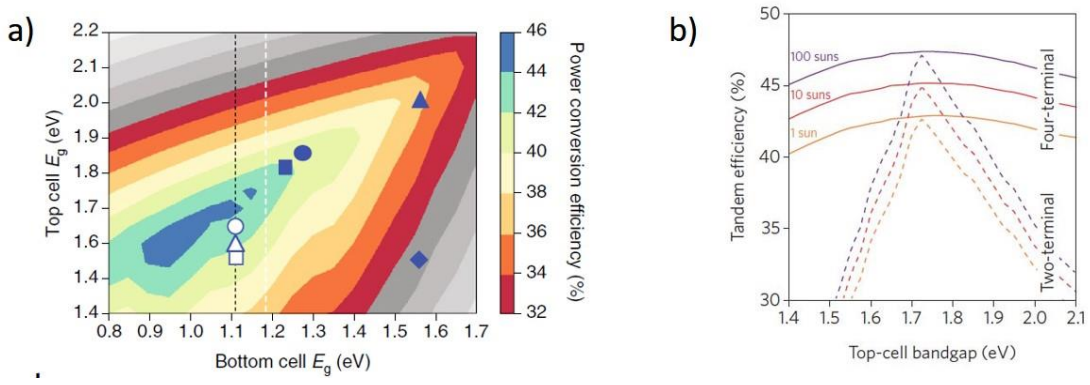

Figure 1-2. Limiting efficiency for a tandem solar cell with free choice of bandgaps (a) [11] and with silicon bottom cell as a function of top cell bandgap (b) [12].

Additional bandgap also helps in reducing the loss of sub-bandgap light that is transmitted and not absorbed.

The easiest case would be to make a multi-junction solar cell with two junctions (referred to as tandem solar cell in this thesis) having a narrow-bandgap bottom cell and wide-bandgap top cell. Figure 1-2 shows with two junctions a conversion efficiency of more than 40% could be achieved [11]. For free choice of bandgaps a top-cell with a bandgap between 1.6 eV to 1.7 eV and bottom-cell with a bandgap between 0.9 eV to 1.1 eV gives the highest conversion efficiency [11, 13]. However, the practicality dictates that silicon be chosen as narrow-bandgap bottom cell due to its dominance of PV market, high *Voc*, high efficiency and close to ideal bandgap 1.12 eV.

With the help of detailed-balance modeling that included Auger recombination Yu *et al.* has shown that with silicon as a bottom cell the optimum bandgap for top cell is 1.7 eV in the case of two-terminal (2T) monolithic tandem. This would result in efficiency of 43%. Similarly, in the case of four-terminal (4T) tandem the highest efficiency is still obtained

for 1.7 eV top cell though the drop in efficiency is not as severe in case the bandgap is not exactly 1.7 eV. This is shown in Figure 1-2(b).

There are several materials that have wider bandgaps than silicon that could be used as top-cell for silicon-based tandem. These include several III-V (GaAs, GaInP, GaNPAs, GaAsP) materials and II-VI (CdTe, $Cd_xMg_{1-x}Te$, $Cd_xZn_{1-x}Te$) materials [14-17]. However, to directly grow these materials on silicon is a challenge due to difference in their lattice constant which results in dislocations lowering the efficiency. In addition, these materials are grown with a process which is expensive thus rendering them not suitable for terrestrial applications. In recent years emergence of perovskite has opened the door to realize a high efficiency, low cost silicon-based tandem. Perovskite belongs to a class of thin-film solar cells, thus have low cost of manufacturing and has recently demonstrated a single junction efficiency of 25.2% [18]. The bandgap of perovskite could easily be tuned in the range of ~1.2-2.3 eV which makes them especially attractive as top cell for silicon based tandem. Wide-bandgap perovskites have been demonstrated with the generic composition of $Cs_yFA_{1-y}Pb(I_xBr_{1-x})_3$ and their bandgap could be tuned by changing the Cs and Br content in the film. In just a couple of years a 2T perovskite/silicon tandem efficiency has jumped from 23.6% to 28% [19, 20]. Similar progress has been made on 4T perovskite/silicon tandem with highest efficiency at 26.4% [21].

Since it is easy to tune the bandgap of perovskites, it is also possible to make all perovskite/perovskite tandem by combining a wide-bandgap and narrow-bandgap perovskite [22-24]. This has the possibility to lower the manufacturing cost further since the complete tandem is thin-film based. By changing the Cs and Sn content in $Cs_yFA_{1-y}Sn_xPb_{1-x}I_3$ the bandgap of low-bandgap perovskite could be tuned. While silicon has a

fixed bandgap which is slightly non-optimal, with low-bandgap perovskite it's bandgap could be tuned to the optimal value of bottom-cell bandgap. So far, a 22.9% efficient 4T and 24.8% 2T perovskite/perovskite has been demonstrated [22, 25, 26].

Bandgap of top-cell material for silicon based tandems is an important criteria. However, there are several other requirements, such as, high absorption coefficient, abrupt band edge, favorable refractive index, excellent IR transparency etc. Similar requirements are applicable to narrow-bandgap bottom-cell material. However, this knowledge is still missing for most of these new absorber materials which is crucial to perform limiting efficiency calculations as well as to draw conclusions about device performance, such as, limiting V_{oc}. In addition, this information could be used in rigorous optical modeling to simulate and develop novel device architectures to serve as guideline for development of tandem solar cells.

1.2 Introduction to Light Management

Information presented in this section is largely taken from [27]. Light management is the science of managing the incident solar radiation with the goal to maximize the photo-generated current in the solar cell through the choice of materials with right optical properties and intelligent device design. In particular, light management deals with three important aspects, antireflection of incident light, minimizing parasitic absorptance in various layers of the cell and light-trapping within the absorber to maximize the short-circuit current density (*Jsc*). These three phenomena are shown in Figure 1-3. To calculate J_{sc} one can follow an incident ray through the absorber. In Figure 1-3 the solar cell is assumed to have no transmittance out of the rear as most solar cells have complete metal on the rear surface. The front-surface reflectance of the incident light is represented

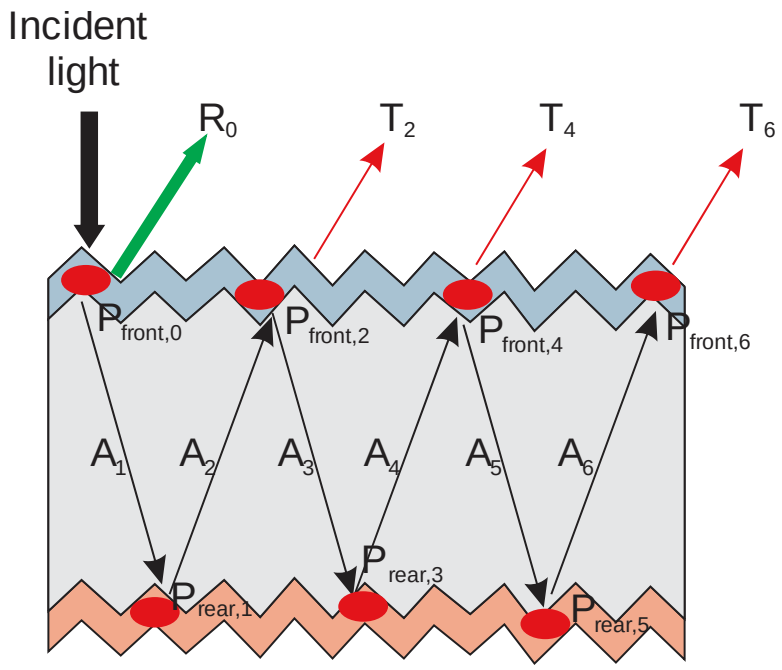

Figure 1-3. Schematic showing the light path in a solar cell.

as R_0 and parasitic absorptance in the front and rear surfaces are labelled as P_{front} and P_{rear} respectively. And absorptance in solar cell for each pass is given by A_x where *x* is the pass number. Then external quantum efficiency (*EQE*) is equal to the total absorptance in the absorber, given by Equation 1.1

$$EQE = A_1 + A_2 + A_3 \ldots \quad 1.1$$

Here absorptance per pass can be written in terms of single-pass absorptance according to Equation 1.2.

$$A_2 = (1 - r)\left(1 - p_{front,0}\right)(1 - a)\left(1 - p_{rear,1}\right)a \quad 1.2$$

Here *a* is the single-pass absorptance in the absorber and is given by Equation 1.3

$$a = 1 - e^{-\alpha d\left(\frac{1}{cos\theta}\right)} \quad 1.3$$

In Equation 1.3 the factor 1/cosθ represents the angle at which the light ray traverses the wafer and is measured from normal of the absorber. This factor represents the path-length

enhancement experienced by the light rays scattering due to texture at the time of entrance. Single-pass absorbance is also dependent on the thickness of the absorber (d) and absorption coefficient (α). Following Equation 1.3, total absorptance and hence *EQE* is given by Equation 1.4

$$EQE = (1 - r)\left(1 - p_{front}\right) \tag{1.4}$$

$$\sum_{k=1}^{\infty}\Big\{(1 - p_{rear})^{k-1}\left(1 - p_{front}\right)^{k-1}\left(1 - t_{front}\right)^{k-1}(1 - a)^{2k-2} + (1 - p_{rear})^{k}\left(1 - p_{front}\right)^{k-1}\left(1 - t_{front}\right)^{k-1}(1 - a)^{2k-1}\Big\}$$

Each pass number is given by *k*. The equation above assumes all absorbed photons are collected. Then to calculate J_{sc} the product of *EQE* and AM1.5G solar spectrum is integrated.

However it is not possible to measure single-pass absorptance in the absorber or parasitic absorptance at the front and rear. But it is possible to relate the absorptance in the absorber with commonly measured quantities such as reflectance and EQE of the solar cell. Using the notation given in earlier equations total reflectance measured with spectrophotometer of the cells would be,

$$R = R_0 + T_2 + T_4 + T_6 \tag{1.5}$$

Here R is total reflectance, R_0 is the front-surface reflectance and T_2+T_4+T_6 equal escape reflectance (R_{esc}). EQE of the cell on the other hand is same as its J_{sc} and hence given by Equation 1.4. Then by plotting 1-R and EQE together against wavelengths one can evaluate total parasitic absorptance at each wavelength as given by Equation 1.6,

$$A_{parasitic} = 1 - (R_0 + R_{esc}) - EQE \tag{1.6}$$

EQE in the absence of parasitic absorptance is the measure of light-trapping afforded by the texture of the absorber. Therefore, to evaluate EQE the parasitic absorptance has to be divide equitably between R_{esc} and EQE. For that following the approach presented in [27], the ratio of EQE to R_{esc} plus EQE before and after correction should be the same. Mathematically this is given by Equation 1.7,

$$\frac{EQE}{R_{esc} + EQE} = \frac{EQE_c}{R_{esc,c} + EQE_c} \tag{1.7}$$

Here EQE_c and $R_{esc,c}$ are the corrected versions of EQE and R_{esc} without parasitic absorptance. With this correction EQE could be evaluated and compared to absorptance in the absorber if the light-trapping was equal to Lambertians scatterer.

1.3 Light Management in Silicon and Perovskite Based Tandems

In simple devices such as single junction solar cells, aspects of light management could be studied using analytical approaches. However for more complex devices such as silicon and perovskite based tandems that comprise of many layers of thin films as well as scattering surfaces comprehensive optical modeling and simulation is required to investigate the components of light management. For this detailed knowledge of device structure and optical properties of each layer has to be known.

Silicon suffers from low absorption coefficient around its band edge. Combined with the fact, silicon wafers used to make solar cells maintain finite thickness (150-200 μm) to reduce the material cost which results in incomplete absorption of light close to its bandgap. Light not absorbed in one round trip across the wafer either escapes or contributes to parasitic absorptance both in single junction silicon and silicon tandem solar cells. Moreover, non-absorbed light can't either be absorbed in top-cell in case of tandem.

Therefore, efficient light trapping of long wavelength light is very important both for single junction silicon and silicon bottom-cell. Analytical modeling of silicon based tandems often assume bottom silicon cell to have Lambertian light trapping [12]. However, mono c-Si solar cells used in highest efficiency single junction silicon and silicon based tandems are textured in alkaline solution which produces random upright pyramids on its surface to improve light trapping [19, 28, 29]. Light transmitted into the wafer travels at oblique angles due to interaction with pyramidal texture, often referred to as path-length enhancement. But more importantly random pyramidal texture traps the transmitted light inside the absorber that returns after reflecting from the back surface. Therefore, trapped light travels several times inside the absorber. Yablonovitch *et al*. has shown for an absorber with refractive index *n*, with perfectly randomizing surface (also known as lambertian surface/scaterrer) and zero parasitic absorptance, the maximum absorption enhancement of weakly absorbed light due to light trapping is equal to $4n^2$ [30]. There are numerous studies that have investigated the light trapping potential of random pyramids and compared them to Yablonovitch limit with varying results. For example, recently it has been shown by Barugkin *et al*. that random pyramids don't reach Yablonovitch limit, similar results have been shown by Shuster et al. [31, 32]. However, these studies didn't preclude the effects of parasitic absorptance. Whereas, Brendel *et al*. has found that pyramids with varying shapes do reach $4n^2$ limit under isotropic illumination and Campbell *et al*. has also shown that perpendicular slates can exceed $4n^2$ limit for various angles of incidence [33, 34]. But these studies have failed to capture the randomness in the slope of pyramids and often model ideal pyramids that have 54.7° slope. Therefore, there is a need

to clearly ascertain the true absorption enhancement that could be gained with real random pyramids in the absence of parasitic absorptance.

Second important aspect of light management is efficient light incoupling into the solar cells. This is achieved by reducing front surface reflectance which is not easy to accomplish. For example, when silicon is combined with perovskite, II-VI and III-V materials to form top-cell/silicon tandem the top surface of silicon has to be planarized before the top-cell material could be grown or deposited. In perovskite's case it is necessary to have a planar surface because it is deposited using spin-coating process. In II-VI materials such as CdTe surface has to be planar to ensure high material quality and to avoid shunts and void in the film. Similarly, in III-V materials case they are grown using molecular bean epitaxy (MBE) which requires atomically flat surface. Therefore, silicon based tandems usually have planar front surface which leads to high front surface reflectance. Same is true for perovskite/perovskite tandem which is an all thin-film device and deposited using spin-coating. Therefore, a lack of texture at the front surface of tandem leads to reflectance loss. Another reason for high reflectance loss is that at the front of these tandems there are several thin-films whose thicknesses if not properly tuned could lead to high reflectance due to interference in these films. This problem also extends to single junction version of these individual sub-cells and also to modules.

Planar antireflection coating (ARC) is one way to reduce reflectance, however, it has been shown that textured surface does a better job [35, 36]. 2T perovskite/Si tandem cells reported in the literature had approximately 7.7 mA/cm^2 and 8.7 mA/cm^2 reflectance loss (between 350 nm and 1100 nm), despite having single-layer indium tin oxide (ITO) or indium oxide (IO:H) ARCs [37, 38]. Previously a similar tandem has been reported with a

double layer LiF/ITO ARC, yet the remaining 4.8 mA/cm^2 reflectance loss remained the largest optical loss in the 23.6%-efficient device [19]. Similarly, a recent 30.2%-efficient GaInP/$Al_xGa_{1-x}As$/Si triple-junction solar cell with a Ta_2O_5/MgF_2 double layer ARC lost a significant 3.9 mA/cm^2 to reflection [39]. Other approach to reduce reflectance is by using textured ARC at the front which can be produced using hot-embossing or UV nano-imprint ligthography (UV-NIL) [40-42]. With this technique an arbitrary texture could be transferred into an arbitrary transparent material which could then be used as an ARC. With this method, the random pyramid texture of monocrystalline silicon wafers was transferred to thin-film silicon and perovskite solar cells, increasing the *Jsc* by 0.5 mA/cm^2 and 1.0 mA/cm^2, respectively [43, 44]. Textured scattering surface is a promising way to reduce reflectance and perhaps also to improve light trapping, but the limit of this approach has to be explored.

Another major aspect of light management is to understand and minimize parasitic absorptance in various layers of the solar cells. This information can easily be obtained if reflectance and external-quantum-efficiency (EQE) of the device is known, then the difference between 1-reflectance and EQE amounts to parasitic absorptance. However, what can't be inferred is the role of individual layers towards the total parasitic absorptance. This problem is especially difficult to tackle in tandem solar cells which generally consist of many thin-film layers whose thicknesses not only effect total parasitic losses but also impact the total reflectance.

For example, modeling results have shown that 2T perovskite/silicon tandem should be able to achieve efficiency greater than 30% but practically it has not been achieved. Initial 2T perovskite/silicon tandems suffered a lot from parasitic absorptance because they

used Spiro-OMeTAD (lost nearly 7.4 mA/cm^2) as hole contact placed at the front [45]. This is also called the regular architecture. Bush et al. later improved this device design by moving electron contact to the front which can be processed much thinner thus reducing the parasitic losses [19]. This device design is called inverted architecture. Yet parasitic losses close to 5.5 mA/cm^2 remain. The source of parasitic losses that still remain are layers such as C_{60} electron contact, front transparent conductive oxide (TCO) layer employed for lateral conductivity, SnO_2 ALD buffer layer, NiO_x hole contact, intermediate recombination layer etc. Another source of loss in efficiency in the implementation of 2T perovskite/silicon tandem is the lack of current-matching between top and bottom sub-cell. This problem is handled by adjusting the thickness of top-cell for a given top-cell bandgap. This problem further gets complicated when the 2T device design is changed to improve the overall light management. For example, by addition of textured ARC on the front or by employing double textured silicon bottom cell [28, 38]. Therefore, there is a need to accurately characterize the optical constants of wide-bandgap perovskites alongside typical electron (C_{60}, VO_x) and hole (NiO_x, PTAA) contacts as well as TCOs. These then could be used in optical simulator to study optical losses in actual devices as well as to improve them by changing the light management schemes.

Perovskite/perovskite tandems which have a greater freedom to tune the bandgap of each sub-cell have the potential to reach >30% efficiency. They generally employ similar sub layers as perovskite/silicon tandem, except that the bottom sub-cell is low-bandgap perovskite. Thus, all-perovskite tandem is completely a thin-film device which means thickness of each layer greatly contributes to parasitic absorptance and reflectance loss. The highest efficiency 2T all-perovskite tandem has reached 24.8% [25]. However, low-

bandgap perovskite employed in all-perovskite tandem solar cells have low absorption coefficient near it's band edge resulting in low EQE both in single junction and tandems [11, 23]. This opens the room for improving light management in these solar cells by improving the device design and applying texturing for path length enhancement and light trapping to enhance the EQE around bandgap region. But this requires detailed optical modeling for which optical constants of these new low bandgap perovskites would be required.

Similarly for 4T tandems there is no requirement for current-matching but there is a need to optimize between parasitic and electrical losses. 4T tandems comprise of more layers than 2T tandems such as more TCO layers for lateral conduction of current. These TCO layers could be made more transparent at the expense of having higher sheet resistance or vice-versa [46, 47].

1.3 Outline of Thesis

The dominant PV technology, that is, single junction silicon is reaching its practical efficiency limit which has paved way for two-junction tandem solar cells that have the promise to reach >30% efficiency. Specifically, of immense importance are silicon based tandems where a top-cell is combined with a silicon bottom-cell. Another class of tandems that has gained importance is perovskite/perovskite tandems due to a possibility of high efficiency and low manufacturing cost. However, for these tandem solar cells to be successful, there are several material and light management challenges that need to be addressed.

Chapter 1 gives a general introduction to the field of silicon and perovskite solar cells and their tandems and provides an outline of thesis.

Chapter 2 deals with the light trapping aspect of light management in silicon solar cells textured with random pyramids. This is important to know since random pyramids are being integrated into tandems as well. Specifically, in this chapter is presented a comparison of light trapping between real-random pyramids, ideal-random pyramids (all pyramids having an ideal 54.7° base angle) and Lambertian scaterrer. This is done by reporting the angular distribution function of light rays trapped inside the wafer for each pass.

Chapter 3 deals with the problem and solution of front surface reflectance. This is an important and dominant optical loss in many planar solar cells such as, single-junction perovskite, perovskite/silicon and perovskite/perovskite tandems etc. Therefore, in this chapter PDMS foil textured with random pyramids is presented as a solution. And using PDMS foil and silicon solar cells with no, single and double-sided texture as a platform, the efficacy of this method is explored.

Chapters 4, 5 and 6 in this thesis deal with characterizing the optical properties of new top- and bottom-cell materials developed for tandem application. So a methodology is developed using spectroscopic ellipsometry to characterize new absorbers. These chapters also deal with the integration of these new materials to form silicon and perovskite based tandems which creates several light management challenges. Some of these challenges arise due to the incompatibility of fabrication process or material properties of top and bottom sub-cells which restricts the tandem device design resulting in optical losses. Moreover, these tandems are multilayered, which makes it non-trivial to design the optically best tandem device. Therefore, comprehensive optical modeling is performed of complete silicon and perovskite based tandem solar cells to understand the parasitic,

reflectance and light trapping losses in current state of the art tandems in addition to exploring more favorable light management strategies thus guiding the device design. Specifically, Chapter 4 deals with wide-bandgap perovskite absorbers and perovskite/silicon tandems, chapter 5 deals with low-bandgap perovskite and perovskite/perovskite tandems and lastly chapter 6 presents spectroscopic ellipsometry studies of wide-bandgap alloys of CdTe to be used as top-cells in II-VI/silicon tandems. Finally, Chapter 7 presents the conclusion and future work.

CHAPTER

2 VISUALIZING LIGHT TRAPPING WITHIN TEXTURED SILICON SOLAR CELLS

2.1 Introduction

Commercial silicon solar cells have textures on their front and rear surfaces to minimize front-surface reflection and maximize the path length of weakly absorbed light. The former is routinely measured and used to tune the texturing process, but the latter is difficult to quantify experimentally because the relevant measurable quantity—the total absorbance—conflates light trapping with parasitic absorption. (Throughout this thesis, "light trapping" refers exclusively to the path length in the absence of absorption and, thus, depends only on texture and refractive index; "parasitic absorption" refers to absorption in layers other than the wafer.) To disentangle these processes and understand how a given texture traps light, it is common to simulate, at sub-bandgap wavelengths, representative silicon solar cell structures with perfect front transmission and rear reflection, as is shown in Figure 2-1.

Monocrystalline silicon solar cells are fabricated on (100) wafers that are textured in alkaline solutions, leading to anisotropic etching of the front and rear surfaces. The resulting pyramids have random positions and heights but not, ideally, random base angle (α_B). The expected base angle is 54.7° and is defined by the angle between the (111) and (100) planes. Randomly distributed pyramids with this ideal base angle are referred to as "ideal-random" in this paper. Previous optical simulations have studied light trapping in wafers with ideal-random pyramids using ray tracing and compared the path-length enhancement to that achieved with other textures [34, 48-54]. The benchmark in these comparisons is usually Lambertian (i.e. isotropic scattering) surfaces, which provide an

average path-length enhancement (i.e. averaged over all possible pathways) of $4n^2$ for weakly absorbed light, with n the refractive index of the absorbing material [30]. Lambertian surfaces are only one particular scheme reaching this $4n^2$ *average* path-length enhancement, often called the Yablonovitch limit or the Lambertian limit. Luque and Miñano, and later Rau *et al.*, have shown that the $4n^2$ Lambertian limit is the actual *average* path-length enhancement limit only when considering—and, hence, averaging over—all angles of incidence [55-57]. Therefore, the path-length enhancement can be greater than $4n^2$ for a subset of angles of incidence, but at the expense of a reduced path-length enhancement at other angles, such that the $4n^2$ limit is not violated [56, 58]. This behavior can be implemented with geometric concentration or angle selectivity schemes. Thus, the actual limit of the *average* path-length enhancement is [55, 57, 58]:

$$L = \frac{4n^2 w}{\sin^2(\theta_{in})} \tag{1}$$

Here θ_{in} is the acceptance angle of the angular selectivity filter or related to the concentration factor.

This Lambertian limit is greater than has so far been measured or simulated for any non-random texture over a wide range of incident angles and photon wavelengths. Of particular importance, Brendel demonstrated that the *average* simulated path-length enhancement of ideal-random pyramids under isotropic illumination can also approach $4n^2$, but this does not ensure that ideal-random pyramids and Lambertian surfaces will yield the same short-circuit current densities since the *distribution* of path lengths can be (and is) different [54]. In an earlier contribution, Campbell and Green had found that the fraction of rays that remain trapped in a wafer with ideal-random pyramids (but of identical size) approaches

that of a wafer with Lambertian surfaces after approximately four passes through the wafer [34]. However, it is not just the *number* of trapped rays that determines the path-length enhancement, but also the angles with which they traverse the wafer. This missing information can be conveyed by plotting the angular distribution function (ADF) of a packet of rays inside the wafer and tracking how it evolves over time as those rays scatter at the front and rear surfaces.

Another piece of information that is missing from the silicon light-trapping literature is how the non-idealities of real pyramids affect the expected path-length enhancement. Baker-Finch and McIntosh calculated approximate base-angle distributions by fitting measured angle-resolved reflectance curves with Gaussian functions; in doing so, they revealed that real pyramids are not only distributed randomly in space, but also have a distribution of base angles that peaks below 54.7° [59]. In particular, they found that samples etched in potassium hydroxide (KOH) have a base angle distribution centered at 50.5° with a full width at half maximum (FWHM) of 4.8°, whereas those etched in tetramethylammonium hydroxide (TMAH) have a distribution centered at 52.1° with a FWHM of 2.5°. Similarly, Mackel *et al.*, showed that pyramids have variable effective base angle between 47.9° to 54.3° and that the reflectance from silicon surface decreases linearly with its value but its influence on path-length enhancement was not studied [60]. Randomly distributed pyramids with a (measured) distribution of base angles are referred to as “real-random” in this paper.

In this contribution, we investigate light trapping in wafers textured with real-random pyramids and compare the results to those obtained with ideal-random pyramids and Lambertian surfaces. To this end, we accurately measure the topography of the surface of

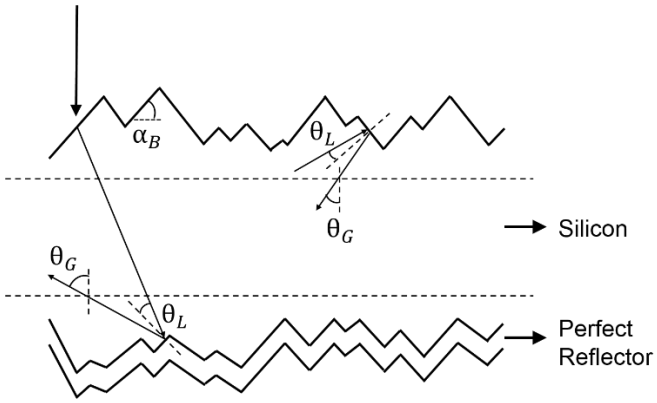

Figure 2-1. Illustration of the base angle (α_B) of pyramids, the global angle (θ_G) and the local angle (θ_L). The pyramids base angle is defined as the angle between the pyramid facets and its base. Horizontal dashed lines are imaginary planes parallel to the macro-scale wafer surface. The global angle is defined relatively to these planes. Conversely, the local angle is defined at the microscopic scale, as the angle at which rays hit the pyramid facets.

alkaline-textured silicon wafers with atomic force microscopy (AFM). The resulting real-random pyramid maps—along with ideal-random pyramid maps that are mathematically "reconstructed" from the measured topographies using 54.7° base angles—are ray-traced to probe their light-trapping capability. Throughout the simulations, we record the ADF of the rays each time they hit the front or rear internal surface of the wafer; the ADFs conveniently contain all information about light trapping. There are, in fact, two ways to report ADFs, and each method is valuable. The "global ADF" gives the rays' trajectories with respect to the wafer normal—the global angle (θ_G), as shown in Figure 2-1. As it is, the angles at which rays travel from the front to rear surface, and vice-versa, the global ADF can be used to calculate the average path-length enhancement and total absorption in the wafer, provided the number of rays remaining is known at each pass. The "local ADF" gives the rays' trajectories with respect to the normal of the pyramid facets—the local angle (θ_L), also shown in Figure 2-1—and strongly depends on the pyramid base angle

distribution. The local ADF at the front surface determines the transmission of light out of the wafer (hereafter termed “escape reflection” because it contributes to the reflected light in a measurement). Similarly, the local ADF at the rear surface determines the absorption in the rear contact of a solar cell; the structures simulated here have perfect rear reflectors, but real cells suffer from parasitic absorption that depends on local angle [61-63]. Both escape reflection and parasitic absorption reduce the number of rays remaining in the wafer and, thus, the average path-length enhancement.

2.2 Experimental

2.2.1 Measurements

Monocrystalline silicon wafers with (100) orientation and either random or inverted pyramid textures—both formed by alkaline etching—were provided by commercial silicon solar cell manufacturers. From these wafers, realistic topographical maps of real-random pyramids and real-inverted pyramids were generated. Optical profilometry and scanning electron microscope (SEM) stereoscopic image reconstruction were considered as methods to measure the topography, but both were found to lack the necessary nanometer-scale spatial resolution required to resolve the sharp peaks and valleys of pyramids. AFM was chosen instead, and measurements were performed in tapping mode to avoid tip breakage when scanning over large areas with dramatic changes in height. To accommodate the tallest pyramids of the samples, which were over 7 μm in height, an NT-MTD AFM with a z-range of 12 μm was employed.

Particular attention was given to choosing the best-suited AFM tip, which was found to be a >10-μm-tall, sharp, single-crystal diamond tip from SCD Probes. This tip correctly reproduced the pyramid base angles and avoided flat spots in the scans, that can arise when

the cantilever hits the top of pyramids thus stopping the tip from reaching the valleys. Prior to measurement, z (height) and x-z (side-wall angle) calibrations were performed using 0.11-, 0.52-, and 1.4-μm-tall standards and a 70° edge-angle standard, all from K-TEK Nanotechnology. For all measurements, the scanned area was sufficiently large (40 μm × 40 μm) to be representative of the overall surface. In particular, each scan included approximately 100 peaks for random pyramids and 25 peaks for inverted pyramids—enough to accurately capture the distribution of base angle, the variation of pyramid height, and the randomness of the pyramid positions.

The measured real-random and real-inverted pyramid AFM maps served as input into a custom MATLAB code to create ideal-random pyramid and ideal-inverted pyramid maps by changing the base angle of all pyramids to 54.7° while keeping their peak positions and heights the same. The algorithm first finds the pyramid peaks in the input map and then constructs a new map by reducing (or increasing, for inverted pyramids) the height of the neighboring pixels according to the desired base angle. This process is repeated until neighboring pyramids intersect. The result of this strategy is that the points where adjacent pyramids intersect have slightly different base angle than the desired value. Therefore, a map with only one base angle for all pyramids shows a very narrow distribution around the desired base angle.

For select samples, AFM measurements were complemented with scanning electron microscopy (SEM) images of cross sections cut with a focused ion beam (FIB). Sequential imaging and milling were done with an FEI Nova 200 by pointing the FIB and SEM columns at the same point (the eucentric point) on the wafer. Milling was performed with a gallium-ion beam oriented perpendicular to the wafer and rastered parallel to (two of the

four) pyramid base edges. SEM images were taken at 52° from the wafer normal. Before milling, the pyramids were coated with 200 nm of platinum to protect the pyramid profiles and to provide contrast that simplifies subsequent image processing.

The pyramid base angle distribution of select samples was calculated from AFM scans using Gwyddion, a data analysis program, and from SEM images of milled cross-sections using image processing tools in MATLAB. Before calculating base angle distributions, the images were oriented such that the x and y directions were aligned with the pyramid base edges and the z direction was aligned with the wafer normal. In Gwyddion, a plane was fit at each pixel and the magnitude of its gradient—the base angle—was calculated. In MATLAB, a pixel intensity threshold filter was used to find the profile of the pyramids, which appear dark and are capped with platinum that appears bright. A line was then fit at each pixel along the profile through 50 neighboring points, which corresponds to a physical distance of 1.35 μm, and its slope—the base angle—was calculated.

The total front-surface reflectance of textured wafers was measured over the 300–1000 nm wavelength range using a PerkinElmer Lambda 950 spectrophotometer equipped with an integrating sphere. The angle of incidence was 7° from the wafer normal. The angle-resolved reflectance was measured using an Automated Reflectance/Transmittance Analyzer (ARTA) that connects to the spectrophotometer. For these measurements, 270 nm light was incident at angles ranging from 0° to 20° relative to the wafer normal. For each angle of incidence, an integrating sphere detector mounted on a goniometer circled the sample in the horizontal plane, recording the reflectance every 2°. Note that the angle-resolved reflectance cannot be measured for detector angles between −12 and +12° because the reflected light is blocked by the incident light source. The aperture width of the detector

was 5° for all measurements. The wafers were oriented such that (two of the four) base edges of each pyramid, as well as the wafer normal, were coplanar with the circle traced by the detector.

2.2.2 Optical simulations

Optical simulations were performed with an optical simulator named CROWM (combined ray optics/wave optics model) that has been previously used to study the optical properties of solar cells [64-66]. CROWM is capable of performing three-dimensional incoherent ray tracing based on geometric optics, as well as transfer-matrix calculations for thin films included in the simulation domain. Simulations were carried out for air/silicon/perfect-reflector structures with the top and bottom surfaces of the silicon having a pyramid texture measured by AFM (real-random and real-inverted) or reconstructed from such measurements (ideal-random and ideal-inverted). The thickness of the silicon wafer was 180 μm for all simulations. Periodic lateral boundary conditions were enforced by mirroring the textures across first the x-axis and then the y-axis. The front-surface reflection spectrum of each texture was simulated for the 300–1000 nm wavelength range, with a 10 nm step, for light incident at 7° with respect to the wafer normal (as in the spectrophotometry measurements). Also simulated was the angle-resolved reflectance for 270 nm light having an angle of incidence between 0° and 20°. As in the measurements, a simulated detector was swept across angles between -90° and 90° with respect to the incident beam, in the plane perpendicular to the wafer surface and the pyramid base edges. The aperture width of the simulated detector was 5°.

Next, local and global ADFs were collected for each pass through the wafer by monitoring each ray of the normally incident 1200 nm light. This wavelength was chosen

because the absorption in silicon is negligible. For these simulations, we implemented perfect transmission of incident rays and rays hitting the front surface within the escape cone from inside the silicon; this is equivalent to having a perfect antireflection coating. Rays were binned in 0.5° increments according to their angle (0–90°) with respect to either the appropriate pyramid facet (local ADF) or the wafer normal (global ADF). The ADFs were then normalized at each pass by dividing by the total power of the remaining rays. Lastly, the total path-length enhancement was investigated as a function of the angle of incidence of 1200 nm light for angles between 0° and 75°, with a 5° step. And the wavelength is kept constant at 1200 nm. The total path length-enhancement was calculated by dividing the total distance traveled by all 10,000 rays by the total number of rays, and expressing the result in terms of the wafer thickness.

2.3 Results and Discussion

2.3.1 AFM map validation

Obtaining an accurate topographical map with AFM is not a trivial task for samples containing both micrometer- and nanometer-scale features. Challenges that we encountered, particularly over large-area scans, include tip-related artifacts, rounded edges of pyramids, and artificial flat spots [67, 68]. Consequently, the fidelity of the AFM height maps was verified prior to light-trapping analysis using measurements and simulations of the total and angle-resolved reflectance, as described in detail below. We begin this verification process with inverted pyramids and then move on to random pyramids. While inverted pyramids are not the primary focus of this paper, they serve as a convenient test case or standard for the verification methodology because they have less randomness in

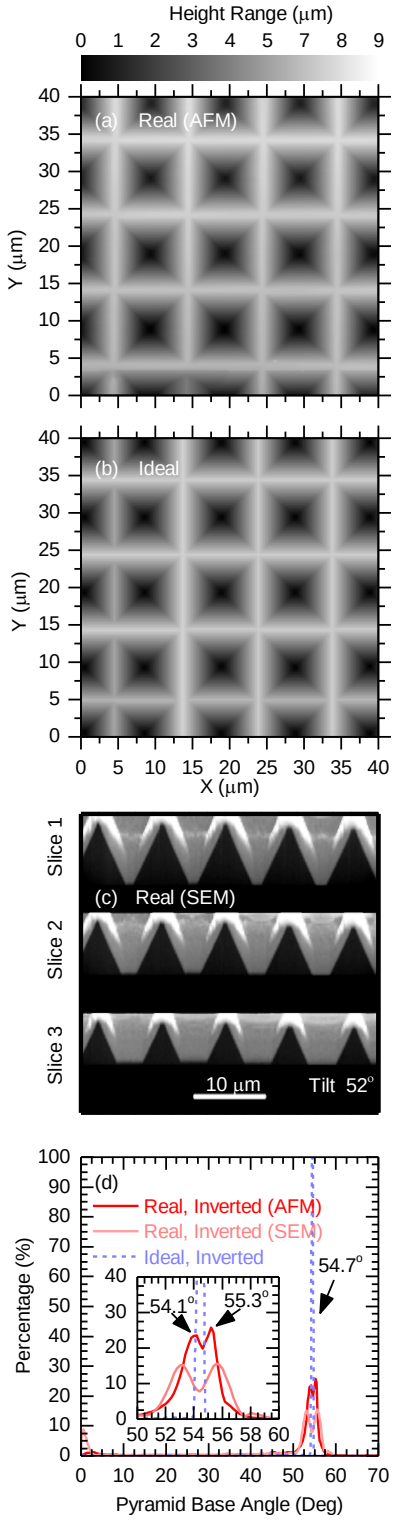

Figure 2-2. (a) AFM map of an actual inverted-pyramids wafer (real-inverted). (b) Reconstructed map from (a) with ideal inverted pyramids (ideal-inverted). (c) SEM cross-sections of successive slices of real-inverted pyramids, milled with FIB. (d) Plot of base-angle distribution for inverted pyramids.

pyramid height, position, and base angle than random pyramids, making them easier to analyze.

Figure 2-2a shows an AFM scan of real-inverted pyramids approximately 9 μm in depth, and Figure 2-2d reveals the pyramid base angle distribution calculated from this map. There are two dominant peaks in the distribution curve—at 54.1° and 55.3°—with an average of 54.7°, the expected base angle for anisotropic etching of silicon. The appearance of two peaks may be the result of a slight (0.6°) sample tilt during measurement, leading to a splitting of the measured angles for the leading and trailing edges of pyramids. Alternatively, the wafer may have been 0.6° off-cut from the intended (100) orientation prior to texturing—this is just at the orientation tolerance specified by most wafer manufacturers—resulting in pyramids that are in fact slightly tilted [51]. The small peak at 0° originates from flat spots between the inverted pyramids—visible in Figure 2-2a—that result from the photolithographic masking process used to define the location of each inverted pyramid.

As a preliminary check of the base-angle distribution extracted from AFM, the inverted pyramid sample was progressively milled parallel to the (010) plane with a FIB, and SEM images were taken of each cross section. Three such cross-sections are displayed in Figure 3-2c. The associated calculated base-angle distribution, displayed in Figure 2-2d, is slightly broader than that from AFM (note the very different data processing used to extract these angles), but contains the same split peak and average value of 54.7°. Also shown in Figure 2-2d is the base angle distribution of the ideal-inverted pyramid map in Figure 2-2b, which was reconstructed from the measured map in Figure 2-2a. As intended, ideal-inverted

pyramids present a unique narrow peak centered around 54.7°.

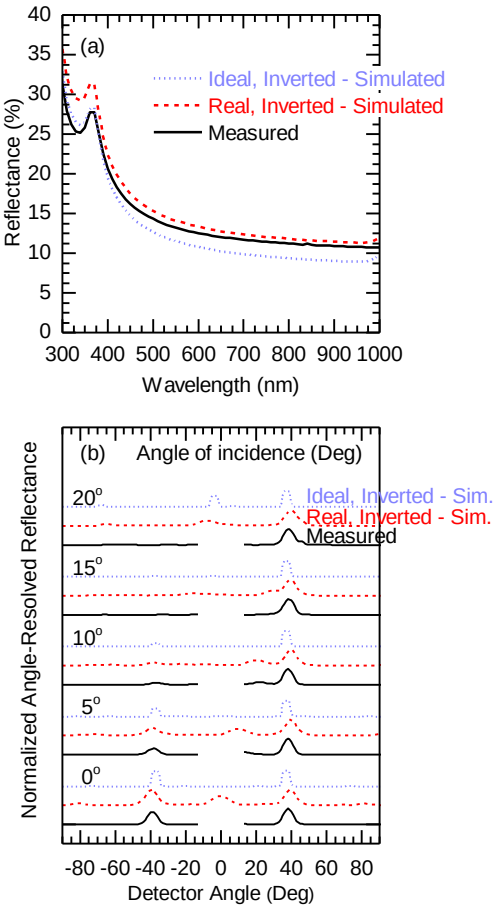

Figure 2-3. Spectrally-resolved total reflectance (a) and angle-resolved reflectance (b) from simulation of ideal-inverted pyramids, simulation of real-inverted pyramids, and experimental spectrophotometry measurement. A noteworthy feature of the curves is the presence of a peak at a detector angle of 0° degrees for simulated real-inverted pyramids and experimental measurement while this peak is absent for ideal-inverted pyramids. For the rest of the incident angles, the peaks of all three curves match.

In Figure 2-3a, the measured total reflectance spectrum of the inverted-pyramid sample is compared with the simulated spectra from real-inverted pyramids—i.e., that obtained by ray tracing from the map in Figure 2-2a—as well as from ideal-inverted pyramids, mapped in Figure 2-2b. Assuming the AFM map to be an accurate reproduction of the actual surface

morphology and the features to be sufficiently large to use geometric optics [69, 70], we expect ray-tracing simulations to precisely reproduce the optical response of the sample. Here, the simulated real-inverted pyramids reflectance is in strong agreement with the measured data above 400 nm, leading to an AM1.5G-weighted average reflectance difference limited to 0.2% (higher). This compares with a difference of 1.3% (lower) for the simulated ideal-inverted pyramids, in large part due to the elimination of flat spots during the construction of the ideal-inverted pyramid map.

The measured AFM map can be further validated using angle-resolved reflectance measurements. The detector angle at which the peak reflectance is measured for normally incident light ($\theta_{r,peak}$) varies with the prevalent pyramid base angle ($\alpha_{B,peak}$) according to:

$$\theta_{r,peak} = 4\alpha_{B,peak} - 180^{\circ} \quad (2)$$

with $\theta_{r,peak}$ and $\alpha_{B,peak}$ in degrees.[71] The angle-resolved reflectance is, thus, a sensitive probe of base angle: for each 1°-variation in base angle, the angle at which the most light is reflected shifts by 4°.

Figure 2-3b compares the measured angle-resolved reflectance to that obtained by ray tracing from the real- and ideal-inverted pyramid maps, for several angles of incidence. In the simulated ideal-inverted pyramid case at 0° incidence, the peak scattering angle lies at ±39.5°, corresponding to a base angle of 54.9°—in close agreement with the correct ideal base angle of 54.7°. We assume a 5° detector aperture in our simulations in order to match the experimental setup, hence the breadth of the sharp-walled peaks for ideal-inverted pyramids. As expected, the measured data presents peaks at a nearly identical scattering angle of ±39°, as real pyramids exhibit the same average base angle as the simulated ideal-inverted pyramids. However, the peaks are broader, due to the non-ideal distribution in

base angles shown in Figure 2-2d. The simulated peak scattering angle from real-inverted

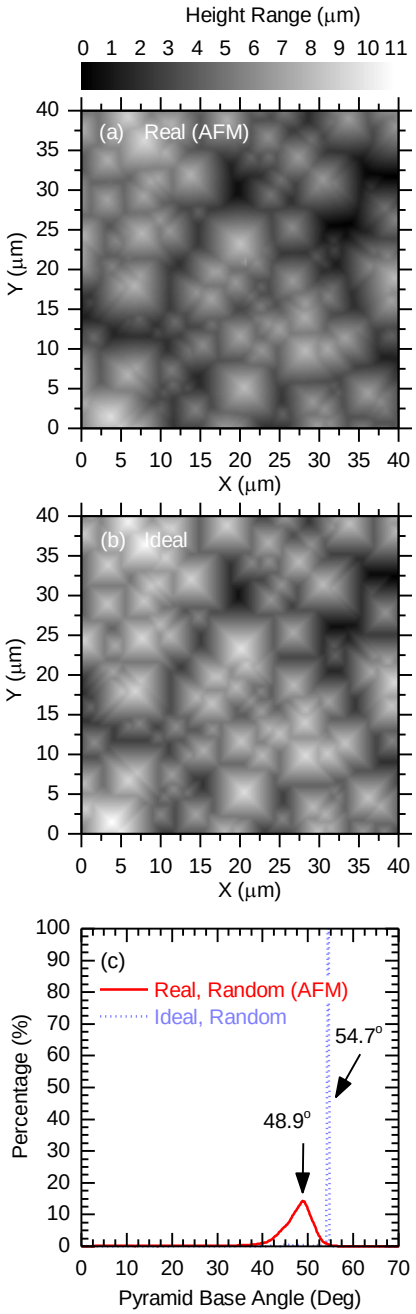

Figure 2-4. (a) AFM map of real-random pyramid wafer. (b) Ideal-random pyramids map reconstructed from (a). (c) Base angle distribution of real-random and ideal-random pyramids, shown in (a) and (b), respectively.

pyramids differs from the measured value by less than 1°, setting an upper bound of

0.25° for the error in the base angle of the AFM map. Some of this error may also arise from a difference in granularity: the angle-resolved reflectance was acquired with 2° steps, whereas the simulations were performed with 0.1° steps. The accuracy of the AFM map was confirmed for all the angles of incidence displayed in Figure 2-3b.

This validation process was next carried out on random-pyramids texture—the primary texture type of interest in this paper. Figure 2-4a shows an AFM map of the surface of a silicon wafer textured with random pyramids, with a maximum pyramid height of approximately 11 μm. The base angle distribution for this map, shown in Figure 2-4c, reveals a peak at 48.9°, considerably lower than the 54.7° value generally assumed in optical simulations of solar cells [48, 49]. Moreover, the distribution is much broader than for real-inverted pyramids (Figure 2-2d). In previous reports, it has been shown that the texturing conditions and use of certain etchants can result in pyramids with average base angle as low as 45° [59, 60, 72, 73]. In Figure 2-4b, the ideal-random pyramid map reconstructed from the real-random pyramid map is displayed, with all base angles equal to 54.7°, as shown in Figure 2-4c.

The total reflectance spectra measured from the sample and simulated from the real-random and ideal-random pyramids maps are compared in Figure 2-5a. The reflectance simulated from the real-random pyramids map has the same profile as the measured reflectance, but with a constant offset of approximately 0.9%. This may be attributed to the finite size of the AFM tip—which rounds sharp features such as peaks and edges—or it may be caused by diffraction from peaks and valleys that are not reproduced with ray optics simulations [69]. In particular, Haug *et al*. found that ray tracing can reproduce the scattering profile from pyramids along the principle axis (the axis parallel to the base of

pyramids) but fails to predict scattering happening due to features along the diagonal

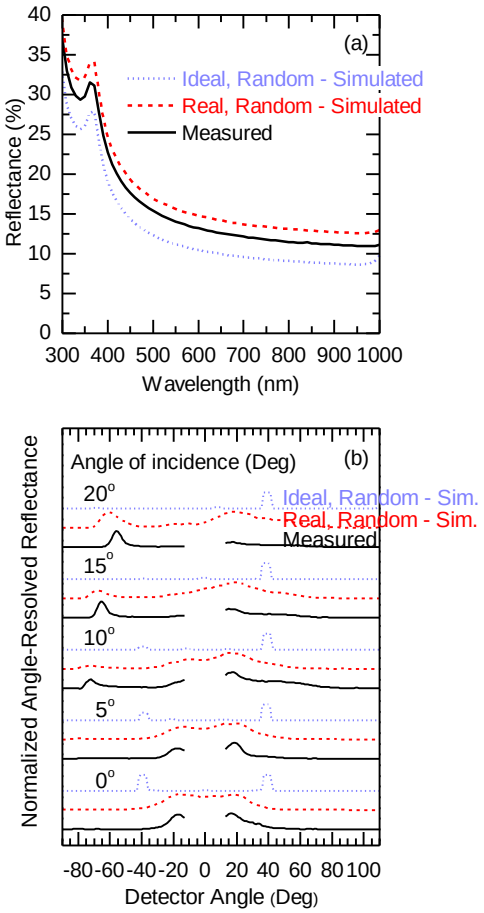

Figure 2-5. Total spectrally-resolved reflectance (a) and angle-resolved reflectance (b) from simulation of ideal-random pyramids, simulation of real-random pyramids, and experimental spectrophotometry measurements.

direction (the axis diagonal to the principal axis) connecting peaks of the pyramids and it is only with a wave-optics approach that such diffractive effects can be correctly accounted for. The simulated reflectance from the ideal-random pyramids map is less representative of the actual sample: the reflectance is approximately 1.5% lower than the measured one throughout the considered wavelength range. This behavior is expected, since real-random pyramids are flatter than ideal-random pyramids, leading to increased reflection.

In Figure 2-5b, the measured angle-resolved reflectance and the simulated reflectances from real-random pyramids and ideal-random pyramids maps are compared. Because of their broad base-angle distribution (Figure 2-4c), real-random pyramids result in broad reflectance peaks in both the measured and simulated cases. For an angle of incidence of 0°, peak reflection is measured at a detector angle of ±17°, which corresponds to a pyramid base angle of 49.3°. In comparison, simulated data from the real-random pyramids map exhibits a peak at ±18.5°, corresponding to pyramid base angle of 49.6°. This compares with a prevalent base angle of 48.9° in the actual sample, as extracted from the AFM map (Figure 2-4c). These are all within 0.7° of each other, suggesting that AFM mapping and ray-tracing simulations do not introduce artifacts that misrepresent the actual pyramids. By contrast, simulations from the ideal-random pyramids map lead to a scattering reflectance peak at ±39.5°, as expected. This emphasizes how inaccurate it can be to assume a 54.7° pyramid base angle when simulating the optics of silicon solar cells.

With increasing angle of incidence, the reflectance peaks measured and simulated from the real-random pyramid map change in concert, though the deviation increases (e.g., on Figure 2-5, the peak near -60° at an angle of incidence of 20°). We hypothesize that this is attributable to electromagnetic effects, as explained by Pla et al [70]. These authors found that the wavelength-to-period ratio—the period being the projected spacing between adjacent pyramids—becomes larger as the sample is tilted and as the area of the pyramids, projected perpendicular to the incident wave-vector, decreases. This moves the sample from the regime of geometric optics to that of wave optics, and, thus, the accuracy of ray-tracing methods decreases.

2.3.2 Comparison of real-random pyramids with a Lambertian scatterer

Having verified that precise AFM measurements yield an accurate height map of the random pyramids, we perform ray-tracing simulations of a monocrystalline silicon wafer, using this map—and the corresponding reconstructed ideal-random pyramids map—for both the top and bottom surface textures. Unless specified otherwise, these simulations are carried out for normal incidence of light. A packet of rays is traced *inside* this textured wafer to explore the (experimentally inaccessible) evolution of the light, in particular the randomization of ray directions following scattering at each surface. We describe this randomization process with a normalized two-dimensional angular distribution function (ADF(θ,ϕ)), that gives the relative light intensity as a function of the polar (θ) and azimuthal (ϕ) angles in spherical coordinates. We condense this information into a unidimensional polar ADF(θ) by integrating over ϕ:

$$ADF(\theta) = \int_0^{2\pi} ADF(\theta, \phi) \sin(\theta) d\phi \tag{3}$$

We then compare the resulting ADF(θ) to that of a Lambertian scatterer, given by:

$$ADF_{Lambertian}(\theta) = \int_0^{2\pi} \frac{1}{\pi} \cos(\theta) \sin(\theta) d\phi \tag{4}$$

From here onwards, "ADF" refers to the unidimensional polar ADF(θ), unless specified otherwise. As mentioned in introduction, two ADFs are of interest: the global ADF (G-ADF) and the local ADF (L-ADF), which are defined with reference to the wafer normal and pyramid facet normal, respectively. The G-ADF is an important metric of phenomena happening at the wafer scale, such as the path-length enhancement due to scattering, while the L-ADF is related to texture-scale phenomena, such as transmission out of the wafer through the escape angle. Both L- and G-ADFs can be reported in two manners. A

"Differential" ADF describes the angular distribution of rays at the end of a given pass, like a snapshot in time. Recording differential ADFs for successive passes thus elucidates how an initial packet of rays scatters inside the wafer over time. The "cumulative" ADF, on the other hand, is the sum of the differential ADFs over an infinite number of passes, weighted by the number of rays remaining within the wafer after each pass. Cumulative ADFs, thus, inform us on the total light intensity scattered into a given angle over the course of a large number of passes. Since the initial passes include the largest number of rays—for example, for a Lambertian scatterer, $1/n^2$ rays escape out the front surface per pass—the initial scattering events are represented strongly in the cumulative ADF.

Here, for both G-ADF (Figure 2-6) and L-ADF (Figure 2-7), we report the differential ADFs for the first 7 interactions with surfaces (the initial transmission and the 6 following reflections) as well as the cumulative ADFs. We show the evolution of ADFs for real- and ideal-random pyramids and compare them to the ADF of a Lambertian scatterer. In these figures 'Pass' represents the number of one-way through-passes completed by the rays—i.e., from the top to the bottom surface, or vice-versa from the bottom to the top surface. The ADFs for Passes 0–6 are, thus, differential ADFs, while the Pass ∞ plot at the bottom of the figures corresponds to the cumulative ADF. As these ADFs are normalized in terms of total light intensity, they can be compared regardless of the light escaping the wafer between passes.

As mentioned earlier, Pass 0 ADFs correspond to the initial transmittance event, showing the global (Figure 2-6) and local (Figure 2-7) angles at which light rays entered the wafer. Thus, these transmittance ADFs compare how efficient different textures are at scattering the incoming light in a single pass through the rough interface. For the following

pass, the ADFs are recorded immediately before the reflection event (i.e. at the “end” of

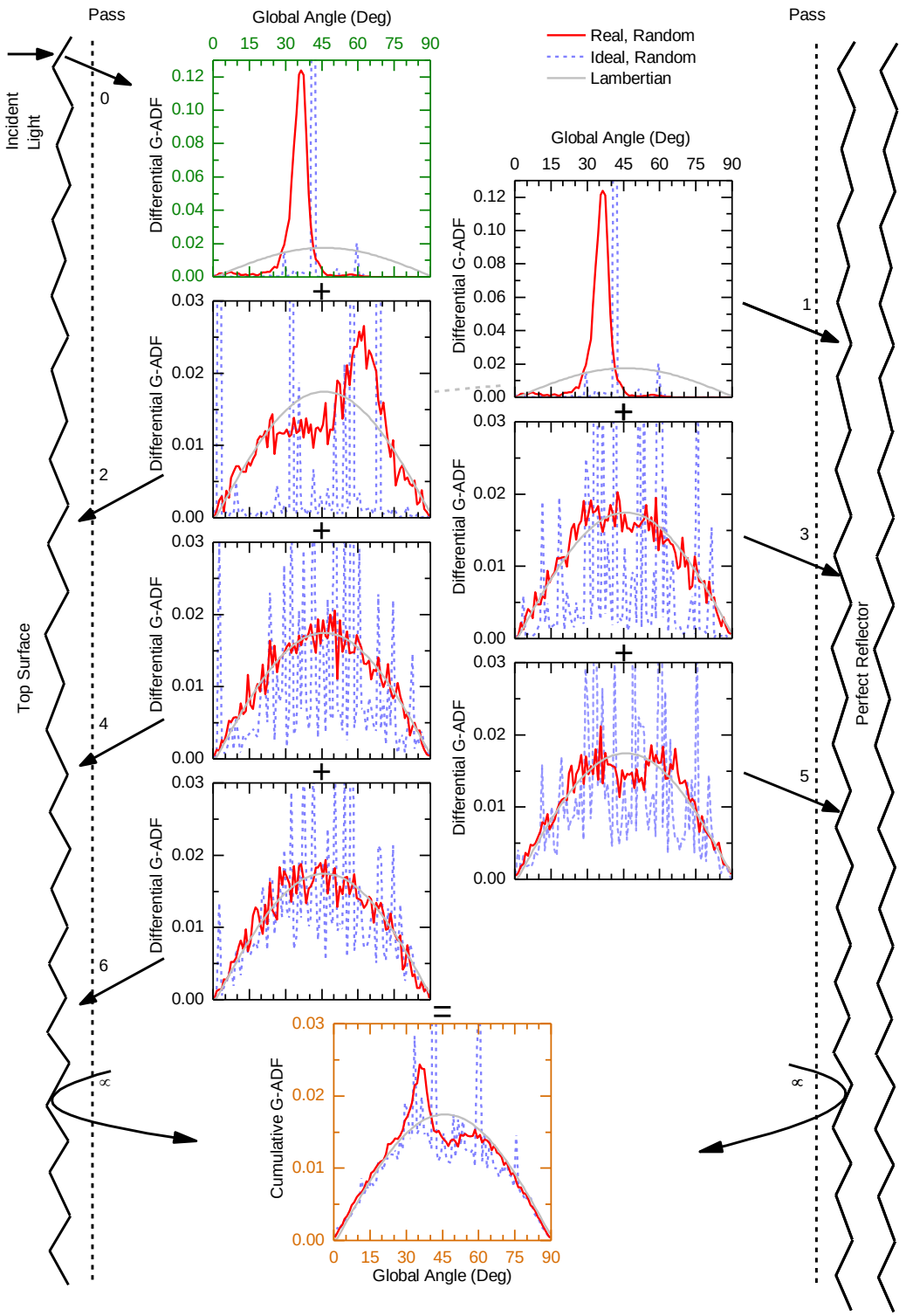
Pass
Global Angle (Deg)
Real, Random
Ideal, Random
Lambertian
Pass
Incident Light
Top Surface
Perfect Reflector
Differential G-ADF
Cumulative G-ADF
Global Angle (Deg)
0
1
2
3
4
5
6
∞
∞

Figure 2-6. Global angle distribution function (G-ADF) evolution versus passes of trapped light rays for normally incident light. The first 7 plots show differential G-ADF, which are snapshots in time that capture the randomization of rays after a particular pass. The vertical dashed lines on each side of the wafer are imaginary planes defined to record the global angles at which trapped rays travel through the wafer. The first plot, for Pass 0, shows the G-ADF of light rays that have just been transmitted into the wafer. The following differential G-ADFs are reported just before the rays hit the surface. Thus, Passes 1, 3, and 5 show G-ADFs of the rays travelling down from the top surface and about to hit the bottom surface; while Passes 2, 4, and 6 show G-ADFs of rays about to hit the top surface. The last plot shows the cumulative G-ADF, computed by summation of all the prior differential G-ADFs—weighted by the number of rays remaining within the wafer at each pass—for a large number of passes. Thus, this last plot reveals the total path-length enhancement.

the pass). Hence, odd passes (1, 3 and 5) correspond to rays travelling down from the top surface and about to hit the bottom surface and, conversely, even passes (2, 4 and 6) correspond to rays travelling up from the bottom surface and about to hit the top surface. As a result, the G-ADFs (Figure 3-6) for Pass 0 and 1 are the same, since the global angle ADF does not change between the initial transmission and the first reflection. Note, though, that this is not true from a local perspective, as shown on the L-ADF (Figure 2-7).

Pass 0 is arguably the most important opportunity to maximize the path length of the light coupled-in the wafer, before any of it can be lost to parasitic absorption in the back reflector or escape reflection through the front surface. As shown in Figure 2-6, the G-ADF for Pass 0 exhibits peaks at 41.5° and 36.5° for ideal-random and real-random pyramids, respectively, thus offering a greater path length for the former. In a 180-μm-thick silicon absorber, considering light in the 1000-1200 nm wavelength range, this difference in first-pass path length would lead to 0.13 mA/cm^2 additional photocurrent generated during the first pass with ideal-random pyramids.

It thus appears that the smaller base angles of real-random pyramids are detrimental, as they reduce the path length of the first pass compared with ideal-random pyramids.

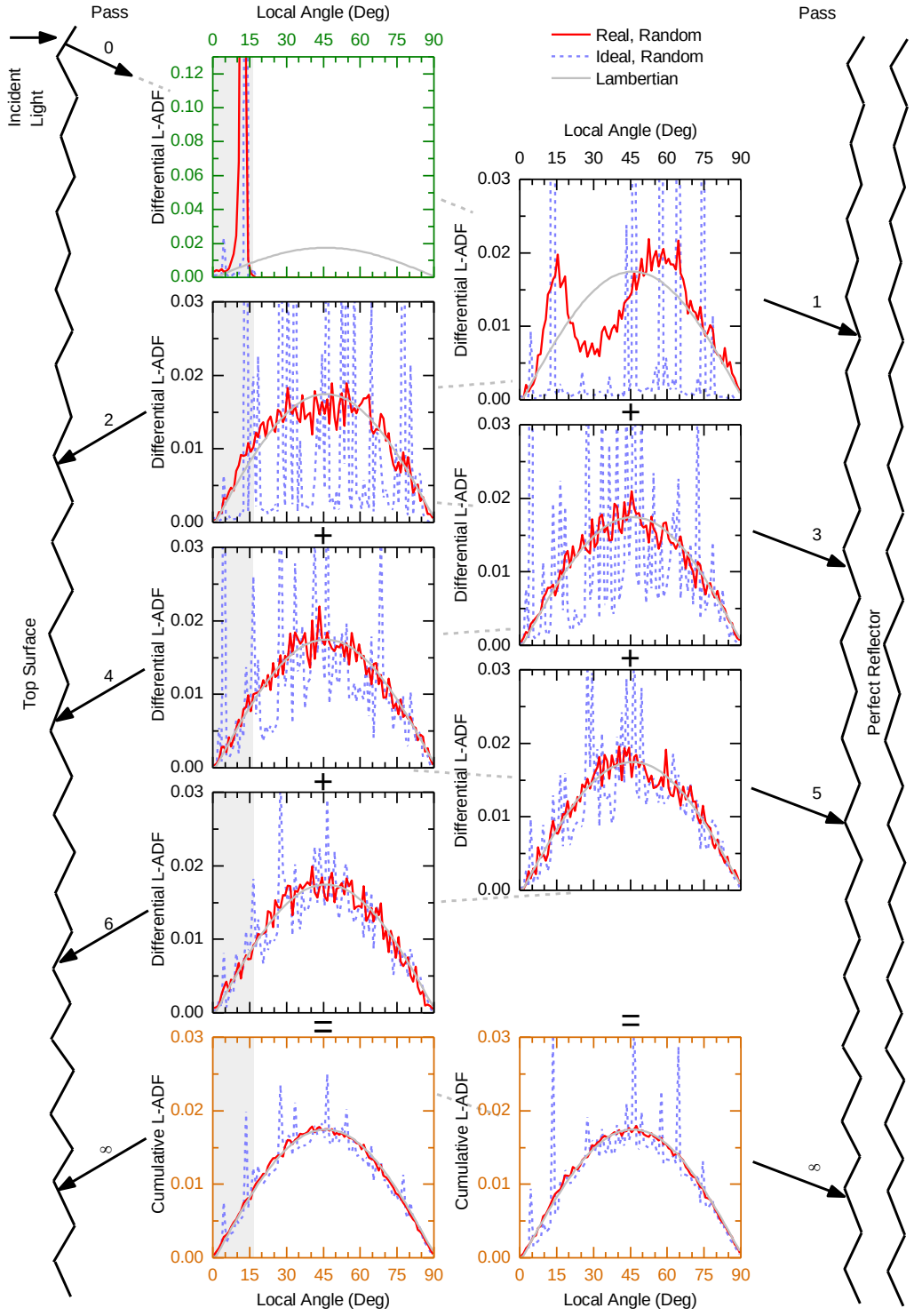
Pass
Local Angle (Deg)
Real, Random
Ideal, Random
Lambertian
Pass
Incident Light
Top Surface
Perfect Reflector
Differential L-ADF
Cumulative L-ADF
0
1
2
3
4
5
6
∞
0 15 30 45 60 75 90
0.00 0.01 0.02 0.03
0.00 0.02 0.04 0.06 0.08 0.10 0.12

Figure 2-7. Local angle distribution function (L-ADF) evolution versus passes of trapped light rays for normally incident light. The first 7 plots show differential L-ADF, which are snapshots in time that capture the randomization of rays after a particular pass. The first plot, for Pass 0, shows the L-ADF of light rays that have just been transmitted into the wafer. The following differential L-ADFs are reported just before the rays hit the surface. Thus, Passes 1, 3, and 5 show L-ADFs of the rays travelling down from the top surface and about to hit the bottom surface; while Passes 2, 4, and 6 show L-ADFs of rays about to hit the top surface. The last two plots are showing cumulative L-ADFs for the top and bottom surfaces, respectively. Cumulative L-ADFs are computed by summation of all the prior differential L-ADFs for the respective surface— weighted by the number of rays remaining at each pass—for a large number of passes. Therefore, cumulative L-ADF plots for the top surface reveals the total light that falls into the escape cone—displayed in light blue shading in the front-surface L-ADF plots—and contributes to escape reflection. Similarly, cumulative L-ADF for the bottom surface informs us on the total parasitic absorption in the back reflector.

However, as we show hereafter, the *distribution* of base angles is an advantage, as it is more efficient in randomizing the light. This can be seen in Pass-1 G-ADF: ideal-random pyramids exhibit a narrow peak, as opposed to a broader G-ADF peak for real-random pyramids. As a result, light rays hit the back surface with a wider distribution of angles for real-random pyramids. This is also visible in Figure 2-7: the L-ADF for ideal-random pyramids consists in a concatenation of narrow peaks, whereas real-random pyramids lead to a broad ADF covering the full 90°. Since the back surface of solar cells is engineered to be highly reflective (here we assume R=1), there is a negligible reduction in total light intensity between Pass 1 and Pass 2. Hence, the inferior Pass-1 path length with real-random pyramids can be counter-balanced during Pass 2. Indeed, Pass-2 G-ADF is broad for real-random pyramids—thus, more randomized—while ideal-random pyramids G-ADF presents sharp peaks at high θ angles (e.g. 57° and 68°), but also at very low angle (2°). Hence, a sizable portion of light travels back nearly perpendicular to the wafer. This light barely experiences any path-length enhancement.

This can also be inferred from the G-ADF root-mean-squared deviation (RMSD) from

a Lambertian behavior, displayed after each pass in Figure 2-8a and calculated according to:

$$RMSD = \sqrt{\frac{\int_{\theta=0}^{\theta=\pi/2}\left(ADF(\theta) - ADF_{Lambertian}(\theta)\right)^2}{\pi/2}} \tag{5}$$

and the average path-length enhancement (PLE) *per pass*, shown in Figure 2-8c and given by:

$$a = \int_0^{\pi/2} ADF(\theta)\frac{1}{\cos(\theta)}d\theta \tag{6}$$

For real-random pyramids, the deviation of the G-ADF is maximal for Pass 1, before dropping close to zero following the subsequent passes (Figure 2-8a). As a result, real-random pyramids have a relatively low PLE of 1.23 for Pass 1. However, following Pass 2, the PLE reaches and maintains the value of 2—the PLE per pass of a Lambertian scatterer—as shown in Figure 2-8c. In contrast, ideal-random pyramids exhibit a higher PLE of 1.34 for Pass 1, but the PLE remains lower than 2 for the next couple of passes and only matches the performance of a Lambertian scatterer at Pass 4. Unsurprisingly, for ideal-random pyramids, both G- and L-ADF remain non-Lambertian until approximately Pass 8. Yet, the PLE per pass reaches 2 at Pass 4, thus demonstrating that the distribution of rays does not have to be Lambertian for the structure to perform as efficiently as a Lambertian scatterer. Similar results have been reported by Boccard *et al.*.[74] Their analytical model—which yielded good agreement between calculated and measured short-circuit current density and external-quantum-efficiency—relies on a similar observation: they assumed a non-Lambertian light scattering, with an average path length per pass below 2, for the first round-trip and a Lambertian light distribution for subsequent passes.

The cumulative G-ADF (Pass ∞, at the bottom of Figure 2-6) captures the overall texture performance in terms of PLE per pass. The peaks from the initial transmission (Pass 0), at 41.5° for ideal-random pyramids and 36.5° degrees for real-random pyramids, are still apparent, thus highlighting the importance of the first scattering event. More importantly, the cumulative G-ADF shows that, although both textures are eventually able to randomize the light, the Lambertian assumption—commonly used to calculate the path-length enhancement—is not entirely true for neither real-random pyramids nor ideal-random pyramids; however, the distribution for real-random pyramids is markedly closer to the Lambertian model.

In addition to maximizing the path-length enhancement through the wafer, minimizing escape reflection by scattering the rays away from the escape cone is a necessary component of a highly performant light-trapping scheme. As mentioned earlier, this information, which relates tightly to the angle at which the incoming rays hit the pyramid facet, can be accessed by studying the L-ADF (Figure 2-7). Results are reported for real- and ideal-random pyramids, just before rays hit the surface. For even Passes, this informs us on the amount of light within the escape cone (ca. 16.6° for air-silicon interface) that is about to be transmitted through the top surface. Similarly, for odd Passes, it shows the amount of light potentially parasitically absorbed in the rear reflector, which varies with the local angle of incidence.[61, 62, 66] The L-ADFs of light rays following reflection are displayed in Appendix:A.

As shown on Figure 2-7, for both textures, the packet of light rays enters the wafer with a distribution of local angles within the escape cone, in agreement with Snell's law. However, after one round-trip back to the front surface (Pass 2), real-random pyramids

scatter the rays away from the escape cone (shown in light blue shading), with an angle

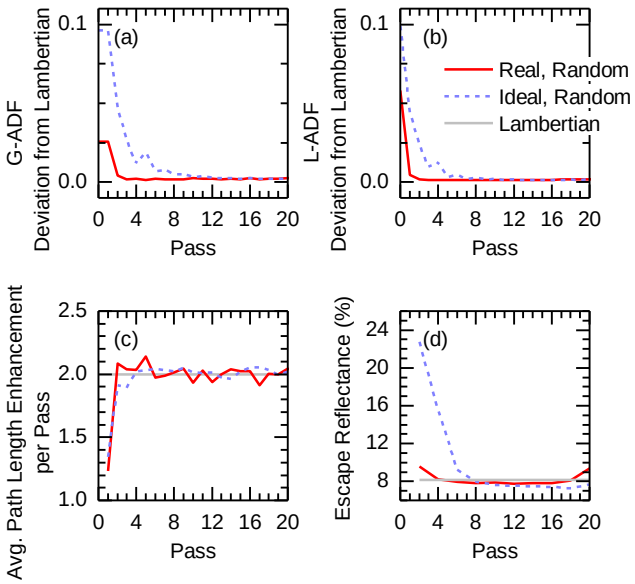

Figure 2-8. Deviations of the G-ADF (a) and L-ADF (b) from a Lambertian behavior as a function of the number of passes. These deviations are defined as the root-mean square difference. (c) Average path-length enhancement per pass, calculated from the differential G-ADFs. (d) Escape reflection at each pass calculated from the differential L-ADFs. These results are for normal incidence of light.

distribution close to Lambertian. In comparison, for ideal-random pyramids, a large amount of light reaches the front surface with a local angle within the escape cone. Again, we attribute this divergence to the difference in base-angle distributions. With ideal-random pyramids, facets from the top and bottom surfaces are parallel. As light rays are initially transmitted into the wafer nearly perpendicular to the pyramid facet, with a local angle within the escape cone, the chance of a ray hitting the back surface nearly perpendicular to the pyramid facets there is non-negligible. The same process on the way back to the front surface allows a large portion of the light to hit back the front pyramids facet nearly perpendicular, within the escape angle. For real-random pyramids, the broad

distribution of pyramid base angles strongly reduces the probability of such events. As a result, as shown in Figure 2-8b—displaying the deviation of L-ADF from a Lambertian behavior, calculated using (4)—ideal-random pyramids take 8 passes to achieve a Lambertian distribution, while it only takes 2 passes for real-random pyramids to get there.

This difference in behavior is also apparent in Figure 2-8d, which shows the fraction of light escaping each time the rays reach the top surface, given by:

$$b = \int_0^{\theta_c} T_{ARC}(\theta) ADF(\theta) d\theta \tag{7}$$

with θ_c the critical angle and T_{ARC} being the transmission of the top surface with a value of unity for angles of incidence within the escape cone. For a Lambertian scatterer, the fraction of rays that escape is $1/n^2$, with n the refractive index of the absorber material. As a result, assuming n=3.5 for silicon, b=8.2% with a Lambertian surface. In comparison, for ideal-random and real-random pyramids, the first internal reflection event on the front surface (Pass 2) leads to 22.7% and 9.6% of light rays transmitted through the escape cone, respectively. Considering light in the 1000-1200 nm range and a 180-µm-thick silicon absorber, these first-escape losses amount to 1.1, 0.45, and 0.37 mA/cm^2 photocurrent losses for ideal-random pyramids, real-random pyramids, and a Lambertian scatterer, respectively. For subsequent internal reflection events on the front surface (even Passes), the escape fraction remains consistent at 7.69±0.64% for real-random pyramids. This compares to escape fractions of 15.6% for Pass 4, 9.3% for Pass 6, and 7.30±0.47% for the following even Passes, for ideal-random pyramids.

Cumulative L-ADF (Pass ∞) is split into two in Figure 2-7; separate plots are shown for the light reaching the front and rear surfaces. This segregation allows isolation of two

distinct loss mechanisms: escape loss through the front surface and parasitic absorption in the rear reflector. The front surface cumulative L-ADF highlights that ideal-random pyramids lose more light through escape transmission at the front surface than real-random pyramids and Lambertian scatterers. Moreover, the real-random pyramids front cumulative L-ADF is close to Lambertian; therefore, a Lambertian model can safely be used to calculate the escape loss from a wafer textured with real-random pyramids.

Cumulative L-ADF at the back surface determines parasitic absorption in the rear reflector. Holman *et al.* have demonstrated that parasitic absorption in a rear contact (silicon/indium-tin-oxide/silver) depends extensively on the angular distribution of light hitting it, this distribution itself being a strong function of the texture morphology [62]. The rear surface cumulative L-ADF in Figure 2-7 shows that the Lambertian assumption for light rays hitting the bottom surface is justified for real-random pyramids and, to some extent, for ideal-random pyramids. More precisely, in the ideal-random pyramids case, care should be taken as the ADF displays sharp peaks at certain angles. If these angles coincide with absorption peaks for the particular rear contact configuration under study; the Lambertian assumption may not be true.

Taken together, the path-length enhancement per pass, the escape reflection through the front surface, and the parasitic absorption in the rear reflector determine the total path-length enhancement. This common light-trapping metric is closely related to the total photogenerated current density. So far we have compared the textures with Lambertian scatterer at normal incidence of light but to perform comparison with the $4n^2$ Lambertian limit, they have to be examined under isotropic illumination or at various angles of incidence. According to Equation 1, *average* total path length enhancement could be

greater than $4n^2$ at restricted angles but when averaged over many angles of incidence, it

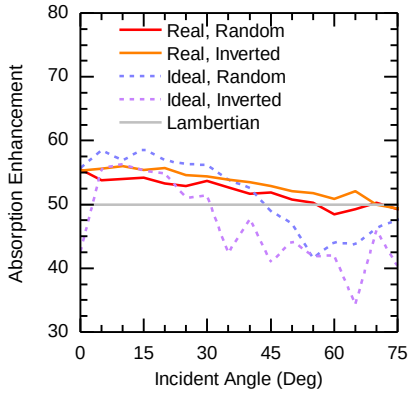

Figure 2-9. Total path-length enhancement of the textures investigated, calculated at a light wavelength of 1200 nm, for various incident angles.

must have a maximum value of $4n^2$. Therefore, the *average* total path-length enhancement for simulated real-random, real-inverted, ideal-random, and ideal-inverted pyramids are compared with a Lambertian scatterer in Figure 2-9, for incident angles between 0° and 75°, with a 5° step. Real-random and real-inverted pyramids both outperform the Lambertian scatterer at all incident angles but 75° for real-inverted pyramids and 60°, 65°, and 75° for real-random pyramids. In comparison, ideal-inverted and ideal-random pyramids exceed the Lambertian performance over a narrower incident-angle range: 0° to 30° and 0° to 45°, respectively. At higher incident angles their performance significantly drops, below that of a Lambertian scatterer.

First, we discuss the *average* total path-length enhancement at θ=0°, and compare it with the results detailed earlier in the manuscript. The path-length enhancement θ=0° can appear counter-intuitive, as we have previously shown that—compared with a Lambertian scatterer—real- and ideal-random pyramids underperform in terms of both average path-length enhancement per pass and escape reflectance for the first couples of passes.

However, both these surface textures offer a lower escape reflectance for later passes (as shown in Figure 2-8d). Thus, compared with a Lambertian scatterer, a higher number of rays remains within the wafers in the long run. As a result, more rays are lost early, and these rays travel a shorter path, but the remaining rays are retained longer within the wafer, hence contributing to the stronger total path-length enhancement. In addition, the cumulative G-ADF plot (Pass ∞) for ideal-random pyramids in Figure 2-6 (light blue – dashed) shows strong peaks at 60° and 75°, indicating that a non-negligible portion of the rays travels longer per pass than in the Lambertian case. This contributes to recovering for the loss of rays in early passes. Campbell *et al.*, has observed similar results in terms of rays remaining: ideal-regular and ideal-random pyramids lose more rays through escape reflection in early passes but, after enough passes, both textures retain more rays than a Lambertian scatterer, thus leading to comparable *average* path-length enhancement [34]. Similar results have been obtained by Brendel: at normal incidence, for some relatively simple texture schemes, path-length enhancement values exceeding 100 are possible, which is considerably higher than the Lambertian limit [54].

Now considering the complete range of angles of incidence, the Lambertian limit is considered a light-trapping performance limit. However, it is important to keep in mind that—with relatively standard surface textures—Lambertian scatterers can be outperformed for a restricted range of incident angles [54]. This result is consistent with light-trapping physics, provided that, once averaged over the full range of incident angles (0°–90°), the path-length enhancement remains below or equal to the $4n^2$ limit [55, 57]. Hence, exceeding the Lambertian limit for some incident angles is counterbalanced by a reduced total path-length enhancement at other angles. We demonstrate such cases of

angular selectivity for the surface textures we presently investigate [58]. Similar results have been reported by Campbell *et al.*, showing that (ideal) perpendicular slats can exceed the $4n^2$ Lambertian limit when light is incident within 30°–45° of the wafer normal [34]. Considering the full range of incident angles, Brendel has shown that various textures (e.g. pyramids, simples prism pyramids, and grooves) all achieve $4n^2$ limit under isotropic illumination [33].

In contrast, using spectral photoluminescence techniques, Barugkin *et al.*, have measured light-trapping efficiencies (LTEs) considerably lower than the Lambertian limit for different textures—including random pyramids—on silicon wafers. We attribute this difference to the definition used for "light trapping" and to the experimental apparatus used. Their definition of LTE includes absorption contributions from "parasitic absorption" in accompanying layers; while the correct definition of "light trapping" due to a texture is the path-length enhancement over the planar case in complete absence of absorption [31, 32]. Schuster *et al.* have similarly calculated low LTE values when accounting for parasitic absorption [32]. Moreover, during PL measurements, Barugkin *et al.* used a detached back reflector with reflectance R>95%. This lower bound on R is inadequate, leading to considerable parasitic absorption and, consequently, low LTE values [31]. Indeed, Deckman *et al.* have shown that, with just 6% of parasitic absorption, the absorption enhancement already drops to half of the Lambertian limit [75]. Therefore, the correct way to assess the light trapping in the presence of parasitic absorptance would be to eliminate its contribution by dividing it between external quantum efficiency (EQE) and reflectance according to the method described by Holman *et al.*,[27]. Using this method, Holman *et al.*, has shown that the experimental EQE of a crystalline silicon solar cell with random-

pyramids texture is very close to simulations assuming a Lambertian behavior. We are, thus, confident in the high path-length enhancement data reported in the present work.

2.4 Conclusion

There have been contradictory reports over the last three decades about the light-trapping performance of random-pyramid texture on crystalline silicon wafers, from the actual base angles of the pyramids to their impact on light trapping. In this work, using AFM, we recorded accurate three-dimensional height maps of textured silicon wafers. Real random pyramids exhibit a wider distribution of base angles than expected from theory, with a peak below the 54.7° theoretical value. This deviation has important implications on their light-trapping performance. Through ray-tracing simulations based on these *real-random* maps, as well as reconstructed *ideal-random* maps featuring ideal pyramids with 54.7° base angles, we demonstrated that the broader base-angle distribution of real-random pyramids yields superior scattering performance. Thus, an ergodic distribution of light rays within the wafer—typical of Lambertian scatterers—is reached after fewer bounces than in the ideal-random pyramids case: 2 passes through the wafer versus 4. Similarly, the escape reflection is lower with real-random pyramids and is in fact lower even than the Lambertian case after five passes through the wafer. Finally, we showed that the total path-length enhancement provided by real-random pyramid textures exceeds the $4n^2$ Lambertian case for a restricted range of incident angles, counterbalanced by sub-Lambertian performance at higher angles. Hence, real-random pyramid textures exhibit an angle-selective behavior, which does not violate the physics of light trapping. Perhaps most important, ideal-random pyramids with 54.7° base angles offer a poor approximation of the behavior of actual textured wafers. A simple Lambertian assumption is a better

approximation, particularly if coupled with an exceptional (non-Lambertian) first pass in which all light is assumed to travel towards the rear of the wafer at 36.5° with respect to the wafer normal.

The framework we present in this contribution can be applied to other surface textures, include mathematically generated artificial textures, provided that the size of features does not preclude the use of geometric optics. Similarly, parasitic absorption and imperfect anti-reflection coatings can be incorporated into the optical simulations to treat particular cases of interest. Angular distribution functions are a powerful tool to investigate the evolution of light within a substrate, as they provide insight into the underlying mechanism(s) responsible for lumped behavior, such as poor photocurrent within a textured solar cell. Small variations in the features of actual textures, relative to the intended design texture, may appear insignificant in a topographical map, but their pronounced effect on the evolution of trapped light becomes apparent in simulated angular distribution functions.

CHAPTER

3 IMPROVED LIGHT MANAGEMENT IN PLANAR SILICON AND PEROVSKITE SOLAR CELLS USING PDMS SCATTERING LAYER

3.1 Introduction

Solar cells suffer from Fresnel reflection losses as light traverses the interfaces between the incident medium—air—and the absorbing medium—typically a high-refractive-index semiconductor. Some solar cells mitigate this loss with microscale textures that are defined in the absorbing medium and that scatter incoming light into, rather than away from, the cell. Most notably, monocrystalline silicon solar cells have random upright pyramid features, with characteristic dimensions of 1–10 μm and base angles of approximately 50° [34, 71], that form during alkaline etching, and multicrystalline silicon solar cells have "spherical cap" pits with similar characteristic dimensions that form during acidic etching [76, 77]. Other solar cells, like thin-film silicon cells deposited on grown or etched textured ZnO layers [78-80], employ sub-wavelength textures to reduce front-surface reflection via refractive-index grading.

For many other solar cells, however, it is inconvenient or impossible to texture the absorber layer. For example, the best perovskite solar cells are presently deposited from solution, and attempts to accommodate non-planar substrates that would impart their texture to the perovskite layer have thus far decreased conformality and degraded cell performance [81-84]. III-V cells are grown epitaxially on polished, lattice-matched substrates, and etching the absorber to define scattering features both would be impractical and would inhibit subsequent growth of epitaxial passivation and contact layers. Even

polycrystalline thin-film solar cells, such as a CdTe and CIGS, are commonly grown on near-planar substrates and do not themselves develop much texture during growth; growth of polycrystalline films on highly textured substrates can create voids in the material, resulting in poor device performance or even shunting [85-88].

Reflective flat surfaces are also not unique to single-junction cells. All *modules* with planar front glass incur a minimum 4% reflectance loss at the air/glass interface for normally incident light (and 5.6% over the course of a year in Phoenix for an ideally mounted fixed-tilt module), regardless of the reflectance of the cells encapsulated therein. In addition, tandem cells (and modules) are rapidly improving as concepts pioneered in III-V multi-junction devices and thin-film silicon tandems are adapted to, e.g., top-cell/Si tandems and perovskite/perovskite tandems [16, 89, 90], yet most have flat front surfaces and thus reflection is a primary efficiency limiter [19, 37-39, 45, 91]. This loss can be particularly detrimental in two-terminal tandems, as reflection is often not constant across the full spectrum and thus influences current matching [92, 93].

One approach to mitigate reflection losses in planar cells and modules is to apply anti-reflection coatings (ARCs) comprised of dielectric or transparent conductive oxide layers [94-98]. However, Sai et al., Escarre et al., and Song et al. have shown that textured surfaces are better at reducing reflection over a wide spectral range and broad range of angles of incidence, as is seen by (flat-plate) cells in the field, than ARCs—even multi-layer ARCs [35, 36, 44, 99]. For example, two-terminal planar perovskite/Si tandem cells reported in the literature had approximately 7.7 mA/cm^2 and 8.7 mA/cm^2 reflectance loss (between 350 nm and 1100 nm), despite having single-layer indium tin oxide (ITO) or indium oxide (IO:H) ARCs [37, 38]. We previously reported a similar tandem with a

double layer LiF/ITO ARC, yet the remaining 4.8 mA/cm^2 reflection loss remained the largest optical loss in the 23.6%-efficient device [19]. Similarly, a recent 30.2%-efficient GaInP/$Al_xGa_{1-x}As$/Si triple-junction solar cell with a Ta_2O_5/MgF_2 double-layer ARC lost a significant 3.9 mA/cm^2 to reflection [39].

Planar solar cells and modules would greatly benefit from a scattering texture that could be added after cell completion; such a texture could even potentially enhance light trapping, which is important in silicon cells that only weakly absorb near-bandgap wavelengths, in addition to mitigating front-surface reflectance. To this end, others have proposed several approaches to impart textures to transparent substrates or films that are then attached to planar cells. For example, a freestanding textured PMMA sheet produced via hot embossing was applied to the front of polycrystalline silicon solar cell which successfully reduced reflectance loss from 11.9 mA/cm^2 to 4.3 mA/cm^2 [42]. An anti-reflection foil carrying a retroreflective texture pasted on the top surface of a two-terminal perovskite/silicon tandem cell similarly reduced the reflectance loss from 9.2 mA/cm^2 to 4.7 mA/cm^2, and a foil pasted on the front glass of an amorphous silicon/microcrystalline silicon tandem module reduced the reflectance loss from 7.9 mA/cm^2 to 4.0 mA/cm^2 [37, 100]. Nano-imprint lithography in UV-curable lacquer (UV-NIL) was utilized to produce textures on glass substrates that were then placed at the front of planar cells [40, 43, 44, 101]. With this method, the random pyramid texture of monocrystalline silicon wafers was transferred to thin-film silicon and perovskite solar cells, increasing the short-circuit current density (J_{sc}) by 0.5 mA/cm^2 and 1.0 mA/cm^2, respectively [44, 101]. These examples demonstrate the efficacy of transparent textured layers, but the limits of the approach have yet to be investigated. In particular, the scattering layers have not been

benchmarked against best-in-class control samples, such as solar cells with the same texture defined *in* the absorber, and their effects on front-surface reflection, parasitic absorption, and escape reflection have not been parsed.

In this contribution, we explore these limits by using UV-NIL to replicate the random pyramid texture of monocrystalline silicon solar cells in polydimethylsiloxane (PDMS) layers. We chose PDMS for scattering layer because it is a strong contender to be used as an encapsulant in advanced modules, due to its right refractive index as well as its stability under extended damp-heat conditions [102, 103]. Random pyramids are chosen because they afford excellent light management and because comparison with silicon solar cells in which the silicon has the same texture is illustrative [34, 104]. Accordingly, silicon heterojunction solar cells with no, one, or two textured surfaces are used as a model system with which the light scattering of two different materials (the silicon itself and PDMS layers placed on the front of the cells) carrying the same texture is quantitatively characterized. A scattering layer is then tested on a solar cell that cannot be easily textured—a planar perovskite cell.

3.2 Materials and Methods

Silicon heterojunction solar cells were fabricated using three 250-µm-thick, *n*-type, float-zone silicon wafers with a resistivity of 1–4 Ωcm. The wafers were double-side polished as received. One wafer remained double-side polished, another was textured on only the rear surface, and the third was textured on both surfaces. Texturing was performed in a potassium hydroxide (KOH) solution containing an additive from GP Solar, which revealed random upright pyramids 2–5 µm in size. To texture only the rear of the single-side textured wafer, the polished front surface was first coated with a 250-nm-thick silicon

nitride (SiN_x) layer that resists KOH etching. The layer was deposited with an AMAT P5000 plasma-enhanced chemical vapor deposition (PECVD) tool at 250 °C. After texturing, the SiN_x layer was removed in dilute hydrofluoric acid, and this wafer joined the double-side textured wafer for cleaning in piranha and RCA-B solutions. All three wafers were then dipped in buffered oxide etch to remove any oxide prior to loading into the PECVD tool. Intrinsic and *n*-type amorphous silicon (a-Si:H) layers 6 nm and 5 nm thick, respectively, were deposited on the front (sunward) side, and intrinsic and *p*-type a-Si:H layers 6 nm and 11 nm thick, respectively, were deposited on the rear side. The deposition times were adjusted to achieve the same layer thicknesses on polished and textured surfaces. A 115-nm-thick indium tin oxide (ITO) layer was then sputtered from a 90/10 indium oxide/tin oxide (In_2O_3/SnO_2) target in an MRC 944 tool on the front side through a shadow mask that defined 4 cm^2 cells. This is the near-optimum front ITO thickness when silicon is used as bottom cell in a four-terminal tandem and captures only IR light [105]. A 144-nm-thick ITO layer and a 200-nm-thick silver layer were next sputtered on the entire rear side. Finally, a front grid electrode was defined by screen-printing low-temperature silver paste, and the cells were annealed at 200 °C for 20 mins to cure the paste.

A perovskite solar cell was fabricated on ITO-coated glass. First, 10 nm of PTAA was spun from a 5 mg/ml solution in chlorobenzene on the ITO/glass substrate, followed by spin-coating of a 500-nm-thick perovskite layer. The perovskite precursors were PbI_2, $PbBr_2$, FAI and CsI dissolved in 4:1 DMF:DMSO. Next, 1 nm of LiF and 10 nm of C60 were thermally evaporated on top of the perovskite, and a window layer consisting of 4 nm of tin oxide (SnO_2) and 2 nm of zinc-tin-oxide was deposited by atomic layer deposition (ALD). This was followed by a 150-nm-thick-ITO layer deposited by sputtering. Finally,

a silver grid was thermally evaporated on top of the cell to finish the device. A schematic of the cell structure is shown in Fig. 3-5a and further details on the ALD and ITO depositions are given in reference [19].

PDMS scattering layers were made with Sylgard 184 from Dow Corning. The base and curing agent were mixed in a 10:1 ratio and then diluted with toluene in a 10:1 weight ratio. This mixture was then degassed in vacuum before dispensing onto silicon wafers that had been dipped in toluene for 1 min and that had the same random pyramid texture as the silicon heterojunction cells described above [106]. The PDMS was cured at 46 °C for 12 h and carefully separated by hand from the silicon wafer to reveal the negative of the random pyramid texture.

External quantum efficiency (EQE) and reflectance measurements were performed on cells before and after attachment of PDMS to study wavelength-resolved changes in absorption and reflection resulting from scattering. Refractive-index-matching fluid was used to attach the PDMS layers to the polished front surfaces of cells so as to avoid formation of an air gap and the associated extra reflectance. EQE measurements were recorded over the 300–1200 nm wavelength range using a PV Measurements QEX10 tool. The total reflectance was measured over the same wavelength range using a PerkinElmer Lambda 950 spectrophotometer equipped with an integrating sphere. The angle of incidence was 7° from the wafer normal. The angular-resolved reflectance was measured using an Automated Reflectance/Transmittance Analyzer (ARTA) accessory that connects to the spectrophotometer and utilizes independent sample and detector goniometers [107, 108]. Note that, for normally incident light, the angle-resolved reflectance cannot be measured for -12° to 12° detector angles because the detector is blocked by the light source.

Complementary EQE and reflectance simulations were performed using the Module Ray Tracer (MRT) software from PV Lighthouse [109]. This software combines Monte Carlo ray-tracing with thin film optics. MRT allows texturing of any surface with random pyramids with arbitrary base angle. In our simulations, random pyramids were simulated with a base angle of 50.5° for textured silicon and 49.5° for PDMS scattering layers—the angles found via the angular-resolved reflectance measurements. The simulations also take layer thicknesses and complex refractive indices as input; these were determined for each layer individually using simultaneous fitting of spectroscopic ellipsometry and transmittance data (for a-Si:H layers) or spectroscopic ellipsometry and reflectance data (for ITO layers). Ellipsometry spectra were recorded with a JA Woollam M2000 instrument for an angle of incidence of 70° and a wavelength range of 300–1700 nm; transmittance and reflectance spectra were recorded with the Lambda 950 spectrophotometer. The a-Si:H layers were deposited on glass and fit using a Tauc-Lorentz dispersion relation, whereas the ITO layers were deposited on a-Si:H *i*/*n* stacks on polished silicon wafers (the hydrogen in the a-Si:H layers alters the ITO properties upon annealing and thus it is preferable to characterize structures similar to those in the cells of interest) and fit using a combined Tauc-Lorentz and Drude dispersion relation [110]. The complex refractive indices of monocrystalline silicon and silver (Ag) were taken from literature [111, 112].

3.3 Results and Discussion

Silicon heterojunction solar cells were fabricated on wafers with three surface textures that, together, elucidate the effects of textured PDMS scattering layers on planar-front-surface solar cells via direct comparison to cells carrying the same texture *in* the silicon.

Schematics of these three cell structures are shown in Figure 3-1. The first device has planar front and rear surfaces and is labeled “Flat/Flat,” the second device has a planar front surface and a textured rear surface and is labeled “Flat/Tex,” and the third device has textured front and rear surfaces and is labeled “Tex/Tex”. As also shown in Figure 3-1, the prefix “PDMS” is added to a device’s name when the device carries a PDMS layer at its front surface. Comparison of the Flat/Flat, Tex/Tex, and PDMS/Flat/Flat devices reveals the efficacy of PDMS layers in reducing front-surface reflectance, relative to the present state of the art in textured monocrystalline solar cells. Comparison of Flat/Tex, Tex/Tex, PDMS/Flat/Flat, and PDMS/Flat/Tex devices reveals the efficacy of PDMS layers in trapping long-wavelength infrared light, again relative to the state of the art.

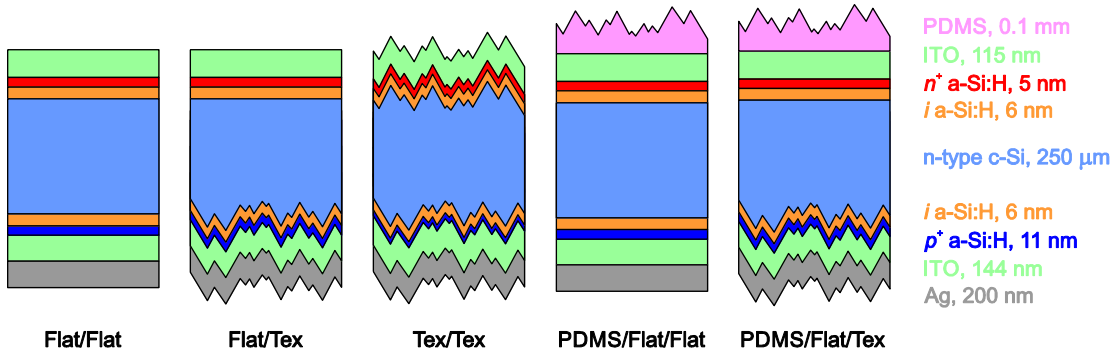

Figure 3-1. Schematic diagrams of the five samples that were investigated, which comprise three silicon heterojunction solar cells, two of which (Flat/Flat and Flat/Tex) were measured without and with PDMS scattering layers affixed to their front surfaces.

3.3.1 Simulations

To quantify the contribution of individual optical loss mechanisms—in particular, front-surface reflection, escape reflection, and parasitic absorption—we simulated the structures depicted in Figure 3-1. Figure 3-2a shows the simulated EQE and reflectance for Flat/Flat, Flat/Tex and Tex/Tex devices (no PDMS scattering layers) and Figure 3-2c gives the

breakdown of the optical losses in terms of equivalent J_{sc}. As a reference, Figure 3-2c also includes the loss breakdown results for an "ideal cell" that has perfect transmission of incoming light at its front surface, no parasitic absorption, and a perfect Lambertian rear reflector. Integrating over all photons in the AM1.5G spectrum with wavelengths between 300 nm and 1200 nm, the J_{sc} of this ideal cell is 44.1 mA/cm^2. The only "loss," of 2.2 mA/cm^2, corresponds to infrared light that enters the cell but escapes back out the front surface (escape reflectance); no solar cells of finite thickness can absorb all photons with above-bandgap energies [113].

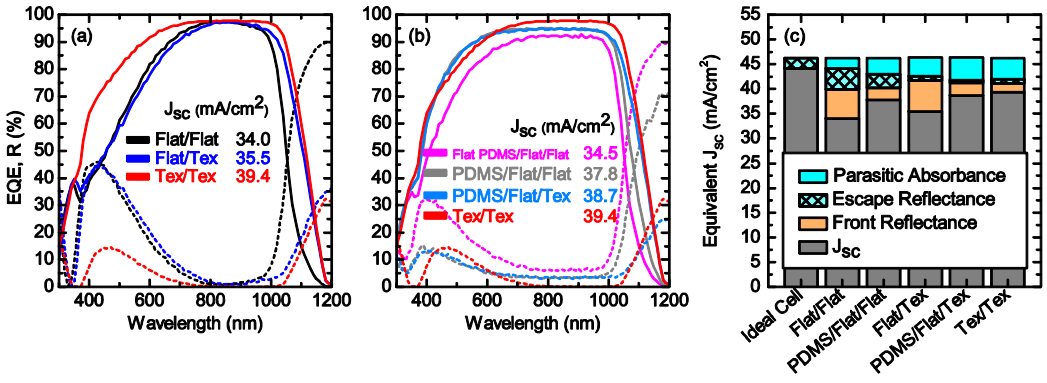

Figure 3-2. Simulated EQE (solid) and reflectance (R, dashed) spectra of devices (a) without PDMS layers and (b) with PDMS layers, and (c) comparison of the losses.

Figure 3-2c shows that Flat/Flat and Flat/Tex devices have, predictably, the same front-surface reflectance and thus their EQE curves nearly lie on top of each other in the 300–950 nm wavelength range (the range of wavelengths with absorption depth less than twice the wafer thickness). On the other hand, for longer wavelengths that interact with the rear surface, the EQE of the Flat/Tex device is higher because the textured rear surface scatters the light, elongating its path length and increasing absorbance. In addition to boosting J_{sc}, multiple internal reflections mean that long-wavelength light interacts more with the (absorbing) front ITO, rear ITO, and rear silver layers, resulting in slightly higher parasitic

absorption than in the Flat/Flat device. As expected, the Tex/Tex device has the highest J_{sc} of the three devices because the textured front surface effectively couples in the incident light, resulting in the smallest front-surface reflectance, and the textured front and rear surfaces together provide excellent light trapping [33, 34], as evident from the small summed parasitic absorbance and escape reflectance. Accordingly, the EQE of the Tex/Tex

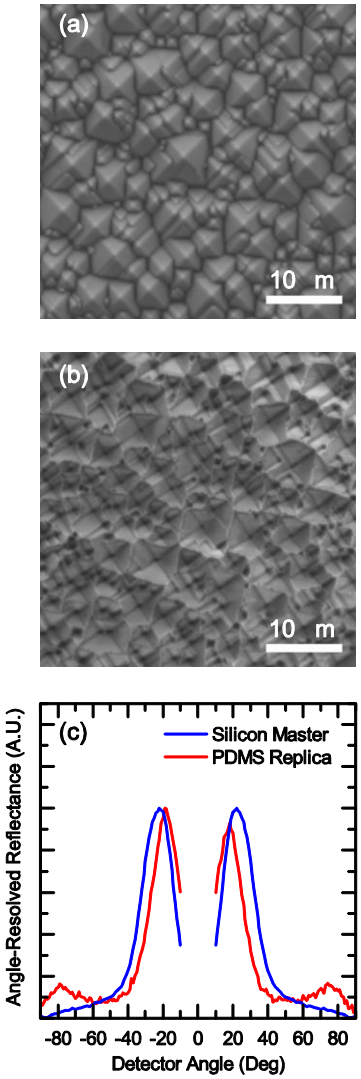

Figure 3-3. Measured EQE (solid) and reflectance (R, dashed) spectra of devices without and with PDMS layer and (a) without textured rear surfaces and (b) with textured rear surfaces. A double-side- textured device is shown as a reference in both cases.

device is much higher across all wavelengths than the devices with flat surfaces.

3.3.2 Measurements

Figure 3-3a shows a scanning electron microscopy (SEM) image of the textured silicon wafer that was used as the texture master, and Figure 3-3b shows an SEM image of the PDMS replica carrying the negative of this texture. To evaluate the fidelity of the replication process, we determined the base angles of the pyramids of the master and replica by measuring their angle-resolved reflectance spectra, displayed in Figure 3-3c. This measurement was performed with a wavelength of 270 nm because diffractive effects are negligible, as this wavelength is considerably smaller than the few-micrometer texture features [71]. However, at 270 nm, the total reflectance of the textured air/PDMS interface is approximately zero, unlike the total reflectance of 47% of the textured air/silicon interface. In order to measure its angle-resolved reflectance, the PDMS replica was thus coated with 30 nm of evaporated gold. The detector angles at which the peak reflectance occurs are 22° for the master and 18° for the replica, which translate into mode base angles of 50.5° and 49.5° [71]. Söderström previously reported that a silicon master with a mode base angle of 54° resulted in a PDMS replica with a base angle of only 49° [114]; we attribute the improved replication fidelity observed here to dilution of the PDMS (in toluene) to reduce its viscosity and to dipping the master in toluene to improve wetting of the PDMS to the mold surface.

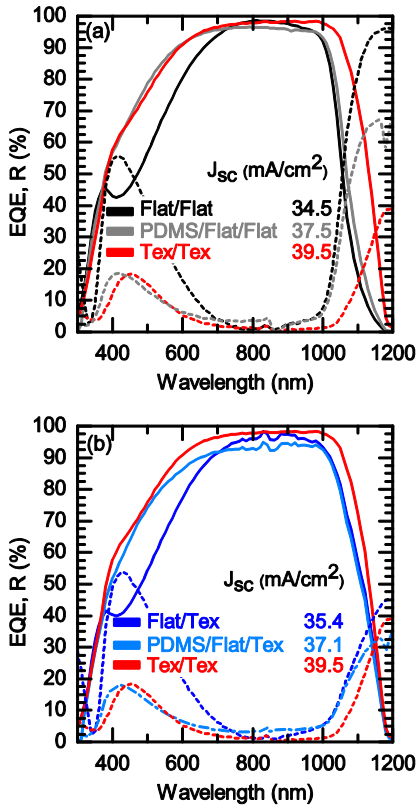

Figure 3-4. Measured EQE (solid) and reflectance (R, dashed) spectra of devices without and with PDMS layer and (a) without textured rear surfaces and (b) with textured rear surfaces. A double-side- textured device is shown as a reference in both cases.

The measured EQE and reflectance spectra for Flat/Flat and Flat/Tex devices with and without PDMS scattering layers are displayed in Figure 3-4. Figure 3-4a reveals that, with PDMS, the reflection loss of the Flat/Flat device reduces across all wavelengths except between 700 nm and 850 nm: The AM1.5G-weighted reflectance over the 300–1200 nm range is 7.1% (absolute) lower upon addition of PDMS, yielding 3 mA/cm^2 enhancement in J_{sc} and an EQE that matches the Tex/Tex device at short wavelengths. As predicted from simulations, PDMS benefits the infrared EQE only marginally because light is coupled out of the cells after only two passes at 6.7° relative to the wafer normal (instead of 0° without PDMS). Note that a silicon solar cell with only a textured front surface (Tex/Flat, not

investigated here) faces the same problem and is simulated to be only marginally better in the infrared than the PDMS/Flat/Flat cell (giving a J_{sc} gain 0.39 mA/cm^2). Figure 3-4b confirms the simulated results that a PDMS scattering layer added to the front of the Flat/Tex device reduces front-surface reflectance but not to the same degree as the Tex/Tex device over the 600–1000 nm wavelength range: The PDMS/Flat/Tex cell has an AM1.5G-weighted reflectance over the 300–1200 nm range of 6.4% (6.1% absolute lower than without PDMS), whereas that of the Tex/Tex device is 5.0%. The PDMS/Flat/Tex J_{sc} gain is 1.7 mA/cm^2, though this value is in fact lower than the expected gain because poor electrical contact of this cell during EQE measurement resulted in low EQE at all wavelengths (c.f. the PDMS/Flat/Flat device in Figure 3-4a, which has higher peak EQE and thus higher J_{sc}).

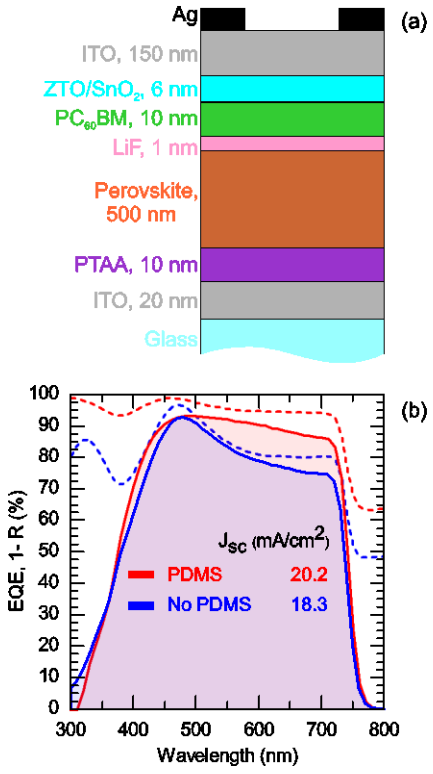

Figure 3-5. (a) Schematic of the planar perovskite solar cell, and (b) EQE (solid) and 1-reflectance (R, dashed) spectra of the cell without and with a PDMS layer.

While silicon solar cells serve as an illustrative platform for comparative investigation of scattering by PDMS layers, the layers are intended to be used at the front of cells that are challenging to texture. We thus demonstrate the efficacy of a PDMS layer by testing it on the perovskite solar cell illustrated in Figure 3-5a. As shown in Figure 3-5b, the primary source of optical loss in this device is reflection at the planar front surface. (Light trapping is much less important—note the steep rise in EQE at the bandgap wavelength caused by the absorber's direct bandgap.) After the PDMS layer is applied to the front surface, the reflection loss reduces by 3.4 mA/cm^2, which increases J_{sc} by 1.9 mA/cm^2. The remaining current is absorbed parasitically in the front contact of the cell, suggesting that, as with the silicon cells, the front ITO layer should be re-optimized specifically for use with PDMS layers. This cell has an open-circuit voltage (V_{oc}) of 1.10 V and a fill factor (FF) of 75%, and thus the cell efficiency jumps from 15.1% for without the scattering layer case to 16.7% with it—a 10.6% relative improvement.

3.4 Conclusion

Solar cells with planar surfaces and their tandems suffer from large optical losses due to high front-surface reflectance and, in some cases, poor trapping of weakly absorbed, long-wavelength light. This contribution has demonstrated that PDMS scattering layers applied to silicon devices with planar front surfaces successfully reduce front-surface reflectance and, when coupled with rear-surface textures, provide optical performance close to double-side-textured silicon solar cells. PDMS scattering layers can be attached to cells of any composition—we demonstrated current enhancement of a planar perovskite solar cell, and the layers are equally applicable to planar CdTe, GaAs, thin-film silicon,

and organic solar cells. In addition, the layers hold particular promise for tandem solar cells; for example, a PDMS layer can be used to both reduce front-surface reflectance and tune current matching in two-terminal, monolithic perovskite/silicon, perovskite/perovskite, and III-V/silicon tandems. Though we investigated only PDMS layers carrying a random inverted pyramid texture, any other texture may be implemented with equal facility provided that a master is available. Given the ease with which a PDMS layer can be (non-destructively) added to a completed solar cell, the layers serve as a convenient tool for testing current and efficiency limits with textures that are difficult to engineer into the cells themselves. Furthermore, the layers have a similar refractive index as the front glass used in solar modules, and thus approximate the performance of modules with textured glass. This is likely where the greatest value of the approach lies, as modules with textured glass are becoming more common in the market and PDMS layers allow module optical simulation with even small, research cells without encapsulation and lamination.

CHAPTER

4 OPTICAL MODELING OF WIDE-BANDGAP PEROVSKITE AND PEROVSKITE/SILICON TANDEM SOLAR CELLS USING COMPLEX REFRACTIVE INDICES FOR ARBITRARY-BANDGAP PEROVSKITE ABSORBER

4.1 Introduction

Perovskite solar cells have rapidly improved in the last few years, with the best power conversion efficiency reaching 23.3% [18]. Due to their superior optical properties (abrupt band edge, infrared transparency) and easy bandgap tunability [115, 116], perovskites are attractive candidates for top cells in tandem applications [12]. Perovskites also find use in other optoelectronic applications, such as light-emitting diodes (LED) [117-119], displays [120], and lasers [121, 122].

Perovskites with wide bandgaps are needed for the top cell in a tandem solar cell. A popular way to synthesize a wide-bandgap perovskite is by adjusting the iodide (I) to bromide (Br) ratio in methylammonium lead triiodide ($MAPb(Br_xI_{1-x})_3$) or in formamidinium (FA) lead triiodide ($FAPb(Br_xI_{1-x})_3$) perovskites. More recently it has been shown that adding cesium (Cs) to the latter, thus forming $Cs_yFA_{1-y}Pb(Br_xI_{1-x})_3$, reduces the Br required to achieve a given (wide) bandgap, and this leads to greater photostability [123, 124]. These 1.6 eV to 1.9 eV perovskites enable several kinds of tandem solar cells, including perovskite/perovskite, perovskite/CIGS and perovskite/silicon [19, 23, 125]. For example, perovskite/perovskite two- and four-terminal tandems with $FA_{0.85}Cs_{0.15}Pb(I_{0.3}Br_{0.7})_3$ or $FA_{0.83}Cs_{0.17}Pb(I_{0.83}Br_{0.17})_3$ as the wide-bandgap perovskite top cell achieved efficiencies of 18.1% and 20.1%, respectively [23, 24]. Similarly,

perovskite/CIGS tandems with $MAPb(Br_xI_{1-x})_3$ reached efficiencies of 10.9% and 23.9% in the two- and four-terminal configurations, respectively, and were limited by parasitic optical losses [125, 126]. Likewise, perovskite/silicon tandems with $Cs_{0.17}FA_{0.83}Pb(Br_{0.17}I_{0.83})_3$ hit 23.6% and 26% efficiencies in the two- and four-terminal configurations, respectively [19, 21].

Though a world-record device, the 23.6%-efficient perovskite/silicon tandem is still well below the 30% mark that is achievable with two junctions in a two-terminal device with silicon as a bottom cell [12]. In this champion device, the sum of the photo-generated current densities in both sub-cells is only 37 mA/cm^2—lower than that of a single-junction silicon cell—mainly due to reflection and parasitic absorption. To minimize such optical losses, and thus to improve the efficiency of the world-record perovskite/perovskite, perovskite/CIGS, and perovskite/silicon tandem, requires detailed and systematic optical modeling that identifies the optimum optical design. The first step in this analysis is to accurately determine the complex refractive indices (*n* and *k*)—frequently called the optical constants—of wide-bandgap perovskites. One recent study from Werner et al. reported optical constants for select perovskite compositions but did not verify if the constants could reproduce perovskite cell results when used in optical simulation [127]. It also did not indicate how the results could be made useful to researchers studying wide-bandgap perovskite materials with different compositions.

In this paper we report optical constants for $Cs_yFA_{1-y}Pb(Br_xI_{1-x})_3$ wide-bandgap perovskites that have shown promising optical, thermal, and environmental stability and are therefore more likely than other compositions to be used in tandem solar cells [128, 129]. $Cs_yFA_{1-y}Pb(Br_xI_{1-x})_3$ (CsBr) perovskites are often referred to by their Cs and Br

content: For example, $Cs_{0.4}FA_{0.6}Pb(Br_{0.3}I_{0.7})_3$ would be Cs40/Br30. We use multi-angle spectroscopic ellipsometry and spectrophotometry to uniquely determine the optical constants of two specific compositions of CsBr perovskite with bandgaps of approximately 1.63 (Cs17/Br17, the composition used in the world-record perovskite/silicon and perovskite/perovskite tandem) and 1.68 eV (Cs25/Br20) [19, 129]. These bandgaps are achieved by varying the Cs/FA ratio by changing the relative concentration of CsI to PbI_2, and by varying the Br/I ratio by changing the relative concentration of FAI to FABr in the precurser solution [19, 129]. We first verify our methodology on a more commonly used absorber, $CH_3NH_3PbI_3$ (MAPI), that has a bandgap of 1.57 eV and for which reference optical constants are available in the literature [130]. After applying the same methodology to the CsBr perovskites, we simulate the absorptance and reflectance of single-junction perovskite cells with the obtained refractive indices, and compare the results to the measured spectra. We then introduce a simple approach to obtain optical constants for any CsBr perovskite with a bandgap between 1.55 eV and 1.68 eV using the refractive indices of MAPI, and employ these to create a guide to maximize the current from perovskite/silicon tandem cells.

4.2 Experimental

Sample preparation: Semi-transparent perovskite devices were fabricated on patterned, 10 Ω/□ glass from Xin Yan Technology. Substrates were sonicated in Extran, acetone, and isopropanol, and UV-ozone cleaned for 10 minutes. Next, a 1M solution of nickel nitrate hexahydrate (Sigma-Aldrich, puriss) and ethylenediamine (Sigma-Aldrich) in anhydrous ethylene glycol (Sigma-Aldrich) was spun at 5000 rpm for 50 seconds and annealed at 300 °C for 1 hour onto the ITO substrates to form a nickel oxide (NiO_x) hole transport layer.

The NiO_x films were quickly taken into a dry air box for perovskite fabrication. The MAPI perovskite was deposited using a 1M solution in 9:1 v/v ratio of *N*,*N*-dimethylformamide (DMF, Sigma-Aldrich) and dimethyl sulfoxide (DMSO, Sigma-Aldrich) with a 1:1 ratio of PbI_2 (TCI) and methylammonium iodide (MAI, Dyesol). The solution was deposited through a 0.2 μm PTFE filter and spun at 1000 rpm for 10 seconds, followed by 6000 rpm for 10 seconds, and 1000 rpm for 5 seconds. Compressed dried air was blown directly onto the samples during the third spin step. The films were annealed on a hot plate at 60 °C for 5 seconds and then 100 °C for 30 minutes. This deposition method was adapted from Conings et al [131]. For the Cs17/Br17 and Cs25/Br20 perovskite compositions, a solution of PbI_2 (1.5M) and CsI (0.255M for Cs17/Br17 or 0.375M for Cs25/Br20, Sigma-Aldrich, 99.99% trace metals) was dissolved in the 9:1 DMF/DMSO and spun onto the NiO_x-coated substrates at 3000 rpm for 30 seconds. The PbI_2/CsI layer was annealed at 100 °C for 10 minutes. After cooling to room temperature, a 0.4M solution of formamidinium iodide (FAI, Dyesol) and formamidinum bromide (FABr, Dyesol) (39:61) for the Cs17/Br17 perovskite and 0.375M solution of FAI and FABr (2:8) for the Cs25/Br20 perovskite in anhydrous isopropanol (Sigma) was spun on top at 3000 rpm for 30 seconds and annealed at 150 °C for 1 hour. Next, we thermally evaporated 30 nm of C60, followed by 4 nm of stoichiometric SnO_2 with and 2 nm of zinc tin oxide pulsed-CVD at 100 °C, with full details of process parameters given previously [19]. Then, a 150-nm-thick layer of ITO was sputtered using a base pressure of $< 5\times10^{-6}$ Torr, deposition pressure of 2×10^{-3}, power density of 8 watts/inch^2, and oxygen partial pressure of 5%, as previously detailed in the supplemental section of Bush et al [128]. Silver fingers were thermally evaporated outside the device active area to carry current.

For ellipsometry characterization, single layers of MAPI, C_{60}, SnO_2, and front ITO were deposited onto Eagle glass separately, using the procedures described above. Similarly, single layers of Cs17/Br17 and Cs25/Br20 were deposited on quartz, and NiO_x was deposited onto SiO_2-coated single-side-polished silicon substrates to provide better refractive-index contrast between the film and substrate.

Sample characterization: The PL spectra of perovskite films (MAPI, Cs17/Br17, and Cs25/Br20) on glass or quartz substrates were measured on an in-house-built PL system. The PL was measured at room temperature using a 532 nm laser diode having 0.46 mW excitation power and a spot size of 0.54 mm. A photomultiplier tube (PMT) was used as the detector.

The perovskite films were characterized with spectroscopic ellipsometry using a J.A. Woollam M2000 or VASE instrument, and with spectrophotometry using a PerkinElmer Lambda 950 instrument. The ellipsometry spectra were measured in air at angles of incidence of 50–75° with a 5° step. The measurements were performed in reflectance mode from the film side in the wavelength range of 370–1690 nm for Cs17/Br17 and Cs25/Br20 samples, and 300–1700 nm for MAPI samples. The transmittance and reflectance spectra of the same samples were measured at normal and 7° incidence, respectively. Simultaneous fitting of the ellipsometry and spectrophotometry data was done with J.A. Woollam CompleteEASE software to arrive at optical constants.

The same methodology was used to determine the optical constants of the individual front ITO, rear ITO, SnO_2, C_{60}, and NiO_x layers, which were deposited on glass or silicon wafers coated with SiO_2. The front ITO, rear ITO, and SnO_2 layers were fit using combined Tauc-Lorentz and Drude models, C_{60} was fit with three Tauc-Lorentz oscillators, NiO_x was

fit with a single Tauc-Lorentz oscillator, and glass and SiO_2 were fit with Cauchy models. The surface roughness of the layers was modeled using the Bruggeman effective medium approximation with 50% air and 50% of the layer being fit. Fig. B1–B7 (Appendix:B) show the ellipsometry and spectrophotometery fits, as well as the extracted optical constants, for each layer.

Scanning electron microscope (SEM) images of perovskite films were collected with a Zeiss Auriga FIB-SEM. The same instrument was used to mill into the perovskite devices and collect cross-sectional images to determine the thicknesses of the perovskite, front ITO, and rear ITO layers. Atomic force microscopy (AFM) was used to analyze the surface topography of perovskite films. Mapping was performed in air with a silicon pyramidal tip in tapping mode using a Bruker Multimode instrument.

EQE and reflectance measurements of solar cells were performed using a PV Measurements QEX10 tool and a PerkinElmer Lambda 950 spectrophotometer, respectively, both in the wavelength range of 300–1200 nm with a 10 nm step. In these measurements, a detached silver

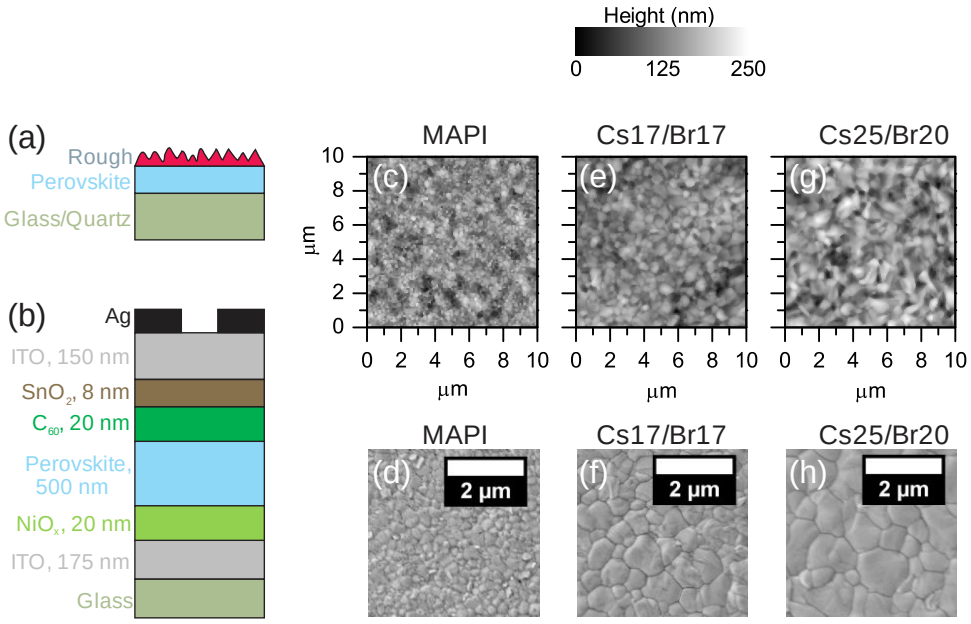

Figure 4-1. (a) Optical model used in fitting ellipsometry spectra of perovskite films on glass or quartz. (b) Schematic of single-junction semi-transparent perovskite cells used to validate optical modeling. AFM (c, e, and g) and SEM (d, f, and h) images of perovskite films for which ellipsometry, transmittance, and reflectance spectra were collected to determine optical constants.

reflector was placed behind the cells so as to have a known material to simulate and not, e.g., a stainless steel measurement chuck.

Optical simulations: Optical simulations of single-junction perovskite solar cells were carried out with the SunSolve software from PV Lighthouse. SunSolve combines thin-film optics with Monte-Carlo-based ray-tracing. Simulations were performed assuming planar interfaces, with the cell structure shown in Figure 4-1(b). The thicknesses of the front and rear ITO layers were determined by ellipsometry fitting as well as verified with cross-sectional imaging of the cell using SEM. The perovskite absorber thickness was approximated from cross-sectional imaging of the device with SEM but was still allowed to vary within 10% range of that thickness value, as the films were observed in SEM to have some spatial thickness variation. The cross-sectional images of the devices are shown

in Figure B-9 (Appendix:B) and the thicknesses are given in Table B-2. The thicknesses of the thinner films in the stack—SnO_2, C_{60}, and NiO_x—were not easily measured with SEM and were thus treated as free fitting parameters with starting guesses equal to the target thicknesses shown in Figure 4-1(b). The final thicknesses of all layers that were used in the optical simulations are given in Table B-3 (Appendix:B). A detached silver reflector was included behind the cell during the simulations, as was present in the measurements. The reported simulated EQE spectra are the absorptance in the perovskite layers, which is equivalent to assuming 100% carrier collection efficiency—a reasonable assumption for these thin, long-carrier-lifetime absorbers.

Optical simulations of perovskite/silicon tandem solar cells were also simulated in SunSolve following the same procedure, but varying the thickness and complex refractive index of the perovskite layer between 1.55 and 1.68 eV using Eq. (1). The optical constants and thicknesses of all other layers were held constant, and the optical constants for MgF_2, intrinsic and doped (n- and p-type) amorphous silicon (a-Si:H), crystalline silicon, silver, the intermediate ITO layer, and the rear ITO layer were taken from the literature [105, 112, 132, 133]. Table B-4 (Appendix:B) shows the thickness of each layer in the tandem simulations. The upright random pyramids on the front and rear of the silicon wafers were modeled with a base angle 51.5°, and all other layers were treated as being conformal to this texture. This base angle and SunSolve's ray tracing algorithm captures the light trapping actually observed in a textured silicon wafer, as described by Baker-Finch et al., as opposed to artificially increasing the bottom cell thickness to mimic the effects of scattering [65, 134, 135].

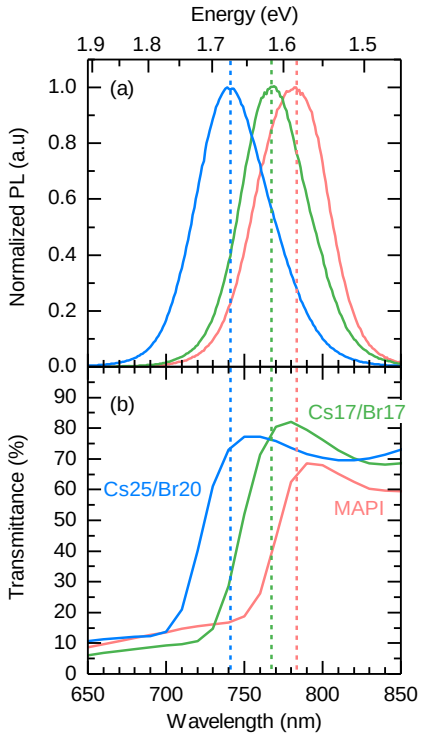

Figure 4-2. Photoluminescence (a) and transmittance (b) of MAPI, Cs17/Br17, Cs25/Br20 perovskite films on glass.

4.3 Results and Discussion

MAPI, Cs17/Br17, and Cs25/Br20 perovskite films were deposited on glass or quartz substrates (sample structure shown in Figure 4-1(a)) and complementary semi-transparent perovskite solar cells were prepared in the cell structure shown in Figure 4-1(b). The surfaces of the films appear in the atomic force microscopy (AFM) and scanning electron microscopy (SEM) images in Figure 4-1(c)-(h), and reveal that they are conformal with no pinholes. The films do, however, have appreciable surface roughness and thickness non-uniformity despite considerable effort to make them smooth. The root-mean-squared surface roughnesses determined from 10 μm^2 AFM images are 25 nm, 26 nm, and 34 nm for MAPI, Cs17/Br17, and Cs25/Br20, respectively. These roughness values are at the

boundary of spectral range that could be modeled with effective medium theories generally employed in ellipsometry fitting [136-138]. Greater surface roughness leads to depolarization and scattering of reflected light, especially at shorter wavelengths making modeling challenging [139].

Figure 4-2 shows the measured photoluminescence (PL) of these perovskite films along with their near-bandgap transmittance. As expected from their compositions, each sample has a distinct bandgap, with the PL peaks at approximately 1.58, 1.61, and 1.67 eV for MAPI, Cs17/Br17, and Cs25/Br20, respectively.

Importantly, the PL spectra of Cs17/Br17 and Cs25/Br20 showed no sign of photo-induced halide segregation (i.e., the Hoke effect), thus confirming their photostabilty during the measurements [129]. The PL spectra were not used directly when determining optical constants, but provide a reference for the bandgap values found from ellipsometry.

For each of the three perovskite films, ellipsometry spectra were collected at three angles of incidence and coupled with transmittance and reflectance spectra for fitting. Figure 4-3 shows the spectra—and their fits—for MAPI, which we investigate first as a model system suitable for validating our methodology. The data were fit in the Woollam CompleteEASE software program assuming a surface roughness layer with thickness, a bulk perovskite layer with thickness, and a substrate (glass or quartz), as shown in Figure 4-1(a). The surface roughness layer was modeled as an effective medium using a Bruggeman effective medium approximation with 50% air and 50% perovskite film having

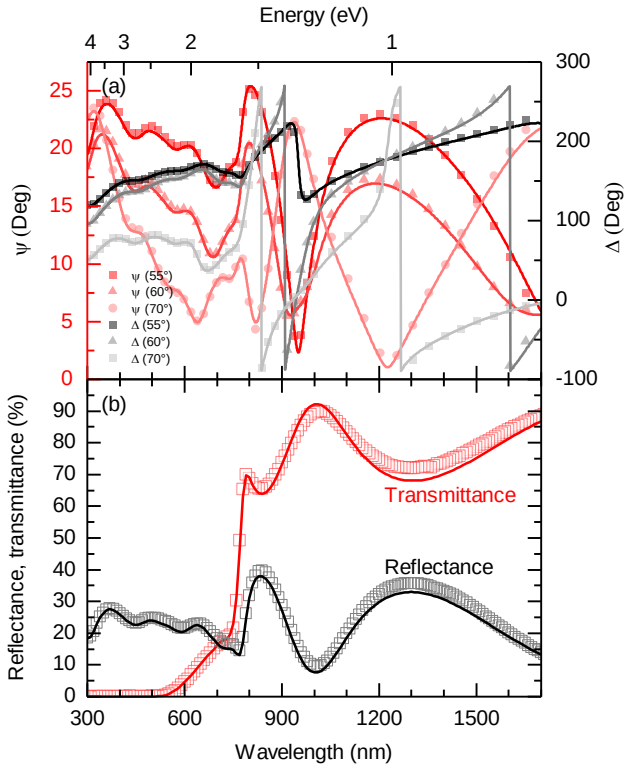

Figure 4-3. Simulated (line) and measured (symbol) (a) multi-angle spectroscopic ellipsometry spectra and (b) reflectance and transmittance spectra of a MAPI film on glass.

the same refractive index as the underlying bulk perovskite layer [140]. The substrate was modeled with a Cauchy dispersion relation fit to spectra recorded on bare substrates.

The bulk perovskite layer was first modeled with a version of a basis spline (B-spline) that is Kramers–Kronig consistent [141]. The flexibility of B-spline curves allows one to capture all of the essential details of the dielectric function of the films, such as very low absorption at energies just below the bandgap energy, and the curves also smoothly connect the transparent IR region to the absorbing visible region. An additional benefit of using a B-spline is that no prior knowledge of the dielectric function of the material is required, unlike when using oscillators, for which one has to know the energies at which to place them.

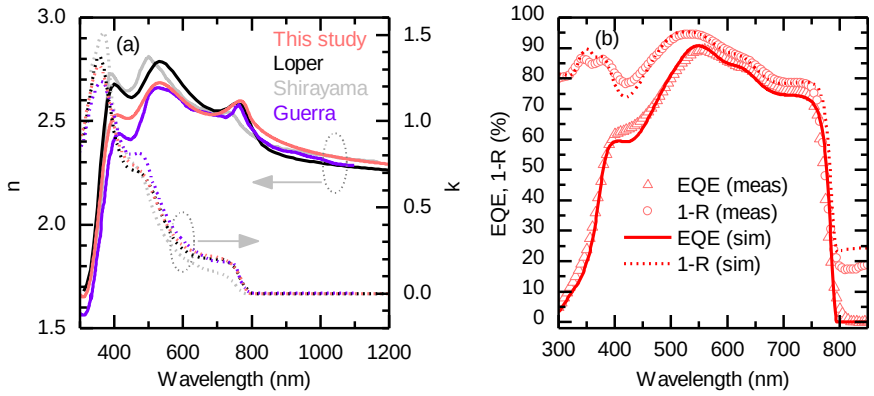

Figure 4-4. (a) Comparison of determined MAPI optical constants with those available in the literature [22, 38, 39]. (b) Simulated (line) and measured (symbol) total absorptance (1-R) and EQE of MAPI cell with a detached silver reflector.

To reduce the number of fitting parameters and to arrive at a physics-based oscillator model of the dielectric function, the B-spline-fit refractive index was next parameterized using a general oscillator approach with multiple Tauc–Lorentz (TL) oscillators [142, 143]. These oscillators were placed at the energies of the peaks that appeared in the B-spline. In particular, we used three TL oscillators in the energy range of 0.73–4.13 eV for MAPI and of 0.73–3.35 eV for Cs17/Br17 and Cs25/Br20. We choose the TL model because it is Kramers–Kronig consistent and can account for the nanocrystalline nature of the films [143]. Figure 5-3 shows that the final fit is in excellent agreement with the measured data, with a root-mean-squared error (MSE) of 9.39.

Figure 4-4(a) shows the optical constants for the MAPI film determined using the procedure outlined above, and Table B-1 in the Appendix:B lists the parameters of the three oscillators comprising the dielectric function. For comparison, Figure 4-4(a) also shows the optical constants determined by others, which—especially those from Loper et al.—are widely used by the research community [130, 143, 144]. Throughout the investigated region, the maximum difference between our refractive index (*n*) and that

determined by Loper et al. is only 0.18. At 480–700 nm wavelengths, our *n* matches more closely with that of Guerra et al [144]. Variations between the *n* values reported by different groups could be due to differences in measurement or fit methods, the films themselves, or both. For example, Guerra et al. reported lower *n* upon degradation due to air exposure. In contrast, there is no significant difference between our extinction coefficient (*k*) and that reported by Loper et al. The oscillator positions—1.57, 2.50 and 3.33 eV—and the bandgap of 1.56 eV are also very similar to those reported by Loper et al [130].

To further validate the accuracy of the optical constants of MAPI shown in Figure 4-4(a), we simulated a complete single-junction semi-transparent MAPI cell. The optical constants of the contact and electrode layers were determined with a similar methodology to that used for the perovskite layer. Figure 4-4(b) shows the simulated and measured external quantum efficiency (EQE) and total absorptance (1-reflectance) spectra with a detached rear reflector. The measured short-circuit current density (J_{sc}) obtained by integrating the product of the EQE and the AM1.5G spectral irradiance over the wavelengths of 300─800 nm for this MAPI cell is 19.70 mA/cm^2 while the simulated J_{sc} is 19.55 mA/cm^2. For the same wavelength range, the measured reflectance loss is 5.44 mA/cm^2 and the simulated loss is 5.25 mA/cm^2. The maximum absolute difference between the measured and simulated EQE and reflectance is 5% and 4.4%, respectively.

Two apparent sources of error in the simulated spectra are surface roughness—revealed in Figure 4-1—and bandtail states. Surface roughness was neglected during the simulation by assuming planar layers, which results in overemphasized interference fringes—see, for example, the local extrema near 450 and 550 nm. (Others have introduced models to account for surface roughness, but they add considerable complexity and uncertainty [145-

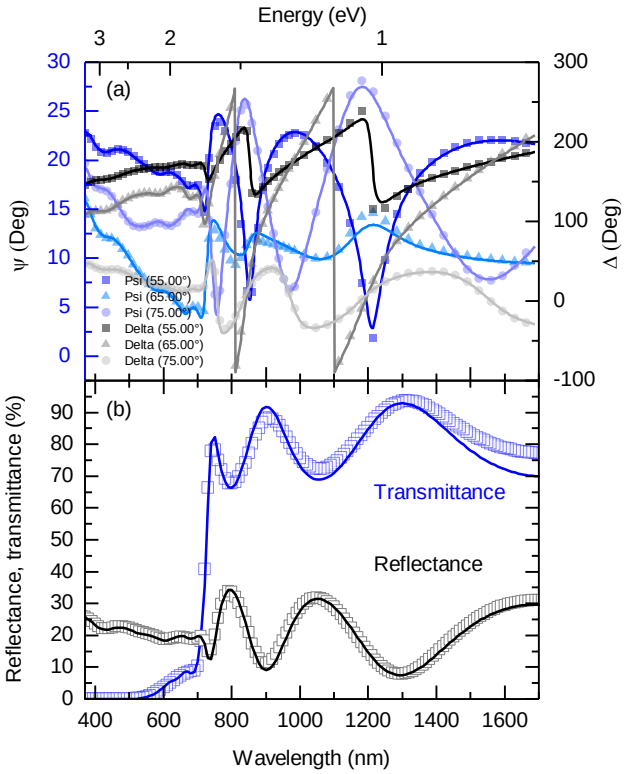

Figure 4-5. Simulated (line) and measured (symbol) (a) multi-angle spectroscopic ellipsometry spectra and (b) reflectance and transmittance spectra of a Cs25/Br20 film on quartz.

147].) States near the band edges are responsible for absorption that is not successfully reproduced in the simulated EQE when using the MAPI optical constants parameterized with three TL oscillators. This absorption just below the bandgap can be better fitted with the optical constants generated by the original B-spline fit, for which *k* remains greater than zero just beyond 800 nm, as shown in Figure B-10(a) in the Appendix:B. Alternatively, a fourth TL oscillator can be added to capture this sub-bandgap absorption, as was done by Shirayama et al., but we prefer to limit the number of oscillators to three to avoid excessive fit parameters [143]. Moreover, the impact of this slight misfit on the device optical modeling is negligible in terms of J_{sc}.

Having validated our approach to determine accurate optical constants using MAPI, we now apply the same methodology to the wide-bandgap CsBr perovskites. The TL model fit to the multi-angle ellipsometry, reflectance, and transmittance spectra of the Cs25/Br20 perovskite in Figure 4-5 results in an MSE value of 11.83. That is, the fit to the ellipsometry and spectrophotometry data is excellent throughout the measured spectral range—particularly in the critical above-bandgap-energy region—except in the transparent region (>1000 nm) for the transmittance. The fit was obtained with three TL oscillators, and their parameters (bandgap, amplitude, breadth, energy) are given in Table B-1 in the Appendix:B. A similarly excellent fit was obtained for the Cs17/Br17 perovskite—shown in Figure B-8 with oscillator values in Table B-1 in the Appendix:B—with an MSE value of 11.51. In relation to MAPI, the oscillator positions for Cs17/Br17 and Cs25/Br20 are blue-shifted, with the highest shift occurring for the bandgap oscillator and modest shifts occurring for the oscillators at higher energies. This contrasts with the uniform shift of all oscillators postulated by Hörantner et al. and others [135, 148, 149]. Though there is no experimental evidence yet available, these oscillators may represent the same electronic transitions that are observed in MAPI. The optical constants obtained with the TL fits for

Cs25/Br20, Cs17/Br17, and MAPI are shown in Figure 4-6. The corresponding optical constants obtained directly from the B-spline fits are shown in Figure B-10(a) in the Appendix:B, and the dielectric functions corresponding to the refractive indices in Figure 5-6 appear in Figure B-10(b) in the Appendix:B. Note that the abrupt change in *k* between 700 and 800 nm indicates that the two wide-bandgap perovskite compositions that we study have sharper band edges than the compositions investigated by Werner et al. [127], which will lead to different absorber layer thicknesses required to current match in a two-terminal tandem.

Figure 4-7 compares the measured EQE and total absorptance of Cs25/Br20 and Cs17/Br17 perovskite solar cells with detached silver reflectors to those simulated with the optical constants in Figure 4-6. The measured J_{sc} and reflectance loss for the Cs25/Br20 cell within the spectral range of 300─760 nm are 17.20 and 4.90 mA/cm^2, respectively, while the simulated values are 17.33 and 4.85 mA/cm^2—less than 0.1 mA/cm^2 difference.

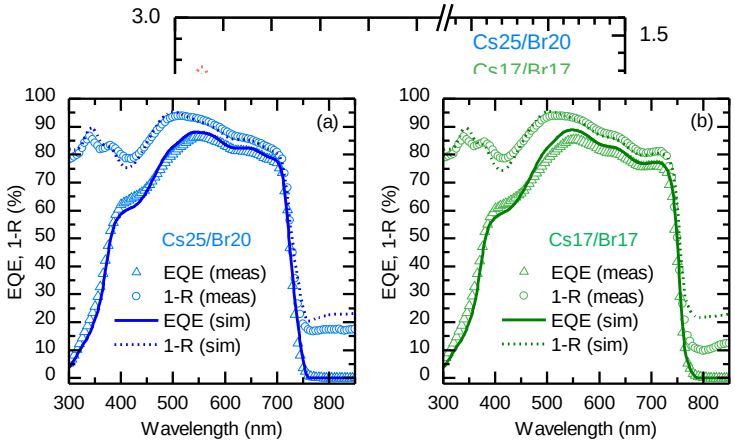

Figure 4-7. Simulated (line) and measured (symbol) total absorptance (1-R) and EQE of (a) Cs25/Br20 and (b) Cs17/Br17 cells with detached silver reflectors.

the result of the TL oscillators placed within the measured spectral range.

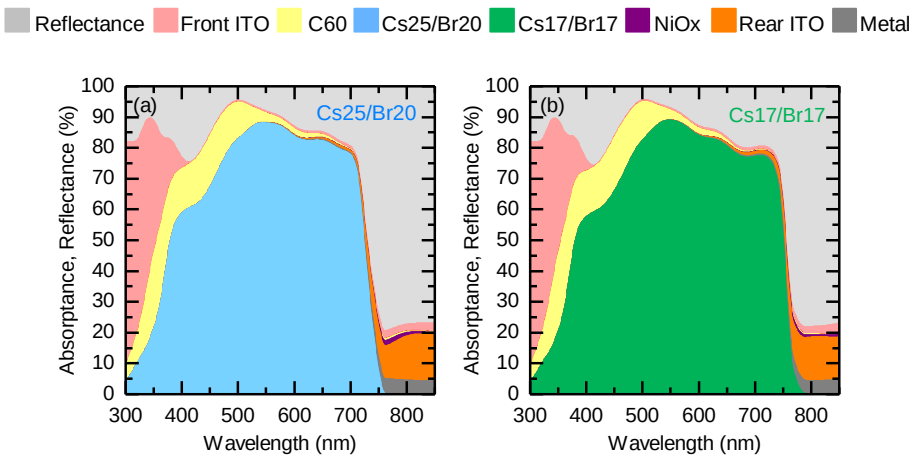

Figure 4-8. Breakdown of optical losses in the (a) Cs25/Br20 and (b) Cs17/Br17 cells.

The discrepancy is slightly larger for the Cs17/Br17 cell: The measured J_{sc} of 18.02 mA/cm^2 and reflectance loss of 6.48 mA/cm^2 within 300─790 nm spectral range differ by nearly 0.3 mA/cm^2 from than the simulated values of 18.31 mA/cm^2 and 6.21 mA/cm^2, respectively. We attribute the mismatch, and in particular the low simulated reflectance at sub-bandgap wavelengths, to a difference in the optical constants of the simulated and actual rear ITO films, as the latter was not available for ellipsometry. We tried to simulate Cs17/Br17 cell using a lower-carrier-density rear ITO layer than used in current simulation and it yields a good fit.

In simulating all three perovskite devices, we found that front-surface reflection at super-bandgap wavelengths is the biggest loss due to the planar cell structure, accounting for 3.62 and 3.93 mA/cm^2 of the total reflectance values reported above for the Cs25/Br20 and Cs17/Br17 devices, respectively. Note that all of this loss could be captured by the cell if front-surface reflection was eliminated by, e.g., texturing and anti-reflection coatings [150], unlike the near- and sub-bandgap "escape" reflection that is present with a detached rear reflector and that would be measured as transmitted light without one [27]. As shown

in the current-loss breakdowns in Figure 4-8, the next largest losses are parasitic absorption in the C_{60} electron contact and front ITO, which are responsible for 1.41 and 0.66 mA/cm^2, respectively, for the Cs25/Br20 cell, and 1.48 and 0.65 mA/cm^2, respectively, for the Cs17/Br17 cell. The parasitic absorption loss in the C_{60} layer could be reduced by thinning it (it is presently >20 nm) without incurring significant detrimental electrical loss, as demonstrated by Liu et al [151].

While the wide-bandgap perovskite optical constants determined here are sufficiently accurate to determine current losses and thus guide cell development, the processes of obtaining and verifying them for new absorbers is somewhat cumbersome. Figure 4-6 reveals that widening the bandgap of CsBr perovskites mostly just blue-shifts their optical constants—this appears to be particularly true for the extinction coefficient. We thus explore the possibility of translating the complex refractive index of MAPI to simulate perovskite cells with arbitrary (wide) bandgaps, using the now known refractive indices of Cs25/Br20 and Cs17/Br17 for validation. Eq. (1) translates each *n* and *k* pairing to a new position on the wavelength axis:

$$\lambda_{new} = \lambda - \left(\Delta\lambda_{bandgap} + 10\right) \times \left(\frac{\lambda}{1200}\right) \qquad 300\ nm \leq \lambda \leq 1200\ nm \qquad (1)$$

Here, $\Delta\lambda_{bandgap}$ is the difference in bandgap between MAPI and the desired wide-bandgap material expressed as a wavelength in nanometers, 10 is an empirically determined offset that correctly aligns the translated and reference indices in the bandgap region, and the multiplier is a stretch factor that shifts *n* and *k* near the bandgap more than at shorter wavelengths. The somewhat arbitrarily chosen 1200 nm wavelength in the stretch factor means that the optical constants are overly stretched at longer wavelengths, but this has

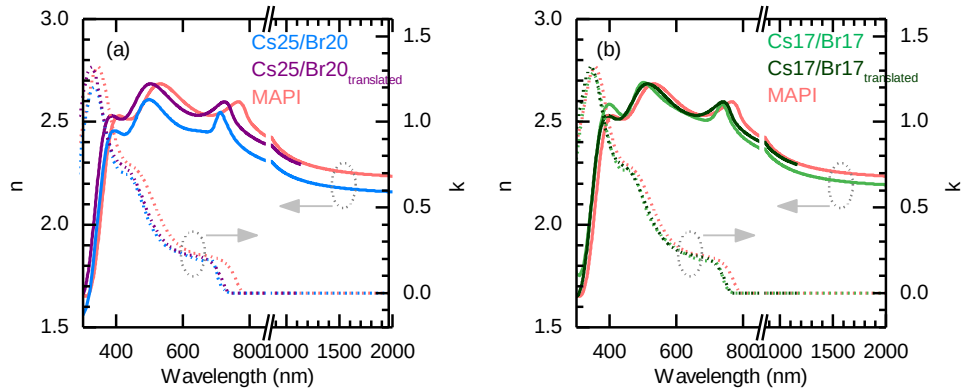

Figure 4-9. Optical constants obtained for (a) Cs25/Br20 and (b) Cs17/Br17 perovskites by translating the MAPI complex refractive index according to Eq. (1).

little consequence because $k = 0$ and n is relatively constant in the infrared region. Figure 4-9 shows that Eq. (1) reproduces the extinction coefficients of Cs25/Br20 and Cs17/Br17 with good accuracy, though an additional term that steepens k at the band edge with increasing bandgap would further enhance its fidelity. Eq. (1) also yields the correct n peak positions, but has a near-constant offset of approximately 0.1 for the Cs25/Br20 perovskite. Using these perovskite translated optical constants, we simulated the EQE and total absorptance of the Cs25/Br20 and Cs17/Br17 cells keeping the thicknesses and refractive indices of all other layers as before. The results, in Figure B-11 (Appendix:B), agree well with the measured spectra, indicating that Eq. (1) is useful for bandgaps of at least up to 1.67 eV.

To date, the best two-terminal perovskite/silicon solar cells have been realized by an iterative process in which the thickness of a particular perovskite layer is adjusted in tandem cells—perhaps guided by optical simulations of that particular perovskite, like those in this contribution—until an experimental maximum matched current is reached [19, 152]. The ability to simulate perovskite cells with arbitrary bandgap, however, enables *simultaneous* optimization of the perovskite bandgap and thickness. Figure 4-10(b) is an

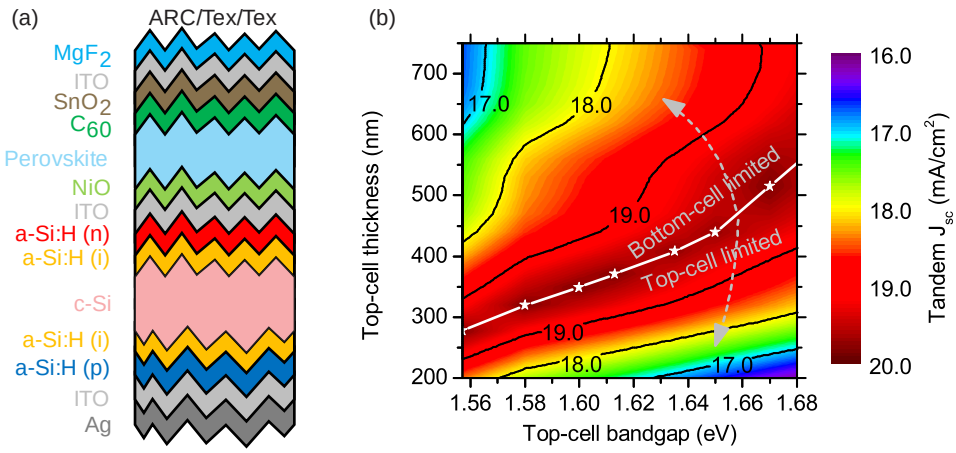

Figure 4-10. (a) Schematic of the two-terminal perovskite/silicon tandem solar cell used in optical modeling, and (b) corresponding simulated tandem Jsc for variable top-cell bandgap and thickness.

example of this for the both-sides-textured tandem cell structure depicted in Figure 4-10(a). The color contours show the J_{sc} in the current-limiting sub-cell, and the white line denotes the current-matched condition. For the particular contact and electrode layers considered here (Table B-4, Appendix:B), the highest current-matched J_{sc} is 19.8 mA/cm^2, which is well over 1 mA/cm^2 higher than that of the present record cell thanks in large part to the textured front surface of the silicon cell [19]. As expected, the perovskite thickness required to current match increases as its bandgap is widened since more infrared light reaches the bottom cell. Also noteworthy, Figure 4-10(b) reveals that a previously unreported advantage of a double-side-textured wafer is that the tandem J_{sc} is relatively insensitive to slight changes in the perovskite thickness—much less so than for a tandem with a planar front surface—which is helpful for cell fabricators because most perovskite layers to date have non-negligible local thickness variation. Assuming a V_{oc} of 0.701 V for the silicon bottom cell as estimated by Yu et al., a V_{oc} of 1.070 V for the top cell as reported by Bush et al., and a fill-factor of 79% as achieved in the current-world record tandem, yields an

expected maximum efficiency of 27.7% for a perovskite bandgap of 1.68 eV and thickness of 550 nm [129, 153].

4.4 Conclusion

We have used ellipsometry and spectrophotometry to uniquely determine the optical constants for two wide-bandgap perovskite compositions that are not available in the literature and that are important for tandem solar cells. When used in optical simulations, these optical constants match the measured quantum efficiency and reflectance spectra of the corresponding single-junction semi-transparent perovskite cells, which provides a pathway to minimizing current losses in these devices. Furthermore, the same measured spectra can be reproduced with nearly the same accuracy using optical constants generated by translating those of the popular MAPI perovskite along the wavelength axis, providing a quick and useful tool for optical simulation of wide-bandgap perovskites with arbitrary bandgap. This, in turn, enables the short-circuit current density of tandems to be calculated for a perovskite of any given bandgap or thickness, and we showed a path to 19.8 mA/cm^2 matched current density in a perovskite/silicon tandem solar cell with a double-side-textured silicon wafer and a wide range of perovskite bandgaps. This corresponds to a top- and bottom-cell summed current density that rivals that of the best single-junction silicon solar cells, and this value can be further improved by reducing parasitic absorption in the contact and electrode layers. Moreover, with an accurate model or data illuminating how the open-circuit voltage and fill factor of CsBr perovskite solar cells vary as a function of their bandgap, it will be possible to render Figure 5-10 as an efficiency map—instead of a current density map—that provides valuable guidance in top-cell optimization.

CHAPTER

5 EFFICIENCY POTENTIAL OF PEROVSKITE/PEROVSKITE TANDEM SOLAR CELLS BASED ON PRESENT ABSORBERS

5.1 Introduction

Power conversion efficiency (PCE) of single-junction perovskite solar cells has sky-rocketed from a mere 3.8% to 25.2% in just a decade [18]. However, like other single-junction technologies (crystalline silicon (Si), cadmium telluride (CdTe) and copper indium gallium selenide (CIGS)) perovskite PCE is also limited to Shockley-Quiesser (SQ) limit (~33%) and practical-limit would be even lower than that [9, 154]. In addition, now that area-dependent balance-of-system cost takes the major share of the installed photovoltaic (PV) system cost, it is imperative to experiment with technologies with potential for PCEs higher than SQ-limit. For this tandem solar cells with two junctions are a promising way to surpass the SQ-limit, with projected PCEs >40% [10, 13, 155, 156]. Therefore, perovskite/perovskite tandems are a natural next step in the evolution of perovskite solar cell technology. Properties such as, easy bandgap tunability, sharp absorption edge, low-defect density, low-temperature and solution processability and high absorption coefficient make perovskites ideal for tandem development [157]. Techno-economic analysis also supports that perovskite/perovskite tandems could provide efficiencies as high as III-V and Si-based tandems but at a cost of thin-film solar cell manufacturing, thus greatly reducing the $/W metric [158-161].

Perovskites have a general crystal structure of ABX_3 and by substituting different elements at A, B and X site, wide- and narrow-bandgap perovskites with bandgaps in 1.18–2.3 eV range could be fabricated [11]. Combining wide- and narrow-bandgap perovskites,

two-terminal (2T) perovskite/perovskite tandems with PCEs in the range of ~18%–24.8% have been demonstrated [24-26, 162]. However, these values are lower than the best single-junction perovskite (25.2%) [18]. Besides open-circuit voltage (V_{oc}) and fill-factor (*FF*) being sub-optimal in these tandems, the short-circuit current density (J_{sc}) is also the limiting factor. These 2T perovskite/perovskite tandems typically employ 1.2–1.25 eV narrow-bandgap perovskite as a bottom-cell which should

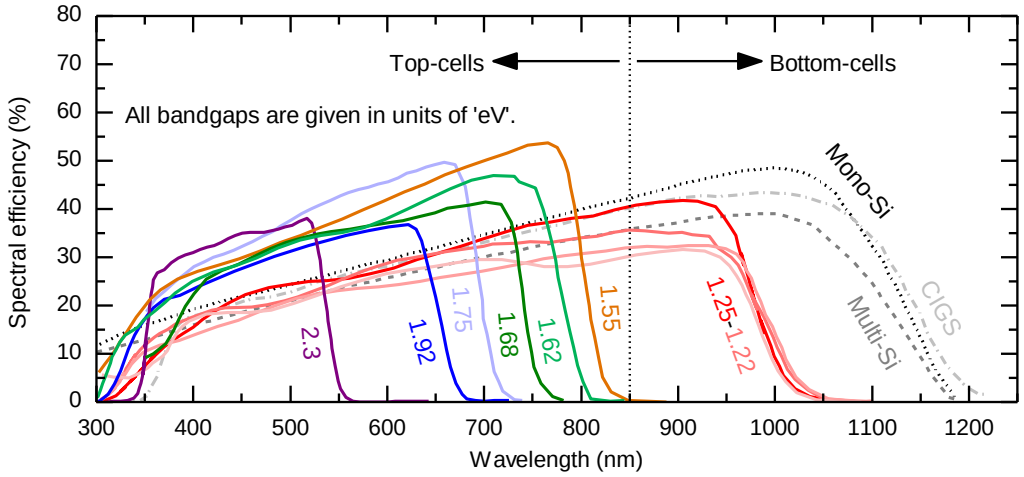

Figure 5-1. Spectral efficiency of various perovskite top-cells and bottom-cells showing their potential for pairing in tandems. Among bottom-cells shown is the performance comparison of narrow-bandgap perovskites with record mono- and multi-crystalline Si and CIGS cells. Reported efficiencies have been taken from [5, 6, 26, 129, 162-170].

allow combined tandem J_{sc} of ~40 mA/cm^2. However, top J_{sc}s are only ~30 mA/cm^2 with the world-record device producing 32 mA/cm^2 [23, 25, 26, 168]. Major reason for this are the material and fabrication constraints related to narrow-bandgap perovskites leading to optical losses. First constraint is that narrow-bandgap perovskites have short carrier recombination lifetimes and small mobility of electron, thus limiting the thickness of absorber. This leads to low external quantum efficiency (EQE) values around the band edge, thus prompting the need for thicker absorber (>1 µm). Second constraint is that the

lowest bandgaps for narrow-bandgap perovskites with PCE >17% lie in the range of 1.2–1.25 eV range. However, ideal bottom-cell should have a bandgap of 1–1.1 eV to limit the transmission loss. These shortcomings are evident in Figure 5-1 that shows the spectral efficiency plots of various wide- and narrow-bandgap perovskites and other bottom-cells. It reveals that wide-bandgap perovskites of different bandgaps are superior at converting <700 nm wavelength light and thus are great top-cell partners. In contrast, narrow-bandgap perovskites perform poor in the relevant wavelength range of 700–1000 nm and as well as in comparison to other bottom-cells.

Other reason of optical loss in 2T perovskite/perovskite tandems is the sub-optimal light-management due to the complexity of device design. Such as high reflectance loss caused by planar structure and multi-layer thin-films, light-trapping loss due to absence of texture and parasitic losses in transparent electrodes, charge selective and passivating contacts. These optical challenges are common to all 2T perovskite/perovskite tandems demonstrated to-date, resulting in tandem J_{sc}s less than 15 mA/cm^2. In order to facilitate further development of perovskite/perovskite tandems it is important to establish their efficiency potential from optical standpoint. Previous efforts to ascertain their PCE limit have considered detailed-balance approach assuming abrupt bandgaps, used optical properties of the absorbers which were not verified against cell results or have not taken parasitic absorptance and device design into consideration [11, 149]. Furthermore, no alternative light-management designs have been studied to improve the tandem performance.

Therefore, in this work we establish the efficiency potential of 2T perovskite/perovskite tandems using the validated optical properties of present best-in-class absorbers employed

in experimentally demonstrated 23% efficient 2T perovskite/perovskite tandem [171]. With this we provide optical constants for 1.22 eV narrow-bandgap perovskite, not available before. The composition chosen is $Cs_{0.05}FA_{0.5}MA_{0.45}(Pb_{0.5}Sn_{0.5})I_3$ (Cs5/MA45/Sn50), as it has long carrier liftetimes >1 µs, allowing thicker absorber (>1 µm) to be made which is an essential requirement for high J_{sc} and has been used as a bottom-cell in the said 23% efficient 2T perovskite/perovskite tandem [171]. We characterize its complex refractive indices using spectroscopic ellipsometry (SE) and spectrophotometry. And validate them by matching optically simulated EQE and reflectance to measured results of complementary Cs5/MA45/Sn50 single-junction cell. We further validate these optical constants against measured results of 23% efficient 2T perovskite/perovskite tandem. For this we also characterize $Cs_{0.4}FA_{0.6}Pb(I_{0.65}Br_{0.35})_3$ (Cs40/Br35), 1.8 eV wide-bandgap perovskite that was employed as top-cell in 23% efficient tandem using SE and then simulate an entire tandem stack for validation. Next, we perform simulation of 2T perovskite/perovskite tandem by varying top (Cs40/Br35)- and bottom (Cs5/MA45/Sn50)-cell thicknesses and also for variable top-cell bandgap from 1.56–1.9 eV with Cs5/MA45/Sn50 (1.22 eV) as a bottom-cell in different, practically relevant, light-management schemes reporting their efficiency potential along with assessment of losses and opportunities to serve as a guide for further development from current 23% to PCEs up to 29%.

5.2 Ellipsometry Fitting and Optical Simulations

Cs5/MA45/Sn50 and Cs40/Br35 perovskite films were deposited on glass substrate to be analyzed with SE. Figure C-1 shows the SEM image of the surface of these films which reveals the films are compact, uniform and without voids or pinholes. These properties are

essential for the collection of artifact-free SE spectra. Figure C-2 shows the AFM images of the surface of these films. It reveals 26.2 nm and 28.3 nm of root-mean square surface roughness for Cs5/MA45/Sn50 and Cs40/Br35 respectively. Large film roughness has been shown to yield non-zero absorbing behavior below the bandgap and results in an overall overestimation of the absorption coefficient curve [136, 143].

For both perovskite-on-glass samples we measured reflectance and transmittance along with SE spectra at five different angles of incidence. Since SE spectra were collected in reflectance mode, thus addition of transmittance helps in accurate determination of extinction coefficient of the film, especially the small values around the band edge. The optical model used to represent these samples during the fitting procedure is roughness layer/bulk perovskite film/glass substrate. In this the roughness layer is modeled with Bruggeman effective medium approximation as having 50% air and 50% underlying

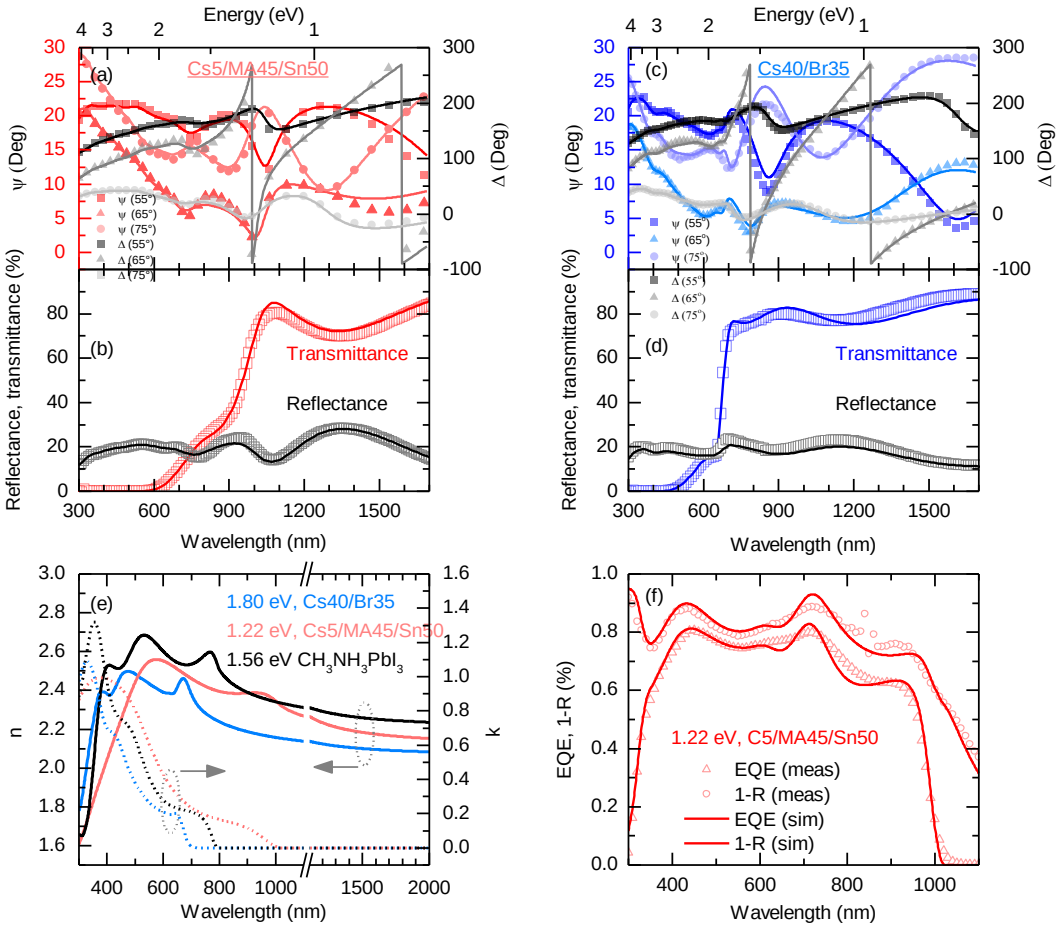

Figure 5-2. Measured SE and spectrophotometric spectra along with fits are shown for narrow-bandgap (a, b) and wide-bandgap (c, d) perovskites respectively. Resulting refractive indices are shown in (e). Match between measured and simulated EQE and 1-reflectance curves obtained with refractive indices in (e) for Cs5/MA45/Sn50 narrow-bandgap single-junction perovskite are shown in (f).

perovskite volume fractions [140]. This is justified since the features in roughness layer are less than ~$\lambda/10$ for the spectral range considered here [136, 172]. Lastly, glass substrate is modeled using Cauchy dispersion formula as it has negligible absorptance in the relevant spectral range [173].

SE and spectrophotometric spectra are initially fitted with Basis splines (B-spline) which are flexible polynomial functions capable of fitting dielectric function of any shape

in a continuous and smooth manner [141]. The reason for choosing B-spline as a starting point is that there is no prior credible information available about the absorption features present in the dielectric function of these novel absorbers and especially of narrow-bandgap perovskites. We use the Kramers-Kronig consistent version of B-spline that yields physically realistic optical constants. First, the SE and spectrophotometric spectra are fitted in the transparent spectral range (>1100 nm) to determine the thickness of the film which is kept fixed for subsequent steps. Next, fitting is extended to entire spectral range and roughness layer is added to the fitting procedure in the last step. After this the best-fit B-Spline obtained dielectric function is parametrized with physics-based multiple Tauc-Lorentz (TL) oscillators [142]. Measured spectra and the result of TL-fitting is shown in Figure 6-2a-b and 6-2c-d for Cs5/MA45/Sn50 and Cs40/Br35 perovskite films respectively. These fits have a root-mean-squared-error (MSE) of 10.2 and 11.4 for Cs5/MA45/Sn50 and Cs40/Br35 respectively. We associate slight mismatch between measured and modeled spectra in Figure 5-2a-d to SE and spectrophotometric measurements being carried out at different spots on the sample. Modeled refractive indices are shown in Figure 5-2e which reveals important differences. First around the respective bandgap regions the slope of extinction coefficient curve is steeper for wide-bandgap Cs40/Br35 while the slope is much more gradual for narrow-bandgap Cs5/MA45/Sn50. This potentially explains why a much thicker narrow-bandgap perovskite is needed to current-match to a much thinner wide-bandgap perovskite in a 2T perovskite/perovskite tandem. Second difference between the two set of complex refractive indices is the number of peaks where Cs40/Br35 has 3 peaks while Cs5/MA45/Sn50 has only 2 peaks. The number of these peaks are often associated with band-to-band optical transitions, the origin

of which has been explained by Shirayama *et al.*, for $CH_3NH_3PbI_3$ (refractive indices shown in Figure 5-2e) and the same explanation could be extended to Cs40/Br35 [143]. But there is no information available to the best of our knowledge that explains the absorption features of mixed Sn-Pb perovskites like Cs5/MA45/Sn50.

Next we validate the optical constants obtained for Cs5/MA45/Sn50, by reproducing the measured EQE and reflectance of single-junction Cs5/MA45/Sn50-cell through optical simulation. This and all subsequent optical simulations were performed using SunSolve which combines thin-film optics with ray-tracing [109]. Complete details of the optical setup are given in the Supplementary Material. We fabricate Cs5/MA45/Sn50 cell with the following structure (from sunward side): glass/ITO/(PEDOT:PSS)/Perovskite/C_{60}/BCP/Cu, where ITO is indium-tin-oxide, PEDOT:PSS is poly(3,4-ethylenedioxythiophene) polystyrene sulfonate, C_{60} is fullerene,

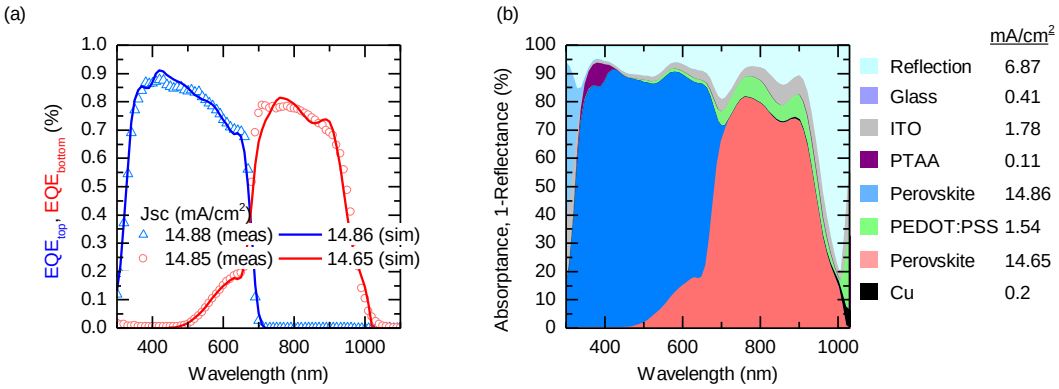

Figure 5-3. Comparison of measured EQE of Cs40/Br35-wide- and Cs5/MA45/Sn50-narrow-bandgap perovskite in tandem to simulated results (a). Reflectance and optical losses in various layers of the tandem are plotted in (b).

BCP is 2,9-dimethyl-4,7-diphenyl-1,10-phenanthroline and Cu is copper. The cell structure is shown in Figure C-3 (Appendix C). Refractive indices for passivating layer, front

transparent conducting oxide, rear metal, electron and hole selective layers were characterized with SE and are shown in Figure C-7 (Appendix C). Final thicknesses of all the layers used in the simulation are given in Table C-2 (Appendix C). The comparison of simulated and measured results is shown in Figure 5-2f. Excellent match is obtained between measured and simulated results, though simulated results show interference fringes which are absent in the measured cell results due to the presence of roughness. Measured J_{sc} obtained by integrating the product of EQE and AM1.5G solar spectrum over the wavelength range of 300–1050 nm is 26.0 mA/cm^2 while the simulated J_{sc} is 26.7 mA/cm^2, representing a relative mismatch of 2.7%. Similar calculation for reflectance shows, the difference in measured and simulated curve is only 0.01% absolute, with measured value being 8.57 mA/cm^2.

Tandem device result matching and losses

Now we simulate experimentally demonstrated 23% efficient 2T perovskite/perovskite tandem based on 1.22 eV-Cs5/MA45/Sn50, bottom-cell and 1.8 eV-Cs40/Br35, top-cell to validate that the results match the measured tandem EQEs before proposing improvements and new light-management designs [174]. This would further establish the reliability of refractive indices of Cs5/MA45/Sn50 and Cs40/Br35 perovskite obtained earlier. In this tandem, top- and bottom-cell employed Poly [bis (4-phenyl)(2,4,6-trimethylphenyl)amine] (PTAA) and PEDOT:PSS/PTAA as a hole contact respectively, and C_{60}/tin-oxide (SnO_2) and C_{60}/BCP as an electron contact respectively, while ITO was used as inter-connecting layer. ITO is also used as front contact and Cu as rear contact. Figure 6-4a shows the

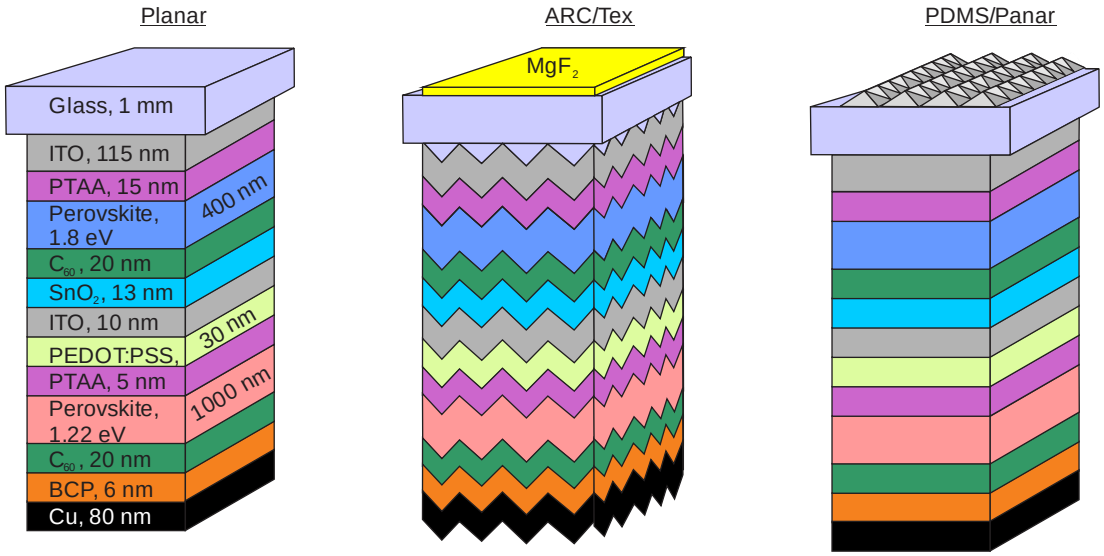

Figure 5-4. Schematic showing 2T perovskite/perovskite tandem configurations investigated. (a) *Planar*, (b) *ARC/Tex*, (c) *PDMS/Planar*.

schematic of tandem device structure along with the nominal thicknesses of all the layers. While the actual thicknesses used in the simulation are shown in Table C-3 (Appendix C). Figure 5-3a shows the comparison of measured and simulated EQE of top (Cs40/Br35)- and bottom (Cs5/MA45/Sn50)-cell. Excellent match is achieved, with measured J_{sc} for wide- and narrow-bandgap perovskite being 14.88 and 14.85 mA/cm^2, versus simulated J_{sc} of 14.86 and 14.65 mA/cm^2 respectively.

We further investigate reflectance and optical losses in various layers of the tandem which are shown in Figure 5-3b. Losses are numerically calculated by integrating the product of absorptance in the layer and AM1.5G solar spectrum for the wavelength range of 300–1050 nm. Three biggest sources of loss are front surface reflectance and parasitic absorptance in front ITO and in PEDOT:PSS hole contact, equivalent to 6.87, 1.78, 1.54 mA/cm^2 respectively. Planar front surface of the glass contributes the most to high reflectance loss across all wavelengths with limited bottom-cell thickness being

responsible for escape of longer wavelengths (>950 nm). Whereas parasitic absorptance in the front ITO below 400 nm wavelength exclusively lowers the top-cell J_{sc} and above 700 nm only the bottom-cell. On the other hand parasitic absorptance in PEDOT:PSS primarily takes away J_{sc} from bottom-cell due to its location in the stack and also due to its high extinction coefficient beyond the wavelength of 600 nm. These loss numbers point to the potential increase in tandem J_{sc} by about 5 mA/cm^2 that could be achieved by reducing reflectance, by thinning and using more transparent front ITO and lastly by using hole contacts such as, NiO_x that incur less parasitic absorptance.

Based on simulation results above perovskite/perovskite tandems are limited in performance in terms of J_{sc} due to sub-optimal device design and material and fabrication constraints, such as non-optimized thicknesses of absorbers and parasitic absorptance in support layers. Another limiting factor could be non-ideal bandgap combination for top- and bottom-cell perovskites. Therefore, next we investigate and optimize these aspects for the 2T perovskite/perovskite tandems shown in Figure 5-4 to provide a guideline for further development.

5.3 Efficiency Potential with Different Tandem Device Designs

It is crucial to have thick narrow-bandgap perovskite bottom-cell in 2T perovskite/perovskite tandems to reach high current-matched J_{sc}. But an alternative way to improve J_{sc} is by elongating the light path through the absorber by changing the device design and by incorporating effective antireflection methods. Here we investigate two new device designs which could potentially boost the J_{sc} and thus the efficiency of tandems. We also compare their performance to *Planar* tandem design employed universally in perovskite tandem community shown in Figure 5-4a and simulated earlier. First alternative

design is shown in Figure 5-4b which is inspired by work done in thin-film solar cells where front glass has a textured surface on the inside and all other layers are deposited conformally on it [175-177]. This helps in scattering the incoming light and elongating the light path through the absorber. Perovskite deposition on textured surface has already been demonstrated using evaporation method for perovskite/Si tandem [28]. Therefore, this design is practically relevant and realizable. We have also added a magnesium fluoride (MgF_2) antireflection coating (ARC) on the front of the glass to maximize the transmission of light. This design is referred to as *ARC/Tex*. Second design is inspired by work done in perovskite/Si tandem community where textured polymeric anti-reflection foil has been used as a substitute for textured glass, to suppress the front surface reflectance leading to efficiencies greater than 25% [20, 178, 179]. In our case we assume the anti-reflection foil is made of polydimethysiloxane (PDMS) and carries random pyramids as texture which are copied from alkaline etched Si. This approach has been shown to be very effective at reducing reflectance [150]. Moreover, in contrast to *ARC/Tex*, the major advantage of *PDMS/Planar* design is that it doesn't require conformal deposition of layers on textured surface. The schematic of this design is shown in Figure 5-4c and is referred to as *PDMS/Planar*.

Finally we simulate these three tandem device designs to investigate the J_{sc} attainable as top (Cs40/Br35)- and bottom (Cs5/MA45/Sn50)-cell thickness is varied. Performance enhancement versus absorber thickness is valuable to know since 2T perovskite/perovskite tandem are J_{sc} limited due to thin narrow-bandgap perovskite. Therefore, we varied the bottom-cell thickness from 300–1480 nm, which includes the thickness range (>1000 nm) not yet realized thus providing a target and potential gain. Top-cell thickness was varied

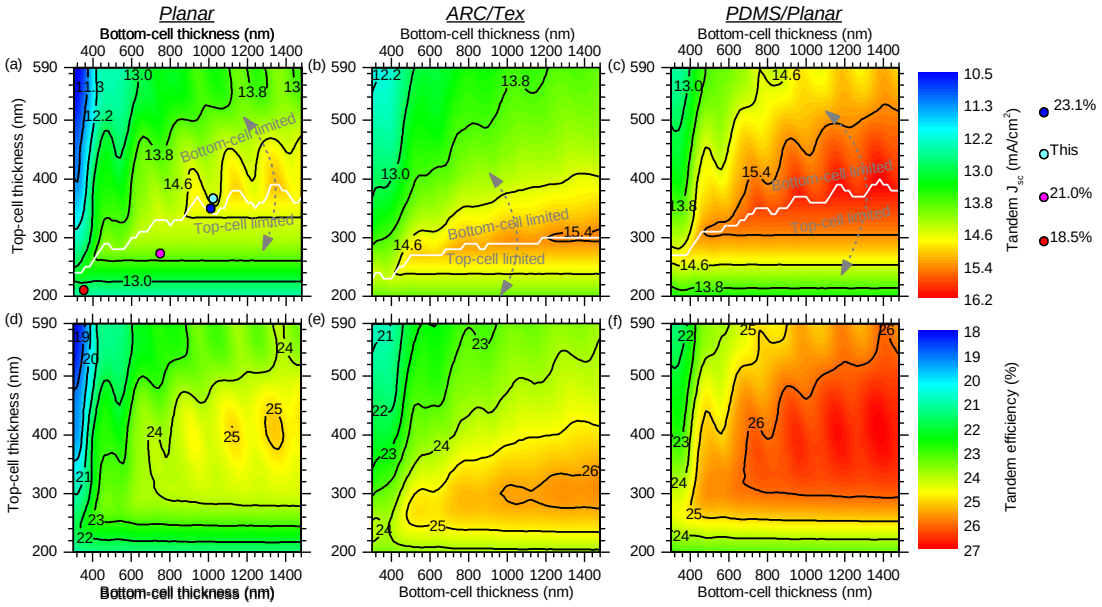

Figure 5-5. Simulation results of absorber thickness sweep showing tandem J_{sc} (a,b,c) and corresponding PCE (d,e,f) for *Planar*, *ARC/Tex* and *PDMS/Planar* configurations respectively. Also shown are the J_{sc}s of current highest efficiency 2T perovskite/perovskite tandems.

between 200–590 nm, a range found sufficient to reach current-matched condition. Layer thicknesses used in the simulation are given in Table C-3 (Appendix C). Results for top- and bottom-cell thickness sweep for *Planar*, *ARC/TEX* and *PDMS/Planar* configurations are shown in Figure 5-5. It can be seen from Figure 6-5a-c that for all configurations higher J_{sc} values are achieved for thicker narrow-bandgap perovskite. At the same time the respective region of higher J_{sc}s starts at lower bottom-cell thickness as the device design is changed from *Planar* to *ARC/TEX* and then to *PDMS/Planar*. Moreover, the region of higher J_{sc}s becomes broader as the device design is varied with the range of narrow-bandgap thickness required to achieve >14.6 mA/cm^2 being 900–1480, 500–1480 and 300–1480 nm for *Planar*, *ARC/TEX* and *PDMS/Planar* respectively. These observations imply, firstly high tandem J_{sc} can be achieved at lower narrow-bandgap thicknesses (<950 nm),

secondly tandem J_{sc} becomes less sensitive to variation in narrow-bandgap thickness with improved tandem design and lastly, thinner narrow-bandgap absorber means it would have higher quality (V_{oc}) due to low non-radiative recombination. Specifically, highest J_{sc}s for *Planar*, *ARC/TEX*, *PDMS/Planar* configurations are 15.1, 15.5 and 16.2 mA/cm^2 respectively. On the other hand, wide-bandgap perovskite thickness required for current-matching is between 250–500 nm and films of such thicknesses are routinely prepared with excellent quality [129, 180]. Reasons for observed benefits versus narrow-bandgap perovskite thickness and device design variation are that increasing narrow-bandgap thickness allows matching at higher J_{sc} since bottom-cell produces more photocurrent. While changing to *ARC/TEX* helps elongating the light path through tandem and its MgF_2 ARC improves transmission but since it is interference based thus its efficacy is thickness dependent. On the other hand *PDMS/Planar* performs the best because it improves transmission of light for all thicknesses of tandem equally and also mildly elongates the light path. For comparison we have also indicated the performance of some of the high performing 2T perovskite/perovskite tandems demonstrated thus far on Figure 6-5a. This clearly shows tandems would benefit from improved device design.

Corresponding to the J_{sc} plots in Figure 5-5a-c, we have calculated their PCEs shown in Figure 6-5d-f using 2-diode model explained in the Supplementary Material. For PCE calculation top- and bottom-cells are assumed to be operating at 75% of their detailed-balance PCE-limit. This is a conservative estimate since recent results have shown tandems operating at 80% of detailed-balance V_{oc} limit [25]. Results in Figure 5-5d-f show that PCEs closely follow the tandem J_{sc} trends which is expected since the bandgaps of wide- and narrow-bandgap sub-cells are unchanged and thickness variation does not drastically

change the V_{oc} and *FF* in the model considered here. We observe that PCE as high as 25% could be achieved for *Planar* configuration but requires narrow-bandgap perovskite thickness >1000 nm and wide-bandgap perovskite between 350–450 nm thick. This defines a narrow region to achieve 25% PCE, however 24% could be achieved for much greater range of thicknesses. In comparison present world-record 2T perovskite/perovskite tandem has a PCE of 24.8% and next best is at 23.1%, both of which have *Planar* structure. In contrast, simulations performed by Hörantner *et al.*, show that PCE of 31.9% and J_{sc} of 17.2 mA/cm^2 could be achieved with *Planar* tandem, however, they optimized the thicknesses of all the layers of tandem stack to reduce reflectance and parasitic absorptance which we have not performed [149]. Also the sensitivity of their result is not shown and in addition unlike our simulation they included MgF_2 ARC on the front glass. Results for *ARC/Tex* design shown in Figure 6-5e reveal PCE of 25% could be achieved between wide- and narrow-bandgap thicknesses of 250–400nm and 500–1480 nm respectively, while 26% PCE is also possible for a thicker bottom-cell, i.e. >1000 nm. Lastly, with *PDMS/Planar* configuration PCEs as high as 27% are possible with 25% and 26% achievable for broad narrow-bandgap thickness range of 400–1480 nm and 700–1480 nm respectively. This shows that with improved tandem design the constraint to have thick (>1000 nm) narrow-bandgap perovskite in a tandem could be mitigated while maintaining PCEs significantly higher than presently achieved.

Beside thicknesses of the absorbers other crucial design parameters for 2T tandems include the top-cell bandgap and its thickness. So next we investigate the impact of varying top-cell bandgap versus its thickness on the performance of 2T perovskite/perovskite

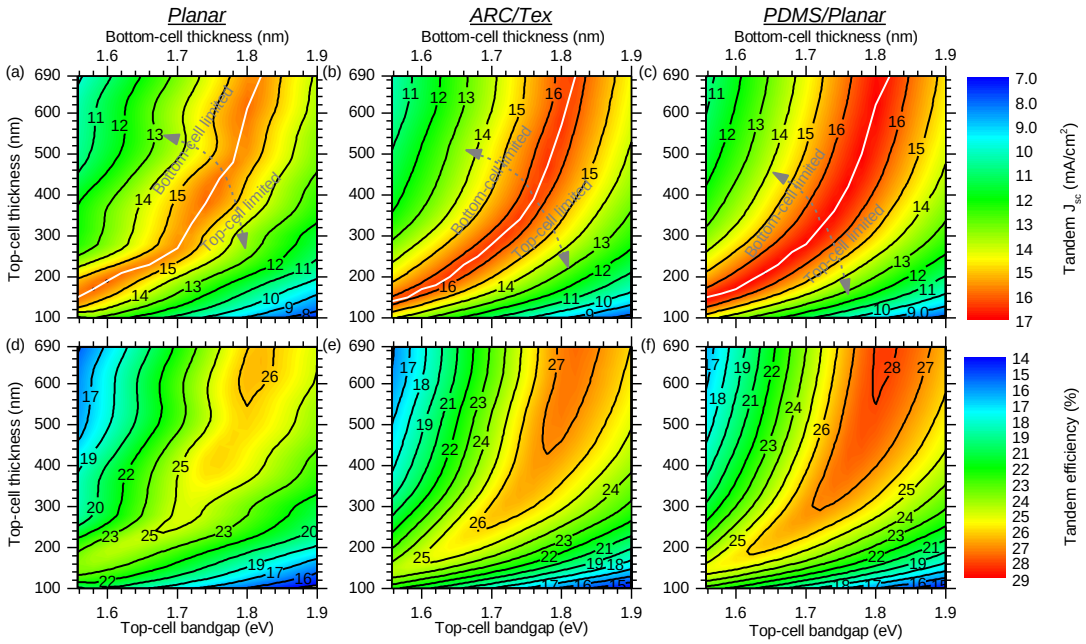

Figure 5-6. Simulation results of top-cell bandgap versus top-cell thickness variation showing tandem J_{sc} (a,b,c) and corresponding PCE (d,e,f) for *Planar*, *ARC/Tex* and *PDMS/Planar* configurations respectively. Bottom-cell is 1.22 eV Cs5/MA45/Sn50 perovskite with 1500 nm thickness.

tandem while keeping the same 1.22 eV Cs5/MA45/Sn50 bottom-cell. In these simulations bottom-cell thickness is kept constant at 1500 nm. We chose this value of thickness to allow maximum absorption in the bottom-cell so tandem J_{sc} could be matched at higher value. We have also reduced the thickness of front ITO and PEDOT:PSS to 60 and 20 nm respectively to reduce the parasitic absorptance. All other layer thicknesses are the same as used for simulation in Figure 5-3 and given in Table C-3 (Appendix C). Top-cell bandgap was varied between 1.56–1.9 eV and top-cell thickness from 100–690 nm. Simulated tandem J_{sc}s are shown in Figure 5-6a-c for *Planar*, *ARC/Tex* and *PDMS/Planar* configurations. For a given configuration, same value of maximum current-matched J_{sc} is reached for top-cell bandgaps <1.82 eV with its value increasing from 15.7 to 16.5 and then to 17 mA/cm^2 as tandem design is changed from *Planar* to *ARC/Tex* and

PDMS/Planar respectively. Beyond the bandgap of 1.82 eV it is not possible to reach current-matched condition for top-cell thicknesses considered here. This behavior has been observed for perovskite/Si tandems as well, which means higher bandgap top-cells would yield higher efficiency by contributing towards higher tandem V_{oc} until they start to limit the tandem J_{sc} [148, 181]. Moreover, tandem J_{sc} becomes less sensitive to variation in top-cell thickness with increasing top-cell bandgap for each respective configuration, with the least sensitivity for *PDMS/Planar* and highest for *Planar*. Corresponding PCE plots calculated using the 2-diode model as explained in Supplementary Material, are shown in Figure 5-6d-f. The results follow similar trend as tandem J_{sc}s, with PCEs increasing with increasing top-cell bandgap until it becomes current-limiting. Highest PCE for *Planar, ARC/Tex and PDMS/Planar* configuration is achieved for 1.82 eV top-cell bandgap and is 26.7%, 28.0% and 28.9% respectively, with V_{oc} of 1.91 V and *FF* of 0.89 for all three. Interestingly a tandem V_{oc} of 1.98 V has been achieved already which shows that our simulations are conservative estimate of the performance of 2T perovskite/perovskite tandems. The main hindering block is the *FF* with the highest demonstrated value of 0.81 [25, 26]. However, we also note it is not easy to achieve high performing 1.82 eV top-cell due to halide segregation.

5.4 Conclusion

Here we have demonstrated that perovskite/perovskite tandems could achieve efficiencies as high as perovskite/Si tandems. We did so by accurately simulating the EQE of 2T perovskite/perovskite tandem with demonstrated efficiency of 23%. For this we experimentally measured the refractive indices of its constituent best-in-class wide- and narrow-bandgap perovskite absorbers using SE and spectrophotometry. Later we provided

a guideline for further development by varying top- and bottom-cell thicknesses and top-cell bandgaps for currently planar designed tandems and for two new light-management designs. Specific outcomes are:

1. With *PDMS/Planar* and *ARC/Tex* architectures it is possible to achieve efficiencies as high as *Planar* perovskite/perovskite tandem but at much lower narrow-bandgap perovskite thicknesses and wide-bandgap perovskite bandgaps.
2. To achieve efficiencies comparable to perovskite/Si tandems (~30%) it is necessary to develop high-efficiency wide-bandgap perovskites with bandgaps between 1.8–1.82 eV and narrow-bandgap perovskites with thicknesses >1000 nm.
3. It is necessary to develop strategies to reduce front-surface reflectance and use alternative contact and electrode materials to reduce parasitic absorptance to achieve higher J_{sc}.

CHAPTER

6 SPECTROSCOPIC ELLIPSOMETRY OF WIDE-BANDGAP CdTe MATERIALS

6.1 Introduction

Polycrystalline (poly) CdTe leads the PV industry after silicon in terms of the market share. A highest PCE of 21% has been demonstrated with single-junction poly-CdTe by First Solar [6]. Major advantage of poly-CdTe is its cheap manufacturing due to low-cost of deposition methods involved. On the other hand silicon solar cells though are more efficient (26.7%) but also have high production cost associated with them. Combining these two technologies to form a II-VI/silicon tandem solar cell could provide a path to higher efficiency than either of the two without increasing the cost too much [182, 183]. Modeling has shown that ideal top-cell bandgap is around 1.7 eV to match with silicon bottom cell [12]. Therefore, CdTe whose natural bandgap is around ~1.48 eV must be raised to 1.7 eV, and this could be achieved by alloying with zinc (Zn) to form $Cd_xZn_{1-x}Te$ [17]. There has been demonstrations of 15.5–16.5% efficient single crystal CdZnTe solar cells. Our partners at Colorado State University (Carey Reich) are making these new alloys but with poly-CdSeTe material where Se is selenium. The success of II-VI/silicon tandem would depend on the optical properties of these top-cell materials. Spectroscopic ellipsometry (SE) has previously been applied to study poly-CdTe and CdSeTe for their properties such as defect density, strain, voids, bandgap and grain size [184, 185]. Therefore, in this work we use SE to determine the optical properties of poly-$Cd_xZn_{1-x}SeTe$. Changing the ratio of Zn in the films changes its bandgap [17]. Therefore it is important to determine the exact optical properties of these absorbers against the variable composition and preparation conditions.

6.2 Experimental Methods

CdZnSeTe samples were deposited on Pilkington TEC10 (soda-lime glass with a sodium (Na) diffusion barrier and a transparent conducting oxide (TCO) on one side) substrates with a 100 nm $Mg_{0.23}Zn_{0.77}O$ (MZO) layer coating the TCO side of the glass. This structure was preheated to 480°C before being transferred into the sublimation source by use of a magnetic transfer arm. The specialized sublimation source used (see Figure 6-1) is composed of two sub-sources physically stacked and thermally insulated from each other allowing independent temperature control for each source. The top source of this stack has through-holes to allow the vapor generated in the bottom source into the pocket under the substrate where the vapors mix and allow deposition of complex alloys. In this case, the top source contained $CdSe_{0.05}Te_{0.95}$ and the bottom source contained Zn. For the Zn containing alloy, the CdSeTe source was maintained at 575°C, the Zn source temperature was swept from 263°C to 335°C and the substrate heater used to maintain the substrate temperature during deposition was held at 400°C. The chamber was kept at pressure of 40 mTorr with deposition performed in argon (Ar) ambient.

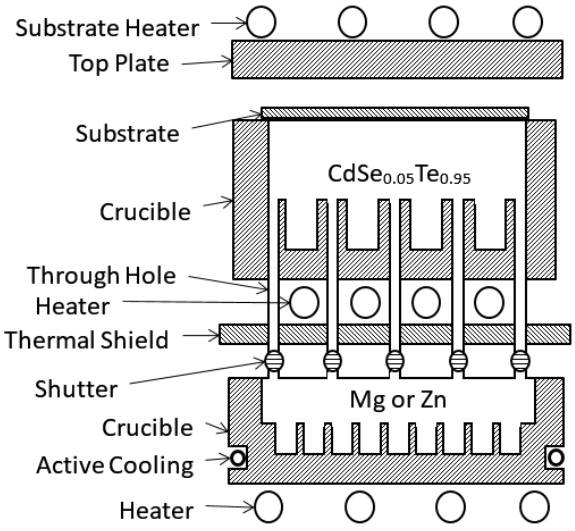

Figure 6-1 Setup for CdTe alloy deposition at Colorado State University.

SE spectra (ψ, Δ) of all the samples were measured from film side between 192–1690 nm (370–1690 nm for CdZnSeTe) wavelength range at three angles (50°, 60°, 70°) of incidence in reflection mode with M2000 rotating compensator ellipsometer from J.A. Woollam Company. A diffusive scotch tape from 3M was attached to the back of the glass to suppress backside reflection. Transmittance between 250–2000 nm wavelengths was measured with 950S Lambda spectrophotometer from PerkinElmer.

6.3 Results and Discussion

6.3.1 TEC-10

CdTe alloys as described in the experimental section were deposited on TEC-10 glass. This is a soda-lime glass with additional layers on it adapted for different applications. They typically are numbered according to their sheet resistance, for example TEC-10 has 10 ohm/square. TEC-10 has tin oxide (SnO_2), silicon oxide (SiO_2) and fluorine doped tin oxide (SnO_2:F) on one side of the glass upon which further layers are deposited. The structure of TEC-10 glass is depicted in Figure 6-2. Before we characterize wide-bandgap CdTe alloys grown on TEC-10, the glass itself has to be modeled. Ideally it would be best to have each layer of TEC-10 characterized with SE separately and then combined in a single model, however, they are not available. So, we have taken the optical

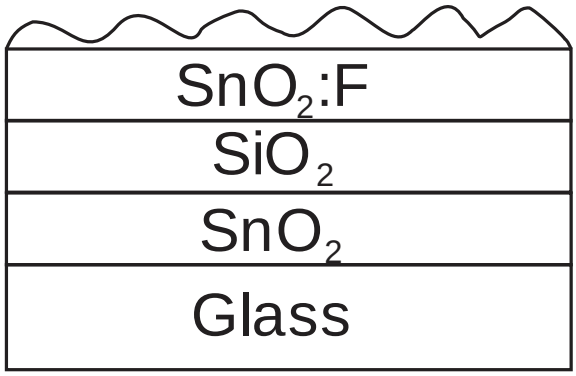

Figure 6-2. Schematic showing the structure of TEC-10 glass.

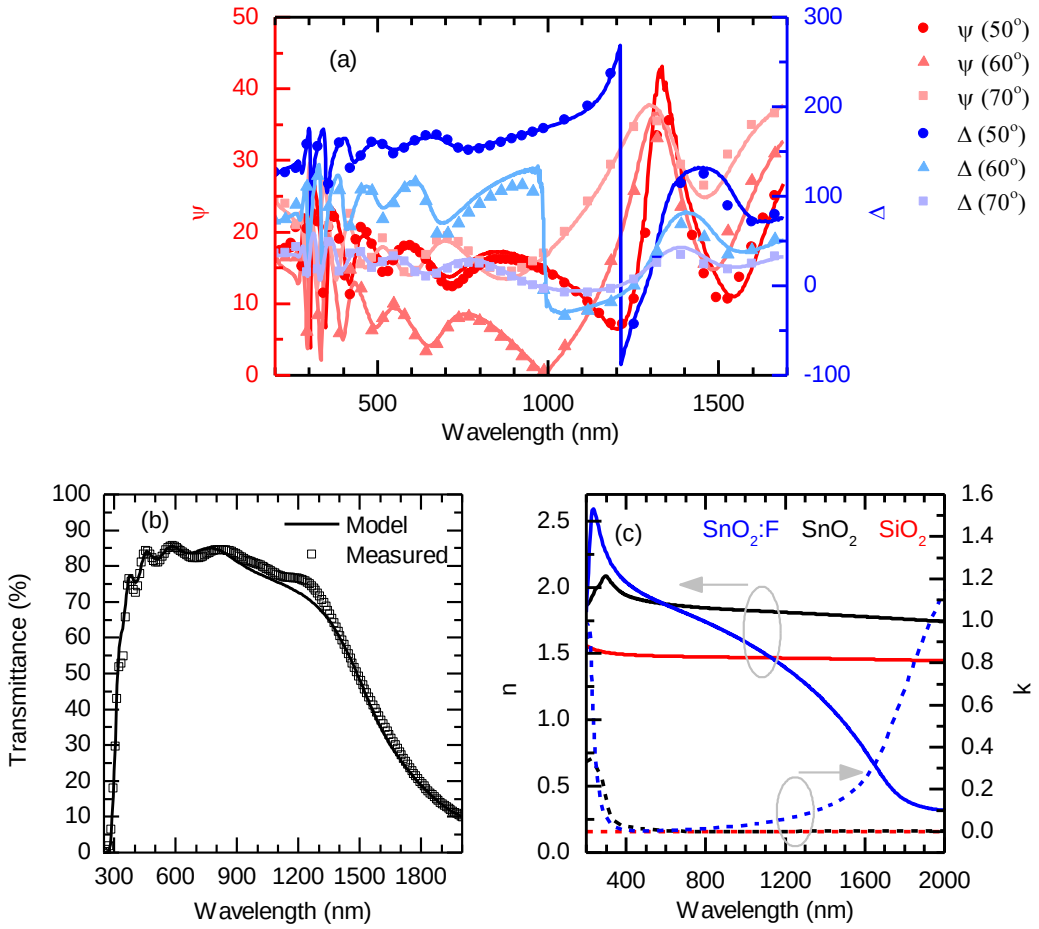

Figure 6-3. Shown are measured SE spectra and fit to it (a) along with transmittance (b). Also shown are the the refractive indices of SiO_2 and SnO_2 taken from literature and optical constants of SnO_2:F determined here (c).

constants for soda-lime glass and two thin layers, that is, SnO_2 and SiO_2 from literature where they were characterized as part of TEC-15 glass [186]. It is important to note that the actual optical properties of these layers in TEC-10 may be different than in TEC-15 but still these are good starting point. The thickest layer of the three is SnO_2:F and thus would have the greatest impact on the optical properties of the substrate. Therefore, we fit the

optical properties of SnO_2:F. As shown in Figure 6-2 this layer also has quite a bit of surface roughness which makes SE analysis difficult.

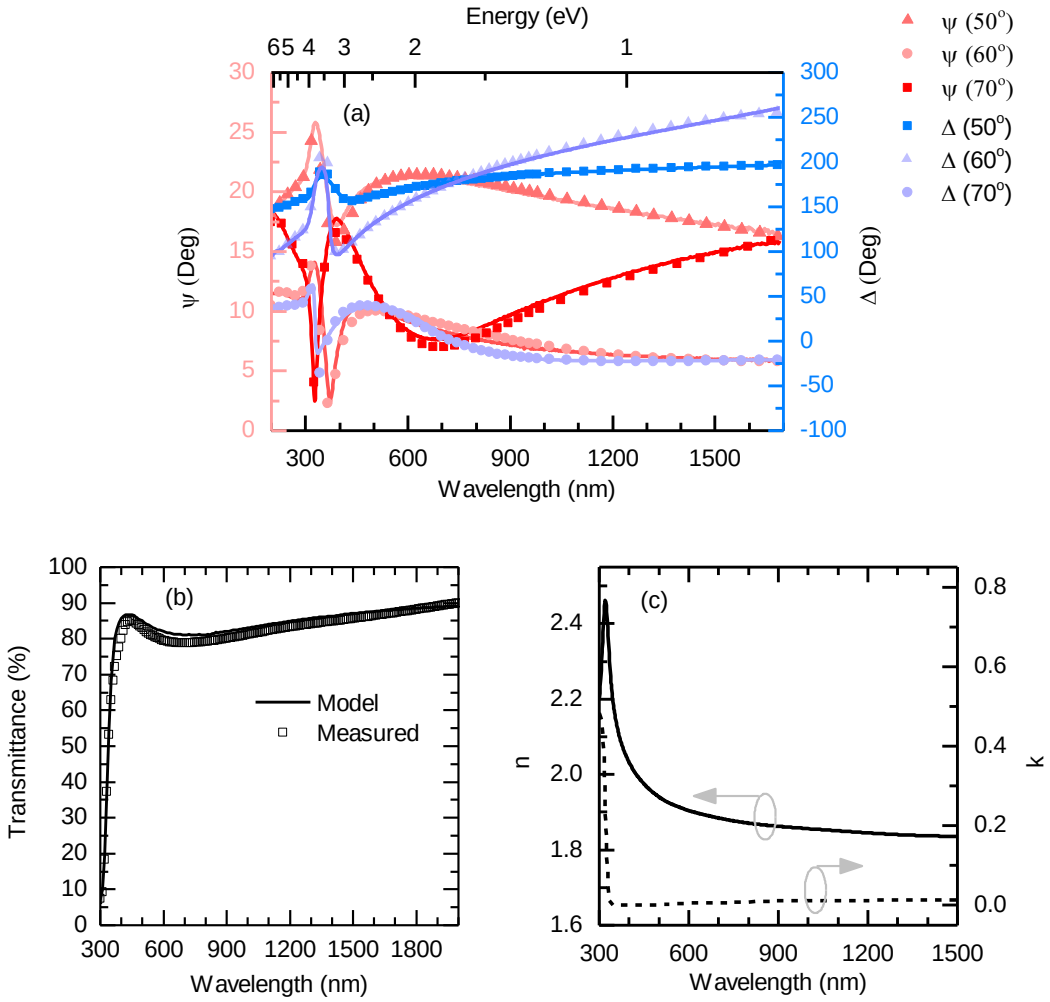

Figure 6-4. Shown are measured SE spectra and fit to it (a) along with transmittance (b). Also shown are the obtained optical constants for MZO (c).

Figure 6-3 shows the measured SE and transmittance spectra for TEC-10. Since the SE spectra was measured in reflection mode so a transmittance data was added to the fitting procedure to allow accurate determination of extinction coefficient. The optical model used for TEC-10 in the fitting procedure is the same as shown in Figure 6-2. During the fitting procedure SnO_2:F is modeled with coupled Tauc-Lorentz (TL) and Drude terms. Whereas

surface roughness is modeled as an effective medium with 50/50% fraction of voids and SnO_2:F according to Bruggeman effective medium approximation. The thickness of the soda-lime glass was fixed at 3 mm whereas the thicknesses of all the other layers were allowed to vary. Optical constants taken from literature for SnO_2 and SiO_2 are also shown in Figure 6-3.

6.3.2 MZO

CdTe solar cells or its wide-bandgap alloys are predominantly made in superstrate configuration. Traditionally cadmium sulfide (CdS) has been used to form a junction with p-type CdTe which is deposited directly on SnO_2:F layer of TEC-10. However, for better band alignment and potentially wider bandgap that could help lower the parasitic absorptance, MZO is used an electron contact here instead of CdS. So next we characterize the optical properties of MZO deposited on Eagle glass. The optical model used in the analysis is surface roughness/bulk layer/glass. The glass substrate is represented with Cauchy model. Figure 6-4 shows the SE and transmittance spectra of the MZO sample along with the fit. Also shown are the obtained optical constants in Figure 4c. Fitting yields a thickness of 102.3 nm for MZO with surface roughness of 7 nm while the target deposition thickness was 100 nm. First, B-Spline was used to fit the SE and transmittance data together, which was then parametrized with a single Tauc-Lorentz oscillator and Drude term. Complex refractive indices of MZO show very similar shape as zinc oxide (ZnO) with the exception that MZO shows non-zero extinction coefficient values in the infrared spectral region. This could be due to free carrier absorption happening in MZO due to Mg doping.

6.3.3 CdTe and $CdSe_xTe_{1-x}$

Before SE analysis is performed on new CdTe alloy absorbers the analysis is performed on poly-CdTe and poly-$CdSe_xTe_{1-x}$ films deposited on TEC-10. The reason for this is to

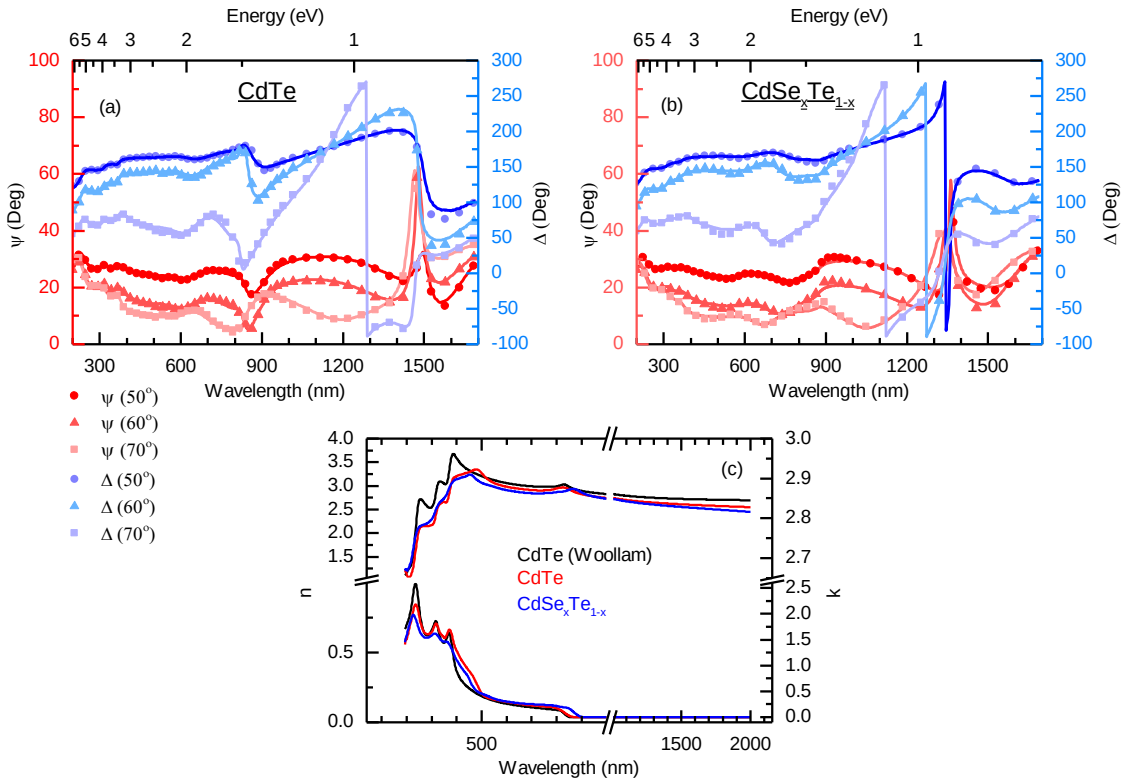

Figure 6-5. Shown are measured SE spectra and fit to it for CdTe (a) and $CdSe_xTe_{1-x}$ (b). Also shown are the obtained optical constants (c).

validate the optical constants obtained previously for TEC-10 glass and MZO electron contact and as well as to validate the fitting procedure by comparing the optical constants for CdTe and $CdSe_xTe_{1-x}$ against those available in the literature [186-188]. The optical constants for crystalline CdTe have been very well characterized and poly-CdTe dielectric function exhibits the same critical points as crystalline CdTe. Thus, verifying that the SE analysis performed results in the same critical point energies would verify the approach. While the optical properties of $CdSe_xTe_{1-x}$ depend on the Se content of the film. Junda *et*

al. has shown that the bandgap of $CdSe_xTe_{1-x}$ shows bowing with the bandgap varying between 1.4–1.75 eV.

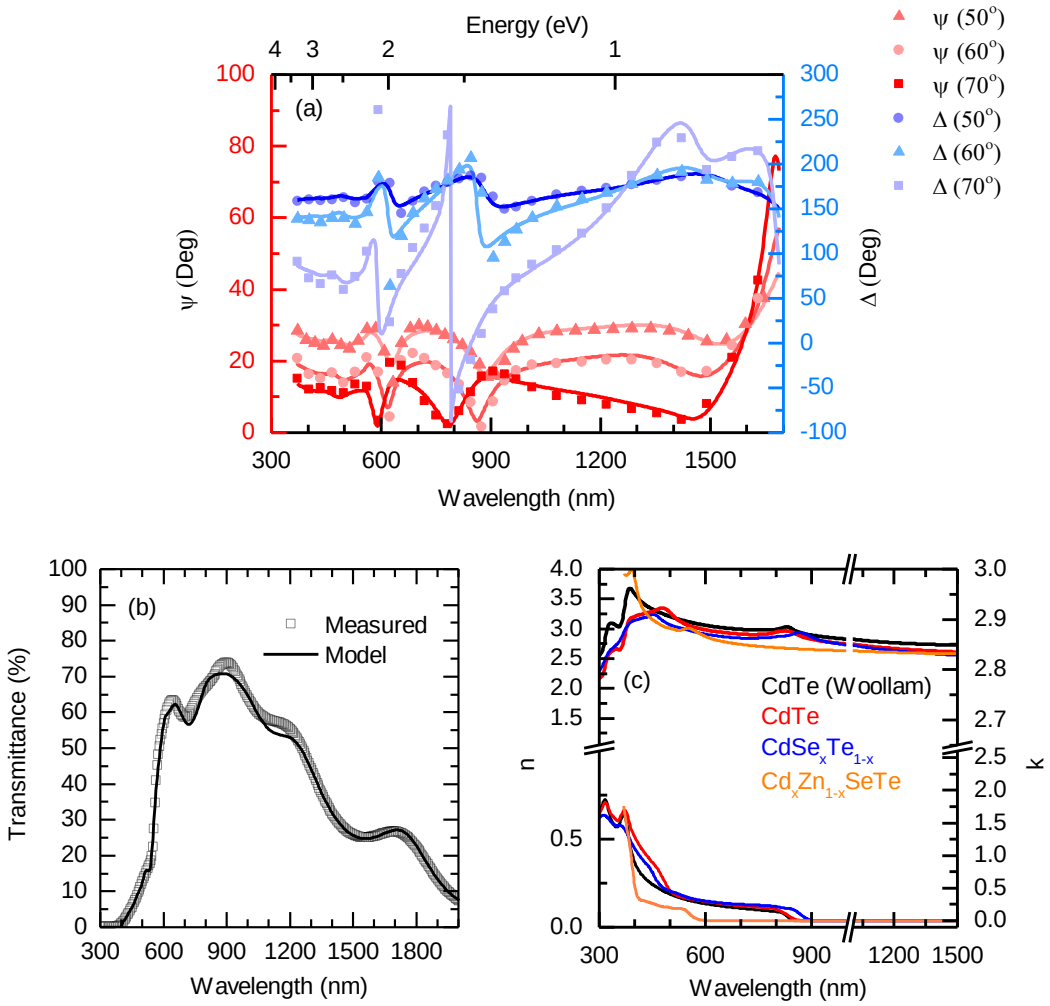

Figure 6-6. Shown are measured SE spectra and fit to it (a) and transmittance (b) for $Cd_xZn_{1-x}SeTe$. Also shown are the obtained optical constants (c).

The optical model used for fitting the CdTe and $CdSe_xTe_{1-x}$ samples were surface roughness/Bulk CdTe or CdSeTe/EMA/SnO_2:F/SiO_2/$SinO_2$/Glass. The surface roughness layer is modeled as an effective medium layer using Bruggeman effective medium approximation with 50% void and 50% underlying layer volume fraction. The measured SE spectra and fits and obtained optical constants are shown in Figure 6-5. Also shown are

the optical constants for crystalline CdTe taken from CompleteEase software from JA Woollam Company. Figure 6-5c clearly shows that poly-CdTe shows the same energy position from critical points as crystalline CdTe. In total there are four distinct critical points. As for $CdSe_xTe_{1-x}$ the main difference is the shift in the position of lowest energy transition, also called bandgap. It shows a red shift in its bandgap. These results validate the fitting procedure and the previously determined optical constants of MZO and TEC-10 glass.

6.3.4 $Cd_xZn_{1-x}SeTe$

Now SE analysis is performed on wide-bandgap $Cd_xZn_{1-x}SeTe$ alloy. The challenge here is that this sample has a rough surface which leads to depolarization of incident light. For this sample a 100 nm of MZO was deposited on TEC-10 followed by CdZnSeTe. The optical model used for fitting the SE spectra is surface roughness layer/bulk CdZnSeTe/EMA/MZO/SnO_2:F/SiO_2/SnO_2/glass. Refractive indices of all the layers are the same as determined earlier except CdZnSeTe. An effect medium layer is introduced at the interface of MZO and CdZnSeTe using Bruggman effective medium approximation with 50%/50% volume fractions of both layers. Similarly, surface roughness layer is also an effective medium layer using the same approximation with 50% of void and 50% of underlying CdZnSeTe volume fraction. The SE spectra and transmittance data is first fitted using B-Spline and then resulting dielectric function is parametrized using Tauc-Lorentz oscillators. The thicknesses of MZO and SnO_2:F was allowed to vary as well. The measured SE spectra and modeled data is shown in Figure 6-6. Optical constants of CdZnSeTe shown in Figure 6-6c reveal a blue shift of bandgap. The exact ratio of Zn and Cd is not characterized in the film but it has a bandgap of 2.1 eV. The composition could

be determined using energy dispersive x-ray spectroscopy (EDS) technique. However SE analysis clearly demonstrates wider bandgap CdTe alloy. With further analysis of the films with varying Zn content and knowledge of the composition of the films a bandgap versus Zn content relationship could determined.

6.4 Conclusion

In conclusion in this chapter a glass substrate, TEC-10, commonly used in superstrate configuration CdTe solar cells is characterized using SE analysis. Also presented are the optical properties of MZO electron contact. The optical properties of substrate and MZO were then validated by characterizing the optical properties of CdTe and $CdSe_xTe_{1-x}$. And finally the complex refractive indices of wide-bandgap $Cd_xZn_{1-x}SeTe$ were determined. However, the roughness of the film is a challenge so polishing the film or performing through-the-glass ellipsometry would yield better estimation of the optical properties.

CHAPTER

7 CONCLUSION AND FUTURE WORK

7.1 Conclusion

Silicon and perovskite based tandems offer the promise of high efficiency solar cells but there are numerous material and optical challenges that have to be surpassed to realize their full potential. Therefore, this work focusses on the light management in these tandems. First, new top- and bottom-cell materials were characterized for their optical properties. Then they were integrated into current and improved tandem device architectures in rigorous optical simulations to arrive at their realistic efficiency limit. Also presented are reflectance and parasitic losses in various layers of the tandem.

Textured surfaces are essential part of high efficiency silicon solar cells as well as thin-film solar cells. First we analyzed the light trapping potential of random pyramids in textured silicon solar cells. For this we accurately captured the 3D height map of random pyramids which show a distribution of base angle centered at an angle less than the 54.7° which is expected for ideal-pyramids. Next we trace light rays inside a wafer bounded on both sides with measured texture and compare its performance against all ideal-random pyramids and Lambertian scaterrer. Comparison is performed through recording the angular distribution function of light rays for each pass. Results showed that ideal-random pyramids is a wrong approximation of real-random pyramids which behave very close to Lambertian scatterer.

Front-surface reflectance is the next problem that was tackled which is a dominant optical loss mechanism in planar solar cells such as single-junction perovskite, perovskite/silicon and perovskite/perovskite tandems. To address this issue a textured

PDMS scattering layer is proposed as a substitute for textured glass to reduce the reflectance loss. Such a scattering layer is produced by replicating random pyramids from alkaline etched silicon wafer using nano-imprint lithography. Next we explored the effectiveness of this approach by putting PDMS scattering layer on the front of no, single-side and double-side textured silicon solar cells. The results showed that PDMS layer on rear-side textured solar cell could perform as well as double-side textured solar cell. We also applied the textured ARC to planar semi-transparent perovskite cell which showed an increase of 10.6% in its efficiency.

The success of perovskite/silicon tandem depends on the optical properties of top-cell such as its bandgap, thickness, parasitic absorptance etc. So next we characterized the optical constants of wide-bandgap perovskites using spectroscopic ellipsometry. Specifically we characterized $Cs_xFA_{1-x}Pb(Br_yI_{1-y})_3$ perovskites with 1.63 eV and 1.68 eV bandgaps which were used in experimentally achieved 23.6 and 25% perovskite/silicon tandems. The accuracy of the optical constants obtained was validated by simulating complementary single-junction perovskite cells and comparing the simulated EQE and reflectance with measured results. After that using the optical constants of $CH_3NH_3I_3$ (1.56 eV) and 1.63 and 1.68 eV perovskites, an empirical formula was developed to determine the optical constants of an arbitrary bandgap perovskite between 1.56–1.68 eV range. Using this formula 2T perovskite/silicon tandem with variable top-cell bandgap and thickness were simulated in different light management schemes to provide a guideline for further development.

A contender for higher efficiency and lower cost to perovskite/silicon tandems are the perovskite/perovskite tandems. However, their efficiencies are lagging to

perovskite/silicon tandems. Challenge is the slow progress of narrow-bandgap perovskites which suffer from stability issues that also restricts lowest bandgaps to be between 1.2–1.25 eV even though the ideal bandgap is less than that. Perovskite/perovskite tandems also share some of the same optical loss mechanisms with perovskite/silicon tandems. So the optical constants of best-in-class 1.22 eV, $Cs_{0.05}FA_{0.45}MA_{0.5}(Sn_{0.5}Pb_{0.5})I_3$ narrow-bandgap perovskite were characterized using spectroscopic ellipsometry. This composition has been employed in experimentally demonstrated 23% efficient 2T perovskite/perovskite tandem. This composition was chosen because it has long carrier diffusion length offering thicker absorber to be made. Obtained optical constants were validated by simulating EQE and reflectance of a complementary single-junction cell and compared to measured cell results. Optical constants were also validated against measured results of 23% efficient 2T tandem. In the end several new tandem designs were simulated with variable top-cell bandgap and thicknesses with 1.22 eV bottom-cell to provide guidance for further development. Results showed with 1.82 eV top-cell and thickness of 690 nm and textured front glass an efficiency as high as 29% could be achieved.

Lastly, spectroscopic ellipsometry was used to study optical properties of CdTe alloys that could be potential candidates for top-cell in II-VI/silicon tandems. Specifically CdZnSeTe absorbers with varying Zn content were analyzed. Before such analysis TEC-10 soda-lime glass with SnO_2:F TCO on it were characterized. Also optical constants of an electron contact that is MZO were determined. The CdTe alloys were deposited by our collaborator at Colorado State University on MZO/TEC-10 substrate and resulted in high film roughness which prevented good fitting of ellipsometric spectra.

7.2 Future Work

The methodology presented in Chapter 2 to capture an accurate height map of a texture and then using ray-tracing to record angular distribution function of light rays inside the substrate is a powerful tool to analyze the light trapping behavior of a texture. It would be interesting to perform similar analysis on texture resulting from isotropic etching of multi-crystalline solar cells as they hold the major share of the world PV market. Such analysis would provide insight into the optical losses in multi-crystalline solar cells and potential improvements.

The work presented in Chapter 3 where random pyramids were replicated into PDMS from textured silicon could be extended to other texture types and materials to investigate their antireflection and light-trapping behavior. It would be very interesting to implement a nano-texture which effectively reduces reflectance but would not scatter the light. This would be great for small-area devices which could lose light due to scattering. Another important direction that could be taken is to design the texture to have antireflection role but also to have the role of anti-soiling. The goal should be to use the combination of texture and material to achieve antireflection and hydrophobicity or hydrophilicity.

The work presented in Chapter 4 and 5 on the optical modeling of wide- and narrow-bandgap perovskites and perovskite/silicon and perovskite/perovskite tandems could be extended to perform search for optically favorable inter-connecting layers and electron and hole contacts. Furthermore, this study could be expanded to explore new tandem designs such as where perovskite absorber could fill up the depth of the texture to form a planar surface. Moreover, there is a need to optimize these tandems for maximum annual energy yield which depends on the location of deployment due to variation in solar spectrum. This

is because a change in irradiation would change the condition for current-matching. In addition to optical simulations of tandems it is imperative to couple them to thermal simulations to model the performance of these tandems in the field over time. Then materials could be chosen that keep the cell and module temperatures low. To couple optical and thermal simulations, the perovskite absorber optical properties would have to be characterized for different temperatures using ellipsometry. Lastly, specific to perovskite/perovskite tandems, corresponding to 1.2 eV bottom-cell a wide-bandgap perovskite of 1.8 eV is required. However, it is challenging to make 1.8 eV wide-bandgap perovskite due to halide segregation. But this top-cell bandgap requirement could be reduced to lower bandgaps if the 2T tandem is made bifacial. The reason is that narrow-bandgap bottom-cell would now produce higher J_{sc} and so top-cell could be matched at higher J_{sc} too by having lower bandgap.

Lastly, the spectroscopic ellipsometry study of wide-bandgap CdTe alloys presented in Chapter 6 has been limited due to the roughness of the samples. So the analysis could be performed by through the glass ellipsometry or polishing the film surface by etching it. These approaches would allow accurate determination of optical properties of wide-bandgap CdTe alloys such as bandgap, voids, strain and defects and also relate them to process parameters. With such analysis growth conditions could be optimized.

REFERENCES

[1] "Fraunhofer ISE, "Photovoltaics report-2017," Freiburg, 2017."

[2] J. Trube, "International Technology Roadmap for Photovoltaic (ITRPV)," *VDMA photovoltaic equipement,* 2018.

[3] A. Richter, M. Hermle, and S. W. Glunz, "Reassessment of the limiting efficiency for crystalline silicon solar cells," *IEEE journal of photovoltaics,* vol. 3, no. 4, pp. 1184-1191, 2013.

[4] K. Yoshikawa *et al.*, "Exceeding conversion efficiency of 26% by heterojunction interdigitated back contact solar cell with thin film Si technology," *Solar Energy Materials and Solar Cells,* vol. 173, pp. 37-42, 2017.

[5] K. Yoshikawa *et al.*, "Silicon heterojunction solar cell with interdigitated back contacts for a photoconversion efficiency over 26%," *Nature Energy*, vol. 2, no. 5, p. 17032, 2017.

[6] M. A. Green, E. D. Dunlop, D. H. Levi, J. Hohl-Ebinger, M. Yoshita, and A. W. Ho-Baillie, "Solar cell efficiency tables (version 54)," *Progress in Photovoltaics: Research and Applications,* vol. 27, no. NREL/JA-5K00-74116, 2019.

[7] M. A. Woodhouse, B. Smith, A. Ramdas, and R. M. Margolis, "Crystalline Silicon Photovoltaic Module Manufacturing Costs and Sustainable Pricing: 1H 2018 Benchmark and Cost Reduction Road Map," National Renewable Energy Lab.(NREL), Golden, CO (United States)2019.

[8] Z. J. Yu, J. V. Carpenter, and Z. C. Holman, "Techno-economic viability of silicon-based tandem photovoltaic modules in the United States," *Nature Energy,* vol. 3, p. 747, 2018.

[9] W. Shockley and H. J. Queisser, "Detailed balance limit of efficiency of p-n junction solar cells," *Journal of applied physics,* vol. 32, no. 3, pp. 510-519, 1961.

[10] L. Hirst and N. Ekins-Daukes, "Fundamental losses in solar cells," *Progress in Photovoltaics: Research and Applications,* vol. 19, no. 3, pp. 286-293, 2011.

[11] T. Leijtens, K. A. Bush, R. Prasanna, and M. D. McGehee, "Opportunities and challenges for tandem solar cells using metal halide perovskite semiconductors," *Nature Energy,* p. 1, 2018.

[12] Z. J. Yu, M. Leilaeioun, and Z. Holman, "Selecting tandem partners for silicon solar cells," *Nature Energy,* vol. 1, p. 16137, 2016.

[13] F. Meillaud, A. Shah, C. Droz, E. Vallat-Sauvain, and C. Miazza, "Efficiency limits for single-junction and tandem solar cells," *Solar energy materials and solar cells*, vol. 90, no. 18-19, pp. 2952-2959, 2006.

[14] K. Bertness, S. R. Kurtz, D. J. Friedman, A. Kibbler, C. Kramer, and J. Olson, "29.5%-efficient GaInP/GaAs tandem solar cells," *Applied Physics Letters*, vol. 65, no. 8, pp. 989-991, 1994.

[15] J. Geisz, J. Olson, D. Friedman, K. Jones, R. Reedy, and M. Romero, "Lattice-matched GaNPAs-on-silicon tandem solar cells," in *Photovoltaic Specialists Conference, 2005. Conference Record of the Thirty-first IEEE*, 2005, pp. 695-698: IEEE.

[16] K. Derendorf *et al.*, "Fabrication of GaInP/GaAs//Si solar cells by surface activated direct wafer bonding," *IEEE Journal of Photovoltaics*, vol. 3, no. 4, pp. 1423-1428, 2013.

[17] D. E. Swanson *et al.*, "CdCl2 passivation of polycrystalline CdMgTe and CdZnTe absorbers for tandem photovoltaic cells," *Journal of Applied Physics*, vol. 123, no. 20, p. 203101, 2018.

[18] Available: NREL Efficiency Chart (https://www.nrel.gov/pv/assets/images/efficiency-chart.png).

[19] K. A. Bush *et al.*, "23.6%-efficient monolithic perovskite/silicon tandem solar cells with improved stability," *Nature Energy*, vol. 2, p. 17009, 2017.

[20] M. Jošt *et al.*, "Textured interfaces in monolithic perovskite/silicon tandem solar cells: advanced light management for improved efficiency and energy yield," *Energy & Environmental Science*, 2018.

[21] T. Duong *et al.*, "Rubidium Multication Perovskite with Optimized Bandgap for Perovskite-Silicon Tandem with over 26% Efficiency," *Advanced Energy materials*, vol. 7, no. 14, 2017.

[22] D. Zhao *et al.*, "Four-terminal all-perovskite tandem solar cells achieving power conversion efficiencies exceeding 23%," *ACS Energy Letters*, vol. 3, no. 2, pp. 305-306, 2018.

[23] G. E. Eperon *et al.*, "Perovskite-perovskite tandem photovoltaics with optimized band gaps," *Science*, vol. 354, no. 6314, pp. 861-865, 2016.

[24] D. Forgacs *et al.*, "Efficient monolithic perovskite/perovskite tandem solar cells," *Advanced Energy Materials*, vol. 7, no. 8, p. 1602121, 2017.

[25] A. Rajagopal *et al.*, "Highly efficient perovskite–perovskite tandem solar cells reaching 80% of the theoretical limit in photovoltage," *Advanced Materials,* vol. 29, no. 34, p. 1702140, 2017.

[26] R. Lin *et al.*, "Monolithic all-perovskite tandem solar cells with 24.8% efficiency exploiting comproportionation to suppress Sn(ii) oxidation in precursor ink," *Nature Energy,* 2019/09/23 2019.

[27] Z. Holman and M. Boccard, "“Light management in silicon solar cells,”" in *Photovoltaics: From fundamentals to applications*, A. Reinders, P. Verlinden, W. van Sark, and A. Freundlich, Eds.: Wiley, 2017.

[28] F. Sahli *et al.*, "Fully textured monolithic perovskite/silicon tandem solar cells with 25.2% power conversion efficiency," *Nature materials,* p. 1, 2018.

[29] B. Chen *et al.*, "Grain Engineering for Perovskite/Silicon Monolithic Tandem Solar Cells with Efficiency of 25.4%," *Joule,* 2018.

[30] E. Yablonovitch, "Statistical ray optics," *JOSA,* vol. 72, no. 7, pp. 899-907, 1982.

[31] C. Barugkin, T. Allen, T. K. Chong, T. P. White, K. J. Weber, and K. R. Catchpole, "Light trapping efficiency comparison of Si solar cell textures using spectral photoluminescence," *Optics express,* vol. 23, no. 7, pp. A391-A400, 2015.

[32] C. S. Schuster, A. Bozzola, L. C. Andreani, and T. F. Krauss, "How to assess light trapping structures versus a Lambertian Scatterer for solar cells?," *Optics Express,* vol. 22, no. 102, pp. A542-A551, 2014.

[33] R. Brendel, "Coupling of light into mechanically textured silicon solar cells: A ray tracing study," *Progress in Photovoltaics: Research and Applications,* vol. 3, no. 1, pp. 25-38, 1995.

[34] P. Campbell and M. A. Green, "Light trapping properties of pyramidally textured surfaces," (in English), *Journal of Applied Physics,* Article vol. 62, no. 1, pp. 243-249, Jul 1987.

[35] H. Sai *et al.*, "Wide-angle antireflection effect of subwavelength structures for solar cells," *Japanese journal of applied physics,* vol. 46, no. 6R, p. 3333, 2007.

[36] A. Gombert and A. Luque, "Photonics in photovoltaic systems," *physica status solidi (a),* vol. 205, no. 12, pp. 2757-2765, 2008.

[37] S. Albrecht *et al.*, "Monolithic perovskite/silicon-heterojunction tandem solar cells processed at low temperature," *Energy & Environmental Science,* vol. 9, no. 1, pp. 81-88, 2016.

[38] J. Werner *et al.*, "Efficient monolithic perovskite/silicon tandem solar cell with cell area> 1 cm2," *The journal of physical chemistry letters,* vol. 7, no. 1, pp. 161-166, 2015.

[39] R. Cariou *et al.*, "Monolithic Two-Terminal III–V//Si Triple-Junction Solar Cells With 30.2% Efficiency Under 1-Sun AM1. 5g," *IEEE Journal of Photovoltaics,* vol. 7, no. 1, pp. 367-373, 2017.

[40] J. Escarré, K. Söderström, C. Battaglia, F.-J. Haug, and C. Ballif, "High fidelity transfer of nanometric random textures by UV embossing for thin film solar cells applications," *Solar Energy Materials and Solar Cells,* vol. 95, no. 3, pp. 881-886, 2011.

[41] C. Battaglia *et al.*, "Efficient light management scheme for thin film silicon solar cells via transparent random nanostructures fabricated by nanoimprinting," *Applied Physics Letters,* vol. 96, no. 21, p. 213504, 2010.

[42] J. Chen and K. Sun, "Enhancement of the light conversion efficiency of silicon solar cells by using nanoimprint anti-reflection layer," *Solar Energy Materials and Solar Cells,* vol. 94, no. 3, pp. 629-633, 2010.

[43] M. Jošt *et al.*, "Back-and Front-side Texturing for Light-management in Perovskite/Silicon-heterojunction Tandem Solar Cells," *Energy Procedia,* vol. 102, pp. 43-48, 2016.

[44] J. Escarre *et al.*, "Geometric light trapping for high efficiency thin film silicon solar cells," *Solar Energy Materials and Solar Cells,* vol. 98, pp. 185-190, 2012.

[45] J. P. Mailoa *et al.*, "A 2-terminal perovskite/silicon multijunction solar cell enabled by a silicon tunnel junction," *Applied Physics Letters,* vol. 106, no. 12, p. 121105, 2015.

[46] P. Löper *et al.*, "Organic–inorganic halide perovskite/crystalline silicon four-terminal tandem solar cells," *Physical Chemistry Chemical Physics,* vol. 17, no. 3, pp. 1619-1629, 2015.

[47] T. Duong *et al.*, "Semitransparent perovskite solar cell with sputtered front and rear electrodes for a four-terminal tandem," *IEEE Journal of Photovoltaics,* vol. 6, no. 3, pp. 679-687, 2016.

[48] J. M. Rodríguez, I. Tobías, and A. Luque, "Random pyramidal texture modelling," *Solar Energy Materials and Solar Cells,* vol. 45, no. 3, pp. 241-253, 2/15/ 1997.

[49] G. Kuchler and R. Brendel, "Reconstruction of the surface topography of randomly textured silicon," (in English), *Progress in Photovoltaics,* vol. 11, no. 2, pp. 89-95, Mar 2003.

[50] P. Campbell, "ENHANCEMENT OF LIGHT-ABSORPTION FROM RANDOMIZING AND GEOMETRIC TEXTURES," (in English), *Journal of the Optical Society of America B-Optical Physics,* Article vol. 10, no. 12, pp. 2410-2415, Dec 1993.

[51] P. Campbell, "LIGHT TRAPPING IN TEXTURED SOLAR-CELLS," (in English), *Solar Energy Materials,* Article vol. 21, no. 2-3, pp. 165-172, Dec 1990.

[52] P. Campbell and M. A. Green, "High performance light trapping textures for monocrystalline silicon solar cells," *Solar Energy Materials and Solar Cells,* vol. 65, no. 1-4, pp. 369-375, Jan 2001.

[53] P. Campbell, S. R. Wenham, and M. A. Green, "Light Trapping and Reflection Control in Solar-Cells Using Tilted Crystallographic Surface Textures," (in English), *Solar Energy Materials and Solar Cells,* vol. 31, no. 2, pp. 133-153, Nov 1993.

[54] R. Brendel, "COUPLING OF LIGHT INTO MECHANICALLY TEXTURED SILICON SOLAR-CELLS - A RAY-TRACING STUDY," *Progress in Photovoltaics,* vol. 3, no. 1, pp. 25-38, Jan-Feb 1995.

[55] A. Luque and J. C. Miñano, "Optical aspects in photovoltaic energy conversion," *Solar cells,* vol. 31, no. 3, pp. 237-258, 1991.

[56] J. C. Miñano, "Optical confinement in photovoltaics," *Physical limitations to photovoltaic energy conversion,* pp. 50-83, 1990.

[57] U. Rau, U. W. Paetzold, and T. Kirchartz, "Thermodynamics of light management in photovoltaic devices," *Physical Review B,* vol. 90, no. 3, p. 035211, 2014.

[58] P. Campbell and M. A. Green, "The limiting efficiency of silicon solar cells under concentrated sunlight," *IEEE Transactions on Electron Devices,* vol. 33, no. 2, pp. 234-239, 1986.

[59] S. C. Baker-Finch and K. R. McIntosh, "Reflection distributions of textured monocrystalline silicon: implications for silicon solar cells," *Progress in Photovoltaics: Research and Applications,* pp. n/a-n/a, 2012.

[60] H. Mackel, H. Holst, M. Lohmann, E. Wefringhaus, and P. P. Altermatt, "Detailed Analysis of Random Pyramid Surfaces With Ray Tracing and Image Processing," (in English), *IEEE Journal of Photovoltaics,* vol. 6, no. 6, pp. 1456-1465, Nov 2016.

[61] Z. C. Holman, S. De Wolf, and C. Ballif, "Improving metal reflectors by suppressing surface plasmon polaritons: A priori calculation of the internal reflectance of a solar cell," *Light: Science & Applications,* vol. 2, p. e106, 2013.

[62] Z. C. Holman *et al.*, "Infrared light management in high-efficiency silicon heterojunction and rear-passivated solar cells," *Journal of Applied Physics,* vol. 113, p. 013107, 2013.

[63] Z. C. Holman *et al.*, "Parasitic absorption in the rear reflector of a silicon solar cell: Simulation and measurement of the sub-bandgap reflectance for common dielectric/metal reflectors," *Solar Energy Materials and Solar Cells,* vol. 120, Part A, no. 0, pp. 426-430, 1// 2014.

[64] B. Lipovšek, J. Krč, and M. Topič, "Optical model for thin-film photovoltaic devices with large surface textures at the front side," *Informacije Midem,* vol. 41, no. 4, pp. 264-271, 2011.

[65] M. Filipič *et al.*, "CH 3 NH 3 PbI 3 perovskite/silicon tandem solar cells: characterization based optical simulations," *Optics express,* vol. 23, no. 7, pp. A263-A278, 2015.

[66] Z. C. Holman *et al.*, "Parasitic absorption in the rear reflector of a silicon solar cell: Simulation and measurement of the sub-bandgap reflectance for common dielectric/metal reflectors," *Solar Energy Materials and Solar Cells,* vol. 120, pp. 426-430, 2014.

[67] K. L. Westra, A. W. Mitchell, and D. J. Thomson, "Tip Artifacts in Atomic-Force Microscope Imaging of Thin-Film Surfaces," (in English), *Journal of Applied Physics,* vol. 74, no. 5, pp. 3608-3610, Sep 1 1993.

[68] C. Canale, B. Torre, D. Ricci, and P. C. Braga, "Recognizing and Avoiding Artifacts in Atomic Force Microscopy Imaging," in *Atomic Force Microscopy in Biomedical Research: Methods and Protocols*, C. P. Braga and D. Ricci, Eds. Totowa, NJ: Humana Press, 2011, pp. 31-43.

[69] F. J. Haug, M. Bräuninger, and C. Ballif, "Fourier light scattering model for treating textures deeper than the wavelength," *Optics Express,* vol. 25, no. 4, pp. A14-A22, 2017/02/20 2017.

[70] J. C. Pla, J. C. Duran, D. C. Skigin, and R. A. Depine, "Ray tracing vs. electromagnetic methods in the analysis of antireflective textured surfaces," presented at the 26th IEEE PVSC, Anaheim, CA, 1997.

[71] S. C. Baker-Finch and K. R. McIntosh, "Reflection distributions of textured monocrystalline silicon: implications for silicon solar cells," *Progress in photovoltaics: Research and Applications,* vol. 21, no. 5, pp. 960-971, 2013.

[72] J. T. L. Thong, P. Luo, W. K. Choi, and S. C. Tan, "Evolution of hillocks during silicon etching in TMAH," (in English), *Journal of Micromechanics and Microengineering,* vol. 11, no. 1, pp. 61-69, Jan 2001.

[73] E. Fornies, C. Zaldo, and J. M. Albella, "Control of random texture of monocrystalline silicon cells by angle-resolved optical reflectance," (in English), *Solar Energy Materials and Solar Cells,* vol. 87, no. 1-4, pp. 583-593, May 2005.

[74] M. Boccard, C. Battaglia, F.-J. Haug, M. Despeisse, and C. Ballif, "Light trapping in solar cells: Analytical modeling," *Applied Physics Letters,* vol. 101, no. 15, p. 151105, 2012.

[75] H. Deckman, C. Wronski, H. Witzke, and E. Yablonovitch, "Optically enhanced amorphous silicon solar cells," *Applied Physics Letters,* vol. 42, no. 11, pp. 968-970, 1983.

[76] S. C. Baker-Finch, K. R. McIntosh, and M. L. Terry, "Isotextured silicon solar cell analysis and modeling 1: Optics," *IEEE Journal of Photovoltaics,* vol. 2, no. 4, pp. 457-464, 2012.

[77] K. R. McIntosh, T. G. Allen, S. C. Baker-Finch, and M. D. Abbott, "Light trapping in isotextured silicon wafers," *IEEE Journal of Photovoltaics,* vol. 7, no. 1, pp. 110-117, 2017.

[78] P. Buehlmann, A. Billet, J. Bailat, and C. Ballif, "Anti-reflection layer at the TCO/Si interface for high efficiency thin-film solar cells deposited on rough LP-CVD front ZnO," 2007.

[79] P. Cuony *et al.*, "Mixed-phase p-type silicon oxide containing silicon nanocrystals and its role in thin-film silicon solar cells," *Applied Physics Letters,* vol. 97, no. 21, p. 213502, 2010.

[80] M. Berginski *et al.*, "The effect of front ZnO: Al surface texture and optical transparency on efficient light trapping in silicon thin-film solar cells," *Journal of applied physics,* vol. 101, no. 7, p. 074903, 2007.

[81] J.-H. Im, I.-H. Jang, N. Pellet, M. Grätzel, and N.-G. Park, "Growth of CH3NH3PbI3 cuboids with controlled size for high-efficiency perovskite solar cells," *Nature nanotechnology,* vol. 9, no. 11, pp. 927-932, 2014.

[82] D. Liu and T. L. Kelly, "Perovskite solar cells with a planar heterojunction structure prepared using room-temperature solution processing techniques," *Nature photonics,* vol. 8, no. 2, pp. 133-138, 2014.

[83] L. Zheng *et al.*, "Improved light absorption and charge transport for perovskite solar cells with rough interfaces by sequential deposition," *Nanoscale,* vol. 6, no. 14, pp. 8171-8176, 2014.

[84] A. R. Pascoe *et al.*, "Enhancing the Optoelectronic Performance of Perovskite Solar Cells via a Textured CH3NH3PbI3 Morphology," *Advanced Functional Materials,* 2015.

[85] W. Jaegermann, A. Klein, and T. Mayer, "Interface Engineering of Inorganic Thin-Film Solar Cells–Materials-Science Challenges for Advanced Physical Concepts," *Advanced Materials,* vol. 21, no. 42, pp. 4196-4206, 2009.

[86] J. Fritsche *et al.*, "Surface analysis of CdTe thin film solar cells," *Thin Solid Films,* vol. 387, no. 1, pp. 161-164, 2001.

[87] J. R. Sites, J. Granata, and J. Hiltner, "Losses due to polycrystallinity in thin-film solar cells," *Solar Energy Materials and Solar Cells,* vol. 55, no. 1, pp. 43-50, 1998.

[88] F.-J. Haug, T. Söderström, M. Python, V. Terrazzoni-Daudrix, X. Niquille, and C. Ballif, "Development of micromorph tandem solar cells on flexible low-cost plastic substrates," *Solar Energy Materials and Solar Cells,* vol. 93, no. 6, pp. 884-887, 2009.

[89] K. Tanabe, K. Watanabe, and Y. Arakawa, "III-V/Si hybrid photonic devices by direct fusion bonding," *Scientific reports,* vol. 2, p. 349, 2012.

[90] M. Umeno, T. Soga, K. Baskar, and T. Jimbo, "Heteroepitaxial technologies on Si for high-efficiency solar cells," *Solar energy materials and solar cells,* vol. 50, no. 1-4, pp. 203-212, 1998.

[91] C.-W. Chen, S.-Y. Hsiao, C.-Y. Chen, H.-W. Kang, Z.-Y. Huang, and H.-W. Lin, "Optical properties of organometal halide perovskite thin films and general device structure design rules for perovskite single and tandem solar cells," *Journal of Materials Chemistry A,* vol. 3, no. 17, pp. 9152-9159, 2015.

[92] H. Liu, Z. Ren, Z. Liu, A. G. Aberle, T. Buonassisi, and I. M. Peters, "The realistic energy yield potential of GaAs-on-Si tandem solar cells: a theoretical case study," *Optics express,* vol. 23, no. 7, pp. A382-A390, 2015.

[93] X. Wang and A. Barnett, "The effect of spectrum variation on the energy production of triple-junction solar cells," *IEEE Journal of Photovoltaics,* vol. 2, no. 4, pp. 417-423, 2012.

[94] C. Ballif, J. Dicker, D. Borchert, and T. Hofmann, "Solar glass with industrial porous SiO_2 antireflection coating: measurements of photovoltaic module properties improvement and modelling of yearly energy yield gain," *Solar energy materials and solar cells,* vol. 82, no. 3, pp. 331-344, 2004.

[95] P.-K. Chang, P.-T. Hsieh, F.-J. Tsai, C.-H. Lu, C.-H. Yeh, and M.-P. Houng, "Improvement of the short-circuit current density and efficiency in micromorph tandem solar cells by an anti-reflection layer," *Thin Solid Films,* vol. 520, no. 1, pp. 550-553, 2011.

[96] D. Bouhafs, A. Moussi, A. Chikouche, and J. Ruiz, "Design and simulation of antireflection coating systems for optoelectronic devices: Application to silicon

solar cells," *Solar Energy Materials and Solar Cells*, vol. 52, no. 1-2, pp. 79-93, 1998.

[97] K. Fleischer, E. Arca, and I. Shvets, "Improving solar cell efficiency with optically optimised TCO layers," *Solar Energy Materials and Solar Cells*, vol. 101, pp. 262-269, 2012.

[98] D. J. Aiken, "High performance anti-reflection coatings for broadband multi-junction solar cells," (in English), *Solar Energy Materials and Solar Cells*, vol. 64, no. 4, pp. 393-404, Nov 2000.

[99] Y. M. Song, J. S. Yu, and Y. T. Lee, "Antireflective submicrometer gratings on thin-film silicon solar cells for light-absorption enhancement," *Optics letters*, vol. 35, no. 3, pp. 276-278, 2010.

[100] C. Ulbrich, A. Gerber, K. Hermans, A. Lambertz, and U. Rau, "Analysis of short circuit current gains by an anti-reflective textured cover on silicon thin film solar cells," *Progress in Photovoltaics: Research and Applications*, vol. 21, no. 8, pp. 1672-1681, 2013.

[101] M. Jošt *et al.*, "Efficient Light Management by Textured Nanoimprinted Layers for Perovskite Solar Cells," *ACS Photonics*, 2017.

[102] K. R. McIntosh, J. N. Cotsell, J. S. Cumpston, A. W. Norris, N. E. Powell, and B. M. Ketola, "An optical comparison of silicone and EVA encapsulants for conventional silicon PV modules: A ray-tracing study," in *Photovoltaic Specialists Conference (PVSC), 2009 34th IEEE*, 2009, pp. 000544-000549: IEEE.

[103] K. R. McIntosh, N. E. Powell, A. W. Norris, J. N. Cotsell, and B. M. Ketola, "The effect of damp-heat and UV aging tests on the optical properties of silicone and EVA encapsulants," *Progress in Photovoltaics: Research and Applications*, vol. 19, no. 3, pp. 294-300, 2011.

[104] S. Manzoor, M. Filipič, M. Topič, and Z. Holman, "Revisiting light trapping in silicon solar cells with random pyramids," in *Photovoltaic Specialists Conference (PVSC), 2016 IEEE 43rd*, 2016, pp. 2952-2954: IEEE.

[105] M. Leilaeioun, Z. J. Yu, and Z. Holman, "Optimization of front TCO layer of silicon heterojunction solar cells for tandem applications," in *Photovoltaic Specialists Conference (PVSC), 2016 IEEE 43rd*, 2016, pp. 0681-0684: IEEE.

[106] C. Con and B. Cui, "Effect of mold treatment by solvent on PDMS molding into nanoholes," *Nanoscale research letters*, vol. 8, no. 1, p. 394, 2013.

[107] P. Van Nijnatten, "An automated directional reflectance/transmittance analyser for coating analysis," *Thin Solid Films*, vol. 442, no. 1, pp. 74-79, 2003.

[108] P. A. van Nijnatten, J. de Wolf, and I. Schoofs, "Automated Reflectance/Transmittance Analyzer for Variable Angle Spectrometry."

[109] *PV Lighthouse: SunSolve*. Available: https://www.pvlighthouse.com.au

[110] K.-U. Ritzau, T. Behrendt, D. Palaferri, M. Bivour, and M. Hermle, "Hydrogen doping of Indium Tin Oxide due to thermal treatment of hetero-junction solar cells," *Thin Solid Films,* vol. 599, pp. 161-165, 2016.

[111] M. A. Green, "Self-consistent optical parameters of intrinsic silicon at 300K including temperature coefficients," *Solar Energy Materials and Solar Cells,* vol. 92, no. 11, pp. 1305-1310, 2008.

[112] Y. Jiang, S. Pillai, and M. A. Green, "Realistic Silver Optical Constants for Plasmonics," *Scientific Reports,* vol. 6, 2016.

[113] I. M. Peters, "Phase space considerations for light path lengths in planar, isotropic absorbers," *Optics express,* vol. 22, no. 103, pp. A908-A920, 2014.

[114] K. Soderstrom, "Coupling light into thin silicon layers for high-efficiency solar cells," PhD, Ecole Polytechnique Federale de Lausanne, 2013.

[115] G. E. Eperon, S. D. Stranks, C. Menelaou, M. B. Johnston, L. M. Herz, and H. J. Snaith, "Formamidinium lead trihalide: a broadly tunable perovskite for efficient planar heterojunction solar cells," *Energy & Environmental Science,* vol. 7, no. 3, pp. 982-988, 2014.

[116] L. Protesescu *et al.*, "Nanocrystals of cesium lead halide perovskites (CsPbX3, X= Cl, Br, and I): novel optoelectronic materials showing bright emission with wide color gamut," *Nano letters,* vol. 15, no. 6, pp. 3692-3696, 2015.

[117] Z. Xiao *et al.*, "Efficient perovskite light-emitting diodes featuring nanometre-sized crystallites," *Nature Photonics,* vol. 11, no. 2, p. 108, 2017.

[118] Z.-K. Tan *et al.*, "Bright light-emitting diodes based on organometal halide perovskite," *Nature nanotechnology,* vol. 9, no. 9, pp. 687-692, 2014.

[119] L. Protesescu *et al.*, "Dismantling the “Red Wall” of Colloidal Perovskites: Highly Luminescent Formamidinium and Formamidinium–Cesium Lead Iodide Nanocrystals," *ACS nano,* vol. 11, no. 3, pp. 3119-3134, 2017.

[120] Q. Zhou, Z. Bai, W. g. Lu, Y. Wang, B. Zou, and H. Zhong, "In Situ Fabrication of Halide Perovskite Nanocrystal-Embedded Polymer Composite Films with Enhanced Photoluminescence for Display Backlights," *Advanced Materials,* vol. 28, no. 41, pp. 9163-9168, 2016.

[121] G. Xing *et al.*, "Low-temperature solution-processed wavelength-tunable perovskites for lasing," *Nature materials,* vol. 13, no. 5, p. 476, 2014.

[122] F. Deschler *et al.*, "High photoluminescence efficiency and optically pumped lasing in solution-processed mixed halide perovskite semiconductors," *The journal of physical chemistry letters,* vol. 5, no. 8, pp. 1421-1426, 2014.

[123] J. W. Lee, D. H. Kim, H. S. Kim, S. W. Seo, S. M. Cho, and N. G. Park, "Formamidinium and cesium hybridization for photo-and moisture-stable perovskite solar cell," *Advanced Energy Materials,* vol. 5, no. 20, 2015.

[124] M. Saliba *et al.*, "Cesium-containing triple cation perovskite solar cells: improved stability, reproducibility and high efficiency," *Energy & Environmental Science,* vol. 9, no. 6, pp. 1989-1997, 2016.

[125] T. Todorov *et al.*, "Monolithic Perovskite-CIGS Tandem Solar Cells via In Situ Band Gap Engineering," *Advanced Energy Materials,* vol. 5, no. 23, 2015.

[126] H. Shen *et al.*, "Mechanically-stacked Perovskite/CIGS Tandem Solar Cells with Efficiency of 23.9% and Reduced Oxygen Sensitivity," *Energy & Environmental Science,* 2018.

[127] J. r. m. Werner *et al.*, "Complex Refractive Indices of Cesium–Formamidinium-Based Mixed-Halide Perovskites with Optical Band Gaps from 1.5 to 1.8 eV," *ACS Energy Letters,* vol. 3, no. 3, pp. 742-747, 2018.

[128] K. A. Bush *et al.*, "Thermal and Environmental Stability of Semi-Transparent Perovskite Solar Cells for Tandems Enabled by a Solution-Processed Nanoparticle Buffer Layer and Sputtered ITO Electrode," *Advanced Materials,* 2016.

[129] K. A. Bush *et al.*, "Compositional Engineering for Efficient Wide Band Gap Perovskites with Improved Stability to Photoinduced Phase Segregation," *ACS Energy Letters,* 2018.

[130] P. Löper *et al.*, "Complex refractive index spectra of CH3NH3PbI3 perovskite thin films determined by spectroscopic ellipsometry and spectrophotometry," *The journal of physical chemistry letters,* vol. 6, no. 1, pp. 66-71, 2014.

[131] B. Conings *et al.*, "A universal deposition protocol for planar heterojunction solar cells with high efficiency based on hybrid lead halide perovskite families," *Advanced Materials,* vol. 28, no. 48, pp. 10701-10709, 2016.

[132] H. T. Nguyen, F. E. Rougieux, B. Mitchell, and D. Macdonald, "Temperature dependence of the band-band absorption coefficient in crystalline silicon from photoluminescence," *Journal of Applied Physics,* vol. 115, no. 4, p. 043710, 2014.

[133] J. M. Siqueiros, R. Machorro, and L. E. Regalado, "Determination of the optical constants of MgF 2 and ZnS from spectrophotometric measurements and the classical oscillator method," *Applied optics,* vol. 27, no. 12, pp. 2549-2553, 1988.

[134] S. C. Baker-Finch and K. R. McIntosh, "Reflection of normally incident light from silicon solar cells with pyramidal texture," *Progress in Photovoltaics: Research and Applications,* vol. 19, no. 4, pp. 406-416, 2011.

[135] M. T. Hörantner and H. J. Snaith, "Predicting and optimising the energy yield of perovskite-on-silicon tandem solar cells under real world conditions," *Energy & Environmental Science,* vol. 10, no. 9, pp. 1983-1993, 2017.

[136] H. Fujiwara, *Spectroscopic ellipsometry: principles and applications*. John Wiley & Sons, 2007.

[137] H. Fujiwara, M. Kondo, and A. Matsuda, "Real-time spectroscopic ellipsometry studies of the nucleation and grain growth processes in microcrystalline silicon thin films," *Physical Review B,* vol. 63, no. 11, p. 115306, 2001.

[138] D. E. Aspnes, "Optical properties of thin films," *Thin solid films,* vol. 89, no. 3, pp. 249-262, 1982.

[139] J. Lee, P. Rovira, I. An, and R. Collins, "Rotating-compensator multichannel ellipsometry: Applications for real time Stokes vector spectroscopy of thin film growth," *Review of scientific instruments,* vol. 69, no. 4, pp. 1800-1810, 1998.

[140] D. Bruggeman, "The calculation of various physical constants of heterogeneous substances. I. The dielectric constants and conductivities of mixtures composed of isotropic substances," *Annals of Physics,* vol. 416, pp. 636-791, 1935.

[141] B. Johs and J. S. Hale, "Dielectric function representation by B-splines," *physica status solidi (a),* vol. 205, no. 4, pp. 715-719, 2008.

[142] G. Jellison Jr and F. Modine, "Parameterization of the optical functions of amorphous materials in the interband region," *Applied Physics Letters,* vol. 69, no. 3, pp. 371-373, 1996.

[143] M. Shirayama *et al.*, "Optical transitions in hybrid perovskite solar cells: ellipsometry, density functional theory, and quantum efficiency analyses for CH 3 NH 3 PbI 3," *Physical Review Applied,* vol. 5, no. 1, p. 014012, 2016.

[144] J. Guerra *et al.*, "Determination of the complex refractive index and optical bandgap of CH3NH3PbI3 thin films," *Journal of Applied Physics,* vol. 121, no. 17, p. 173104, 2017.

[145] G. Yin, C. Merschjann, and M. Schmid, "The effect of surface roughness on the determination of optical constants of CuInSe2 and CuGaSe2 thin films," *Journal of Applied Physics,* vol. 113, no. 21, p. 213510, 2013.

[146] M. van Eerden *et al.*, "Optical Analysis of Planar Multicrystalline Perovskite Solar Cells," *Advanced Optical Materials,* vol. 5, no. 18, 2017.

[147] J. M. Ball *et al.*, "Optical properties and limiting photocurrent of thin-film perovskite solar cells," *Energy & Environmental Science,* vol. 8, no. 2, pp. 602-609, 2015.

[148] K. Jäger, L. Korte, B. Rech, and S. Albrecht, "Numerical optical optimization of monolithic planar perovskite-silicon tandem solar cells with regular and inverted device architectures," *Optics Express,* vol. 25, no. 12, pp. A473-A482, 2017.

[149] M. T. Hörantner *et al.*, "The Potential of Multijunction Perovskite Solar Cells," *ACS Energy Letters,* vol. 2, no. 10, pp. 2506-2513, 2017.

[150] S. Manzoor *et al.*, "Improved light management in planar silicon and perovskite solar cells using PDMS scattering layer," *Solar Energy Materials and Solar Cells,* vol. 173, pp. 59-65, 2017.

[151] D. Liu *et al.*, "Impact of Ultrathin C60 on Perovskite Photovoltaic Devices," *ACS nano,* vol. 12, no. 1, pp. 876-883, 2018.

[152] S. Albrecht *et al.*, "Towards optical optimization of planar monolithic perovskite/silicon-heterojunction tandem solar cells," *Journal of Optics,* vol. 18, no. 6, p. 064012, 2016.

[153] Z. Yu and Z. Holman, "Predicting the Efficiency of the Silicon Bottom Cell in a Two-Terminal Tandem Solar Cell," *IEEE PVSC,* 2017.

[154] S. Rühle, "Tabulated values of the Shockley–Queisser limit for single junction solar cells," *Solar Energy,* vol. 130, pp. 139-147, 2016.

[155] T. Kirchartz and U. Rau, "What Makes a Good Solar Cell?," *Advanced Energy Materials,* vol. 8, no. 28, p. 1703385, 2018.

[156] S. R. Kurtz, P. Faine, and J. Olson, "Modeling of two-junction, series-connected tandem solar cells using top-cell thickness as an adjustable parameter," *Journal of Applied Physics,* vol. 68, no. 4, pp. 1890-1895, 1990.

[157] S. De Wolf *et al.*, "Organometallic halide perovskites: sharp optical absorption edge and its relation to photovoltaic performance," *The journal of physical chemistry letters,* vol. 5, no. 6, pp. 1035-1039, 2014.

[158] Z. Yu, J. V. Carpenter, and Z. Holman, "Techno-economic viability of silicon-based tandem photovoltaic modules in the United States," *Nature Energy*, 2018.

[159] Z. Song *et al.*, "A technoeconomic analysis of perovskite solar module manufacturing with low-cost materials and techniques," *Energy & Environmental Science*, vol. 10, no. 6, pp. 1297-1305, 2017.

[160] M. Cai, Y. Wu, H. Chen, X. Yang, Y. Qiang, and L. Han, "Cost-performance analysis of perovskite solar modules," *Advanced Science*, vol. 4, no. 1, p. 1600269, 2017.

[161] N. L. Chang, A. W. Yi Ho-Baillie, P. A. Basore, T. L. Young, R. Evans, and R. J. Egan, "A manufacturing cost estimation method with uncertainty analysis and its application to perovskite on glass photovoltaic modules," *Progress in Photovoltaics: Research and Applications*, vol. 25, no. 5, pp. 390-405, 2017.

[162] J. Tong *et al.*, "Carrier lifetimes of> 1 μs in Sn-Pb perovskites enable efficient all-perovskite tandem solar cells," *Science*, vol. 364, no. 6439, pp. 475-479, 2019.

[163] N. K. Noel *et al.*, "Highly Crystalline Methylammonium Lead Tribromide Perovskite Films for Efficient Photovoltaic Devices," *ACS Energy Letters*, vol. 3, no. 6, pp. 1233-1240, 2018.

[164] C. Liu, W. Li, C. Zhang, Y. Ma, J. Fan, and Y. Mai, "All-inorganic CsPbI2Br perovskite solar cells with high efficiency exceeding 13%," *Journal of the American chemical society*, vol. 140, no. 11, pp. 3825-3828, 2018.

[165] H. Tan *et al.*, "Dipolar cations confer defect tolerance in wide-bandgap metal halide perovskites," *Nature communications*, vol. 9, no. 1, p. 3100, 2018.

[166] D. Luo *et al.*, "Enhanced photovoltage for inverted planar heterojunction perovskite solar cells," *Science*, vol. 360, no. 6396, pp. 1442-1446, 2018.

[167] W. S. Yang *et al.*, "Iodide management in formamidinium-lead-halide–based perovskite layers for efficient solar cells," *Science*, vol. 356, no. 6345, pp. 1376-1379, 2017.

[168] D. Zhao *et al.*, "Efficient two-terminal all-perovskite tandem solar cells enabled by high-quality low-bandgap absorber layers," *Nature Energy*, vol. 3, no. 12, p. 1093, 2018.

[169] R. Prasanna *et al.*, "Band gap tuning via lattice contraction and octahedral tilting in perovskite materials for photovoltaics," *Journal of the American Chemical Society*, vol. 139, no. 32, pp. 11117-11124, 2017.

[170] J. Benick *et al.*, "High-efficiency n-type HP mc silicon solar cells," *IEEE journal of photovoltaics*, vol. 7, no. 5, pp. 1171-1175, 2017.

[171] Z. Yang *et al.*, "Enhancing electron diffusion length in narrow-bandgap perovskites for efficient monolithic perovskite tandem solar cells," *Nature communications*, vol. 10, no. 1, pp. 1-9, 2019.

[172] H. Fujiwara *et al.*, "Determination and interpretation of the optical constants for solar cell materials," *Applied Surface Science*, vol. 421, pp. 276-282, 2017.

[173] C. V. Cushman, B. A. Sturgell, A. C. Martin, B. M. Lunt, N. J. Smith, and M. R. Linford, "Eagle XG® glass, optical constants from 230 to 1690 nm (0.73-5.39 eV) by spectroscopic ellipsometry," *Surface Science Spectra*, vol. 23, no. 1, pp. 55-60, 2016.

[174] Y. Zhibin *et al.*, "Enhancing Electron Diffusion Length in Narrow-bandgap Perovskites for Efficient Monolithic Perovskite Tandem Solar Cells (under review)."

[175] M. Despeisse *et al.*, "Optimization of thin film silicon solar cells on highly textured substrates," *physica status solidi (a)*, vol. 208, no. 8, pp. 1863-1868, 2011.

[176] M. Despeisse *et al.*, "Resistive interlayer for improved performance of thin film silicon solar cells on highly textured substrate," *Applied Physics Letters*, vol. 96, no. 7, p. 073507, 2010.

[177] R. Dewan, M. Marinkovic, R. Noriega, S. Phadke, A. Salleo, and D. Knipp, "Light trapping in thin-film silicon solar cells with submicron surface texture," *Optics Express*, vol. 17, no. 25, pp. 23058-23065, 2009.

[178] K. A. Bush *et al.*, "Minimizing Current and Voltage Losses to Reach 25% Efficient Monolithic Two-Terminal Perovskite–Silicon Tandem Solar Cells," *ACS Energy Letters*, vol. 3, no. 9, pp. 2173-2180, 2018.

[179] H. Shen *et al.*, "In situ recombination junction between p-Si and TiO2 enables high-efficiency monolithic perovskite/Si tandem cells," *Science advances*, vol. 4, no. 12, p. eaau9711, 2018.

[180] Z. Song, C. Chen, C. Li, R. A. Awni, D. Zhao, and Y. Yan, "Wide-bandgap, low-bandgap, and tandem perovskite solar cells," *Semiconductor Science and Technology*, vol. 34, no. 9, p. 093001, 2019.

[181] S. Manzoor *et al.*, "Optical modeling of wide-bandgap perovskite and perovskite/silicon tandem solar cells using complex refractive indices for arbitrary-bandgap perovskite absorbers," *Optics express*, vol. 26, no. 21, pp. 27441-27460, 2018.

[182] M. Carmody *et al.*, "Single-crystal II-VI on Si single-junction and tandem solar cells," *Applied physics letters*, vol. 96, no. 15, p. 153502, 2010.

[183] Z. J. Yu, K. C. Fisher, B. M. Wheelwright, R. P. Angel, and Z. C. Holman, "PVMirror: a new concept for tandem solar cells and hybrid solar converters," *IEEE Journal of Photovoltaics*, vol. 5, no. 6, 2015.

[184] P. Koirala *et al.*, "Through-the-glass spectroscopic ellipsometry for analysis of CdTe thin-film solar cells in the superstrate configuration," *Progress in Photovoltaics: Research and Applications*, vol. 24, no. 8, pp. 1055-1067, 2016.

[185] J. Chen *et al.*, "Through-the-glass spectroscopic ellipsometry of CdTe solar cells," in *Photovoltaic Specialists Conference (PVSC), 2009 34th IEEE*, 2009, pp. 001748-001753: IEEE.

[186] J. Chen, "Spectroscopic ellipsometry studies of II-VI semiconductor materials and solar cells," University of Toledo, 2010.

[187] M. M. Junda *et al.*, "A Versatile Optical Model Applied to CdTe and CdSe 1–y Te y Alloys: Sensitivity to Film Composition and Relative Defect Density," in *2018 IEEE 7th World Conference on Photovoltaic Energy Conversion (WCPEC)(A Joint Conference of 45th IEEE PVSC, 28th PVSEC & 34th EU PVSEC)*, 2018, pp. 1902-1905: IEEE.

[188] P. Koirala, "Multichannel spectroscopic ellipsometry for CdTe photovoltaics: from materials and interfaces to solar cells," 2015.

[189] C. Gueymard, *SMARTS2: a simple model of the atmospheric radiative transfer of sunshine: algorithms and performance assessment*. Florida Solar Energy Center Cocoa, FL, 1995.

APPENDIX A

LOCAL ANGLE ADF EVOLUTION AFTER HITTING THE TOP SURFACE

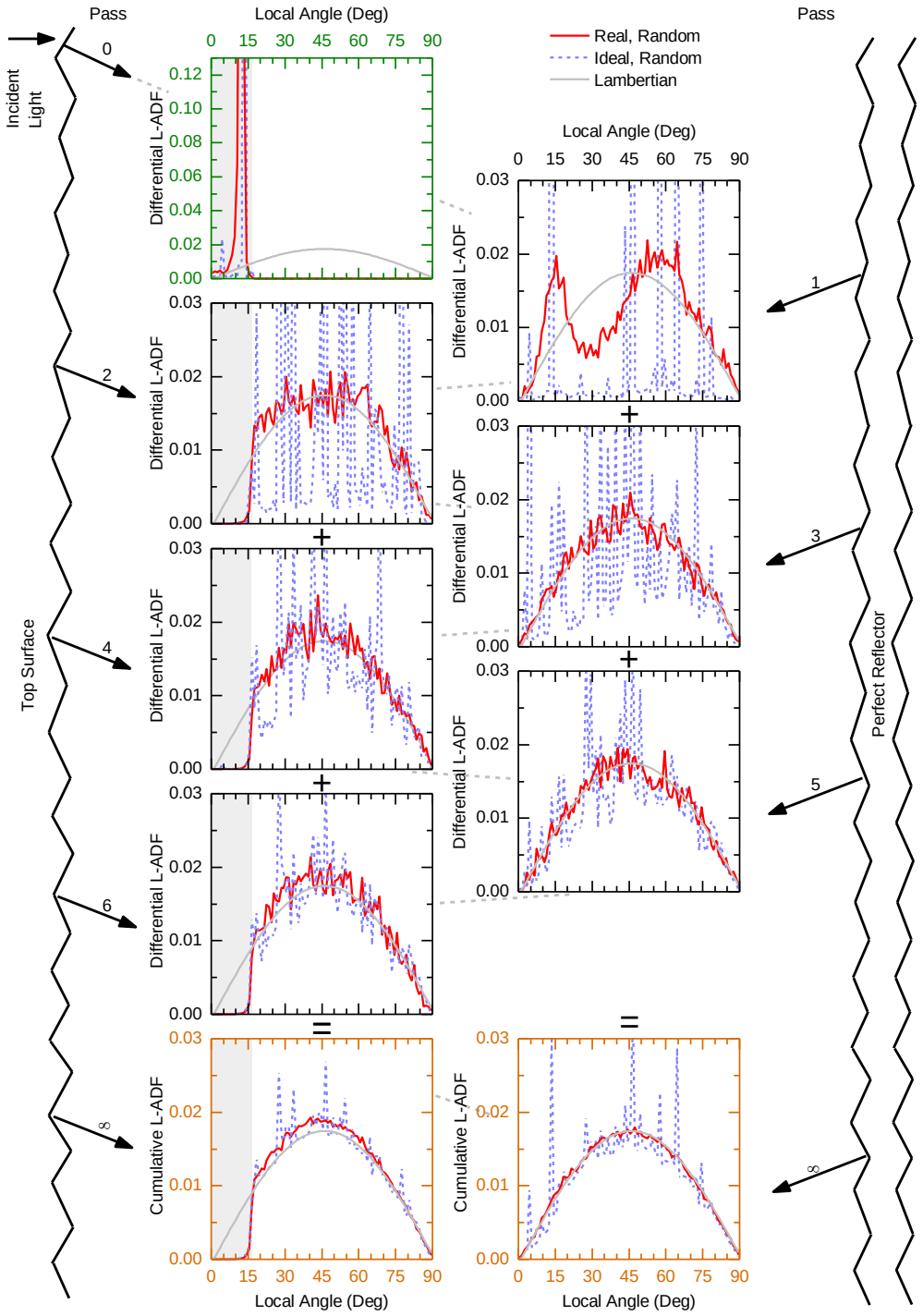

Figure A-1. Shows the local angle ADF evolution versus passes of trapped light rays for normally incident light. This figure is exactly the same as Fig. 7 with only one exception: the local angle ADF reported at the top surface is after the light rays have hit the top surface. Therefore, the light rays that fall into the escape cone, which spans between 0^{o} to 16^{o}, escapes out of the wafer.

APPENDIX B

SUPPLEMENTARY MATERIAL FOR OPTICAL MODELING OF WIDE-BANDGAP PEROVSKITE AND PEROVSKITE/SILICON TANDEM SOLAR CELLS USING COMPLEX REFRACTIVE INDICES FOR ARBITRARY-BANDGAP PEROVSKITE ABSORBERS

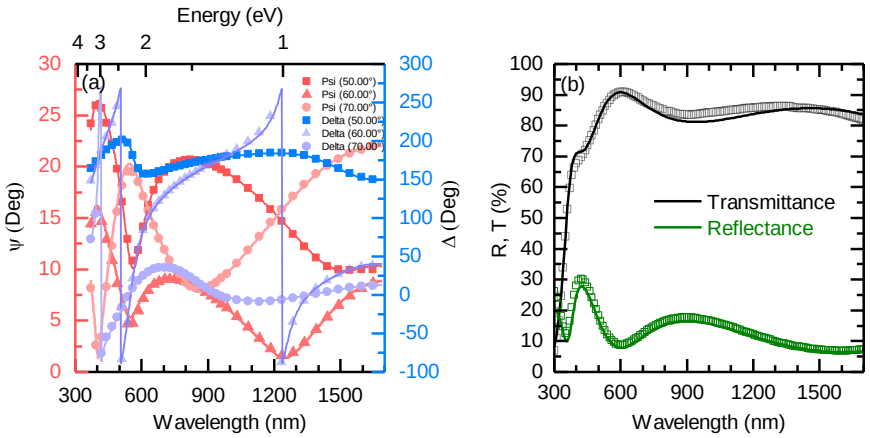

Figure B-1. Simulated (line) and measured (symbol) (a) multi-angle spectroscopic ellipsometry spectra and (b) reflectance and transmittance spectra of a front ITO film on glass.

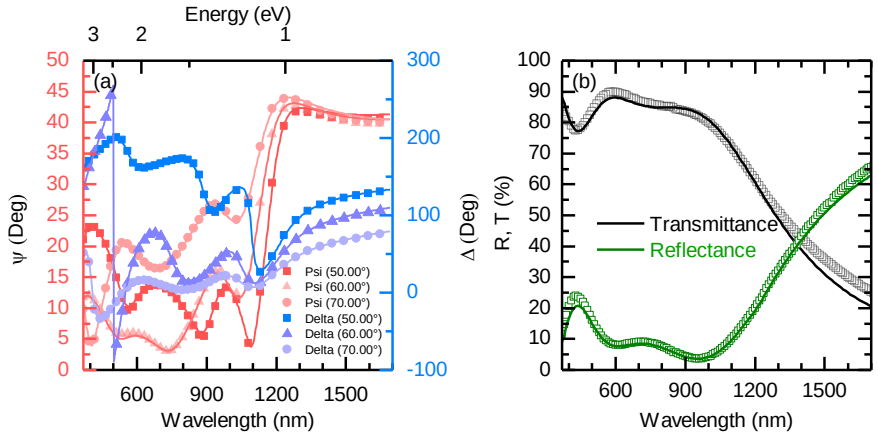

Figure B-2. Simulated (line) and measured (symbol) (a) multi-angle spectroscopic ellipsometry spectra and (b) reflectance and transmittance spectra of a rear ITO film on glass.

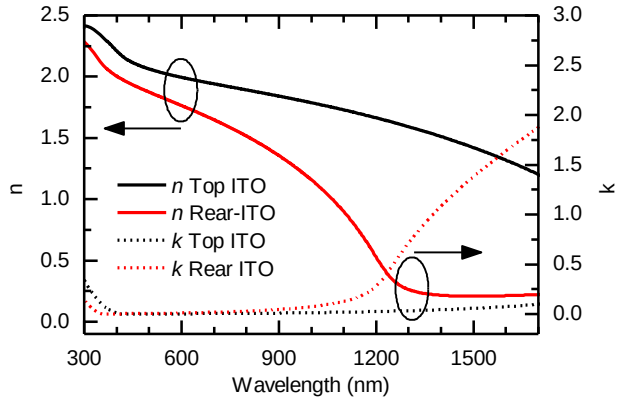

Figure B-3. Optical constants of the front and rear ITO as determined from fitting ellipsometry and spectrophotometry data.

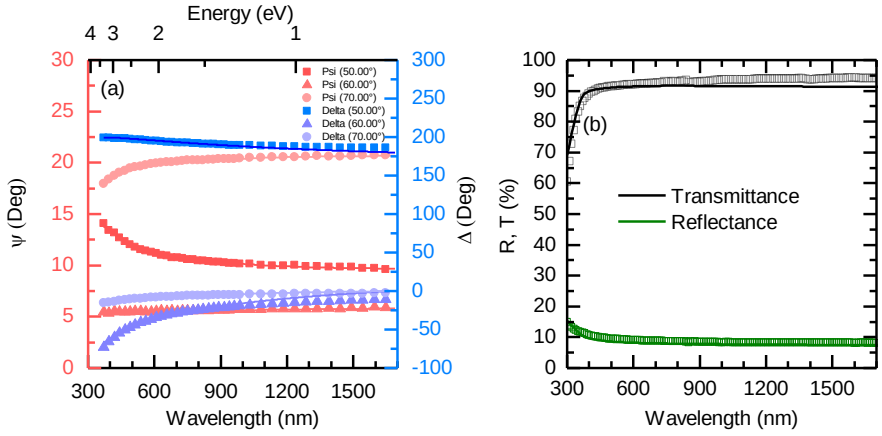

Figure B-4. Simulated (line) and measured (symbol) (a) multi-angle spectroscopic ellipsometry spectra and (b)reflectance and transmittance spectra of a SnO_2 film on glass.

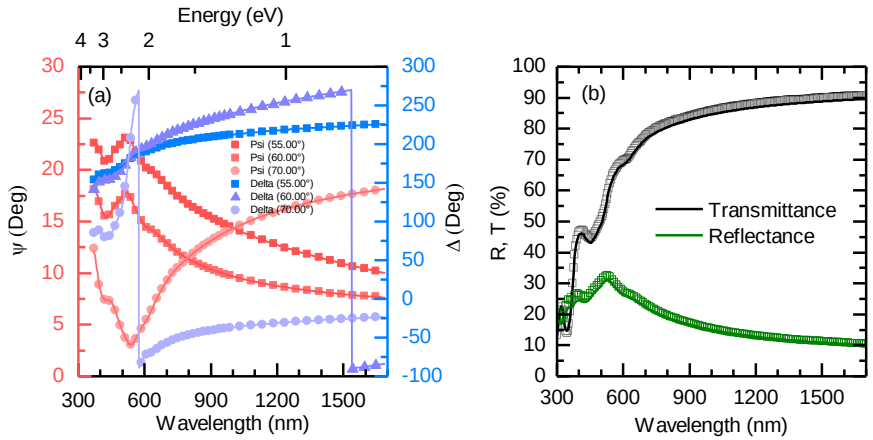

Figure B-5. Simulated (line) and measured (symbol) (a) multi-angle spectroscopic ellipsometry spectra and (b) reflectance and transmittance spectra of a C_{60} film on glass.

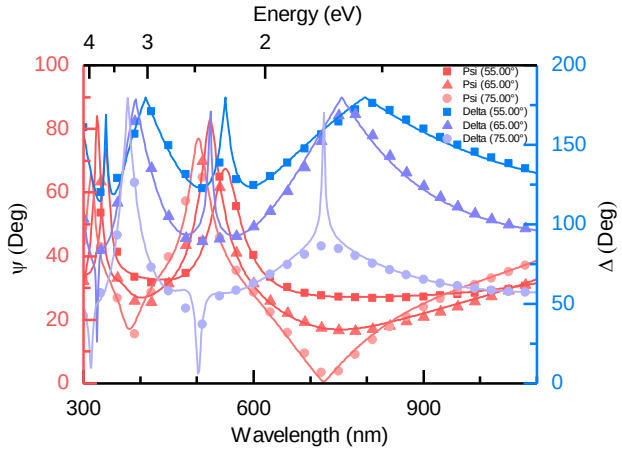

Figure B-6. Simulated (line) and measured (symbol) (a) multi-angle spectroscopic ellipsometry spectra and (b) reflectance and transmittance spectra of a NiO_x film on SiO_2-coated single-side-polished silicon.

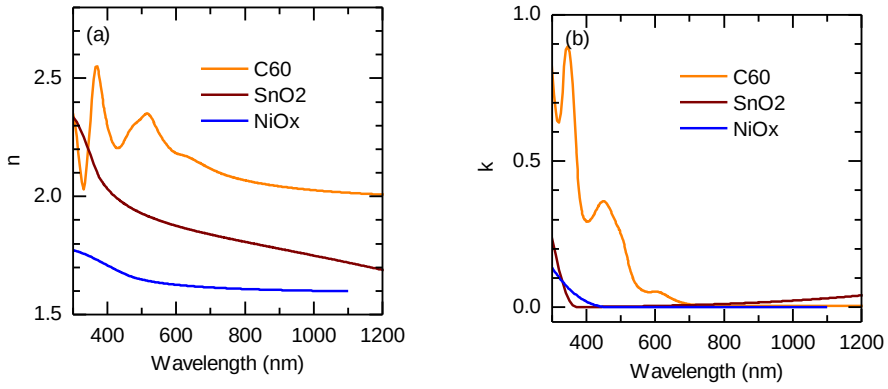

Figure B-7. Optical constants of SnO_2, C_{60}, and NiO_x as determined from fitting ellipsometry and spectrophotometry data.

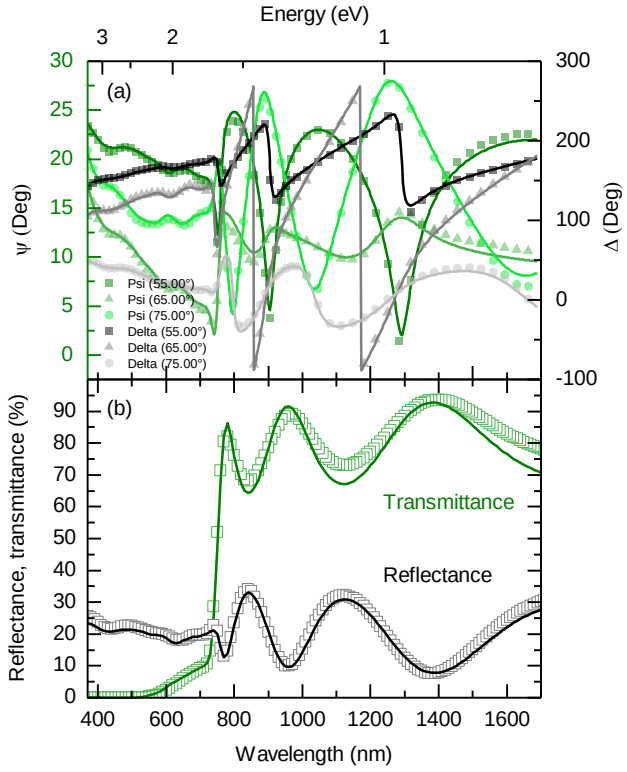

Figure B-8. Simulated (line) and measured (symbol) (a) multi-angle spectroscopic ellipsometry spectra and (b) reflectance and transmittance spectra of a Cs17/Br17 film on quartz.

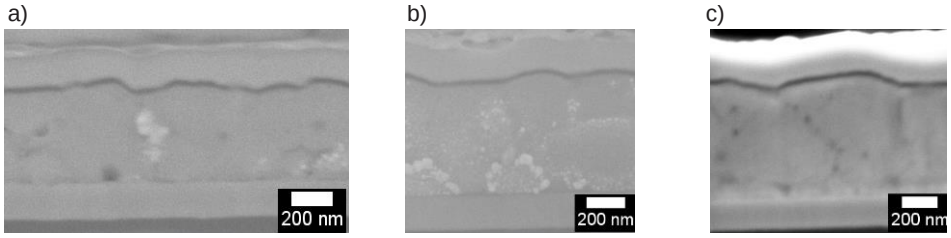

Figure B-9. Cross-sectional SEM images of (a) MAPI, (b) Cs17/Br17, and (c) Cs25/Br20 single-junction solar cells for thickness estimation of the front ITO, rear ITO, and perovskite layers.

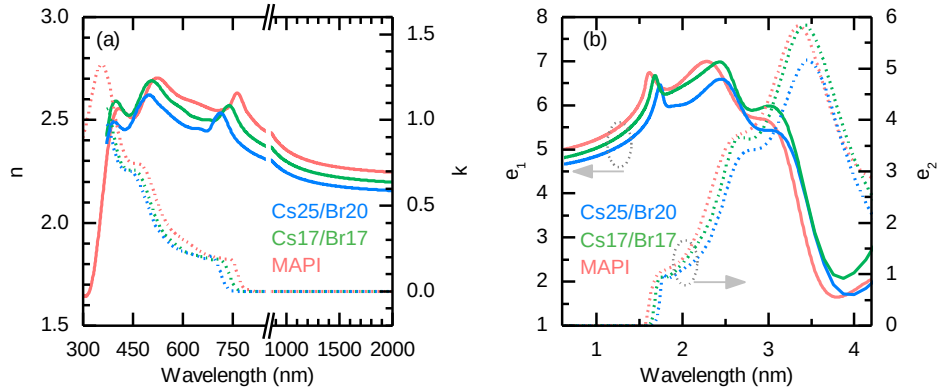

Figure B-10. (a) Optical constants for MAPI, Cs17/Br17, and Cs25/Br20 perovskites resulting from B-Spline fitting (b) Dielectric function of MAPI, Cs17/Br17, and Cs25/Br20 perovskites resulting from Tauc-Lorentz oscillator fitting.

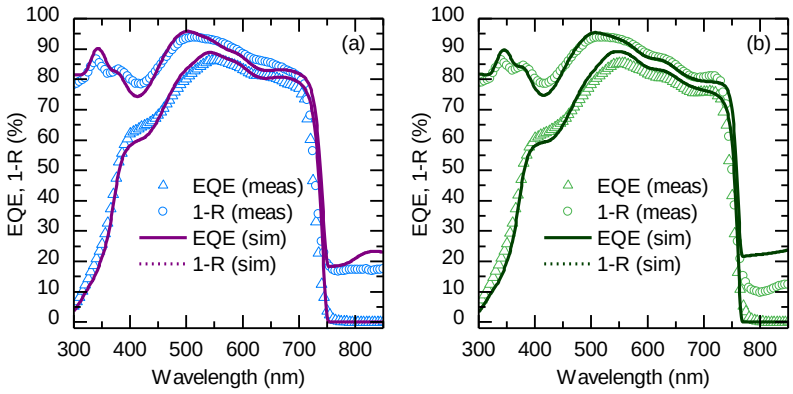

Figure B-11. Simulated (line) and measured (symbol) total absorptance (1-R) and EQE of (a) Cs25/Br20 and (b) Cs17/Br17 cells with detached silver reflectors. The simulations were performed with translated refractive indices from Eq. (1).

Table B-1. Values of dielectric function parameters of the best fits to ellipsometric and spectrophotometric data for perovskite films. d_s is the surface roughness layer thickness, d_b is the bulk perovskite thickness, E_g is the bandgap of the perovskite, and *Amp* is the strength, *Br* is the breadth, and *Eo* is the energy position of the oscillator, all given in eV.

Model Parameter	Cs25/Br20	Cs17/Br17	MAPI
MSE	11.83	11.51	9.39
$\mathbf{d_s}$	15.05	13.45	10.36
$\mathbf{d_b}$	591.34	585.71	420.20
$\boldsymbol{\varepsilon_\infty}$	1 (fixed)	1 (fixed)	1 (fixed)
$\mathbf{E_g}$ (eV)	1.665	1.615	1.557
$\mathbf{Amp_1}$ (eV)	63.225	54.104	76.546
$\mathbf{Br_1}$ (eV)	0.172	0.179	0.164
$\mathbf{Eo_1}$ (eV)	1.708	1.652	1.571
$\mathbf{Amp_2}$ (eV)	17.201	16.203	11.888
$\mathbf{Br_2}$ (eV)	1.012	0.984	0.809
$\mathbf{Eo_2}$ (eV)	2.623	2.565	2.504
$\mathbf{Amp_3}$ (eV)	12.725	14.089	9.965
$\mathbf{Br_3}$ (eV)	0.865	0.906	0.767
$\mathbf{Eo_3}$ (eV)	3.485	3.439	3.334

Table B-2. Thicknesses (in nm) estimated from the cross-sectional SEM images shown in Fig. 19.

Layer	Cs25/Br20	Cs17/Br17	MAPI
Front ITO	148.6	147.1	157.1
Perovskite	640.8	602.3	460.2
Rear ITO	164.5	171	172

Table B-3. Thicknesses (in nm) used in the SunSolve optical simulations of single-junction perovskite solar cells.

Layer	Cs25/Br20	Cs17/Br17	MAPI
Front ITO	152.5	155.3	159.5
SnO_2	9.5	8.5	8
C_{60}	22	23.3	22.1
Perovskite	650	594.9	461.6
NiO_x	20	20	19.90
Rear ITO	165	175	175
Glass	10^6	10^6	10^6
DetachedAg	300	300	300

Table B-4. Thicknesses (in nm) used in the SunSolve optical simulations of perovskite/silicon tandem solar cells.

Layer	Perovskite/Si tandem
MgF_2	150
Front ITO	150
SnO_2	9
C_{60}	10
Perovskite	Varied
NiO_x	20
Intermediate ITO	20
a-Si:H(n)	4
a-Si:H(i)	6
c-Si	250,000
a-Si:H(i)	6
a-Si:H(p)	11
Rear ITO	170
Ag	200

APPENDIX C

SUPPLEMENTARY MATERIAL FOR EFFICIENCY POTENTIAL OF PEROVSKITE/PEROVSKITE TANDEM SOLAR CELLS BASED ON PRESENT ABSORBERS

Experimental methods

Sample fabrication

Single junction narrow-bandgap perovskite cells were fabricated on patterned ITO glass substrates which were cleaned by sonication in acetone and isopropyl alcohol for 30 min followed by UV ozone treatment for 20 min. Next PEDOT:PSS solution was spin-coated onto the ITO substrates at 5000 rpm for 30 s and annealed at 150 °C for 10 min in ambient environment. After this the substrates were transferred into the glovebox where Cs5/MA45/Sn50 perovskite was deposited from a 1.2–2.1 M solution prepared from 0.45 mol MAI, 0.5 mol FAI, 0.05 mol CsI, 0.55 mol PbI_2, 0.5 mol SnI_2 and 0.05 SnF_2 mixed in 3:7 volume ratio of DMSO and DMF solvent. The solution is filtered through 0.22 μm polytetrafluoroethylene (PTFE) filter. A 50 μL of solution was spin-coated for 30 s followed by dropping of 0.3 mL of PCBM solution in toluene (1 mg mL^{-1}) onto the spinning substrate after 10 s had elapsed. This was followed by 100 °C anneal for 10 min. The thickness was controlled by tuning the concentration of precursor solution and spin coating speed. Finally, 20 nm C_{60}, 6 nm BCP and 80 nm Cu were thermally evaporated to finish the fabrication of single junction narrow-bandgap perovskite cells. A complete description of fabrication of 2T terminal perovskite/perovskite tandem is given in [171].

For ellipsometry single layers of Cs5/MA45/Sn50, Cs40/Br35, C_{60}, PEDOT:PSS, SnO_2 and PTAA were deposited on Eagle Glass using the procedures described above and in [171].

Sample characterization

Perovskite-on-glass samples were characterized in air in reflectance mode with rotating compensator, M2000 spectroscopic ellipsometer equipped with NIR extension from J. A.

Woollam Company. Measurements were performed at five (55°, 60°, 65°, 70°, 75°) angles of incidence in the wavelength range of 191–1690 nm. A diffusive scotch tape from 3M was attached to the back of the samples to suppress substrate backside reflections. Transmittance and reflectance of the ellipsometry samples were measured with PerkinElmer Lambda 950 instrument at 0° and 7° angle of incidence respectively. Fitting of SE and spectrophotometric spectra was performed with CompleteEase software from J. A. Woollam Company.

Same methodology outlined above was used to gather SE and spectrophotometric spectra of front ITO, C_{60}, PEDOT:PSS, PTAA, BCP and SnO_2 that were deposited on glass to obtain their refractive indices to be used in optical simulations later. The data were fitted with single Tauc-Lorentz oscillator and a Drude term for front ITO, with one Tauc-Lorentz oscillator for SnO_2, with three Tauc-Lorentz oscillators for C_{60}, with Cauchy dispersion formula for glass substrate and B-Splines were used to fit PEDOT:PSS and BCP data. Roughness layer with 50%/50% volume fractions of air and layer being fitted was included in the fits. Collected spectra, fits and extracted optical constants are given in Figures C-5-7.

Zeiss Auriga FIB-SEM instrument was used to collect scanning electron microscope (SEM) images of the surface of perovskite films and was also used to mill into the perovskite devices and collect cross-sectional images to determine the thicknesses of the perovskite, front ITO, and PEDOT:PSS layers. Surface morphology of the perovskite films was also studied with atomic force microscopy (AFM). Scanning was done with Bruker Multimode instrument in air with a silicon pyramidal tip in tapping mode.

EQE and reflectance of the single junction perovskite cells were measured in the wavelength range of 300–1100 nm with PV Measurements QX10 tool and PerkinElmer Lambda 950 spectrophotometer respectively.

Optical simulations

Optical simulations of single-junction perovskite shown in Figure C-3, were performed in SunSolve software from PV Lighthouse that combines Monte-Carlo based ray-tracer with thin-film solver [109]. Simulations were carried out for normal incidence of light with AM1.5G solar spectrum [189]. Refractive indices of all the layers required as input to SunSolve, were determined using SE as described above and are shown in Figure C-7. Thicknesses of front ITO, PEDOT:PSS and perovskite, also required as input to SunSolve were determined from cross-sectional SEM image of the cell shown in Figure C-4. Perovskite thickness was allowed to vary within 10% of its thickness determined from SEM image to account for thickness non-uniformity. For thinner layers, C_{60}, BCP and Cu, however it was difficult to determine their thickness from SEM image. For them their target thicknesses shown in Figure C-4 were used with 5% variation allowed. Final thicknesses used in the simulation are shown in Table C-2. All layers were assumed to be perfectly planar and coherent. Simulated EQE is the 100% absorptance in the perovskite layer thus is the result of assuming perfect carrier collection. This assumption is justified for thin absorbers with long diffusion lengths.

2T perovskite/perovskite tandems shown in Figure 6-4, were also simulated with SunSolve at normal incidence of light with AM1.5G solar spectrum [189]. Refractive indices of each layer were determined with SE and are shown in Figure C-7 but were taken from literature for MgF_2 [133]. Starting thicknesses of each layer were taken to be their

target thicknesses shown in Figure 6-4a. Perovskite absorber thickness was allowed to vary within 10% of their target thickness and other layers varied 5%. Final thickness values used in the simulations are shown in Table C-3. All layers were assumed perfectly planar and coherent because all layers are thinner compared to coherence length of the sunlight. Base-angle of random pyramids in Figure 6-4 was 51.5° and in case of Figure 6-4b all subsequent layers on the pyramids were assumed conformal to the texture. Complex refractive indices for wide-bandgap perovskite in the bandgap range of 1.56–1.9 eV were generated according to approach presented in [135]. Similar to single junction perovskite, 100% carrier collection is assumed for each sub-cell of tandem and for the same reason.

1. Sample characterization

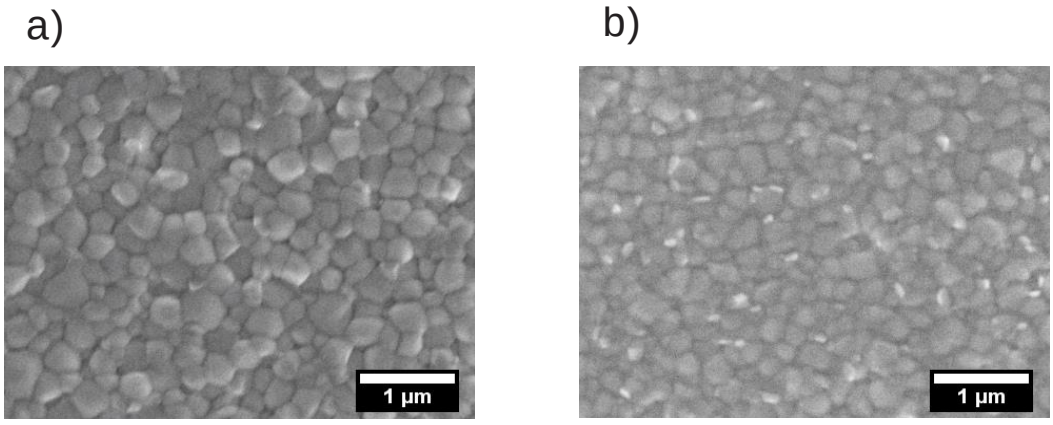

Figure C-1. Scanning electron microscope (SEM) image of the surface of Cs5/MA45/Sn50-narrow-bandgap (a) and Cs40/Br35-wide-bandgap (b) perovskite films analyzed with SE.

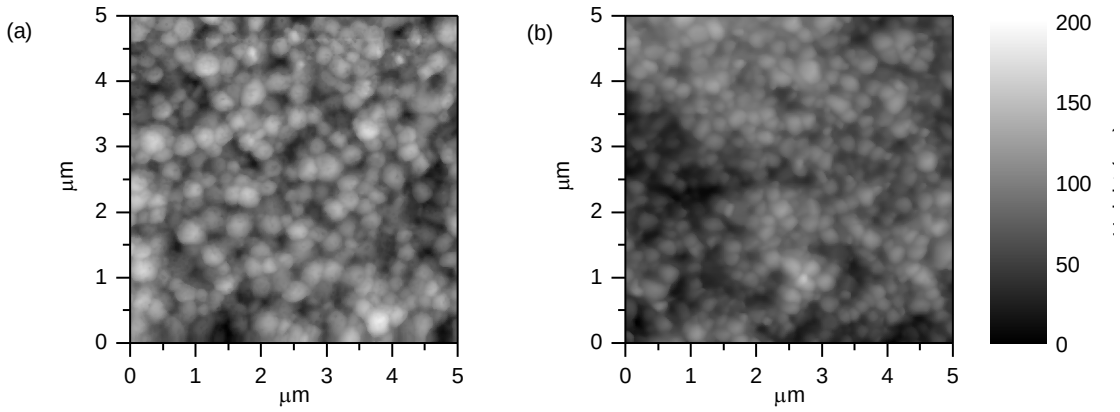

Figure C-2. Atomic force microscope (AFM) image of the surface of Cs5/MA45/Sn50-narrow-bandgap (a) and Cs40/Br35-wide-bandgap (b) perovskite films analyzed with SE.

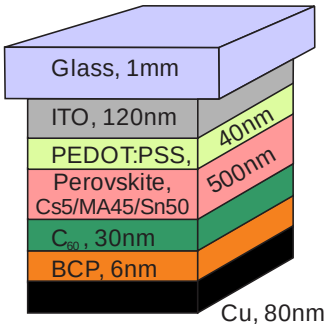

Figure C-3. Schematic showing single junction, Cs5/MA45/Sn50-narrow-bandgap perovskite solar cell fabricated to validate the refractive indices of Cs5/MA45/Sn50 perovskite.

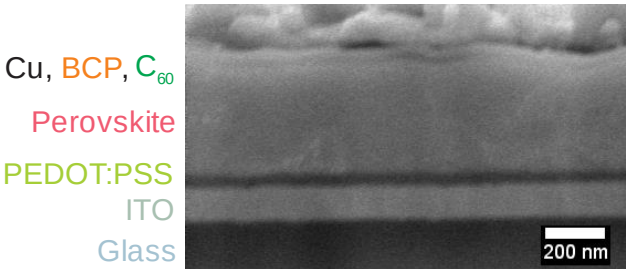

Figure C-4. Cross-sectional SEM image of Cs5/MA45/Sn50 single junction solar cell for thickness estimation of the front ITO, PEDOT:PSS, and perovskite layer.

Table C-1. Thicknesses (in nm) estimated from cross-sectional image shown in Figure C-4.

Layer	Thickness
ITO	115
PEDOT:PSS	38
Perovskite	490

2. Ellipsometry of contact and electrode layers and their optical constants

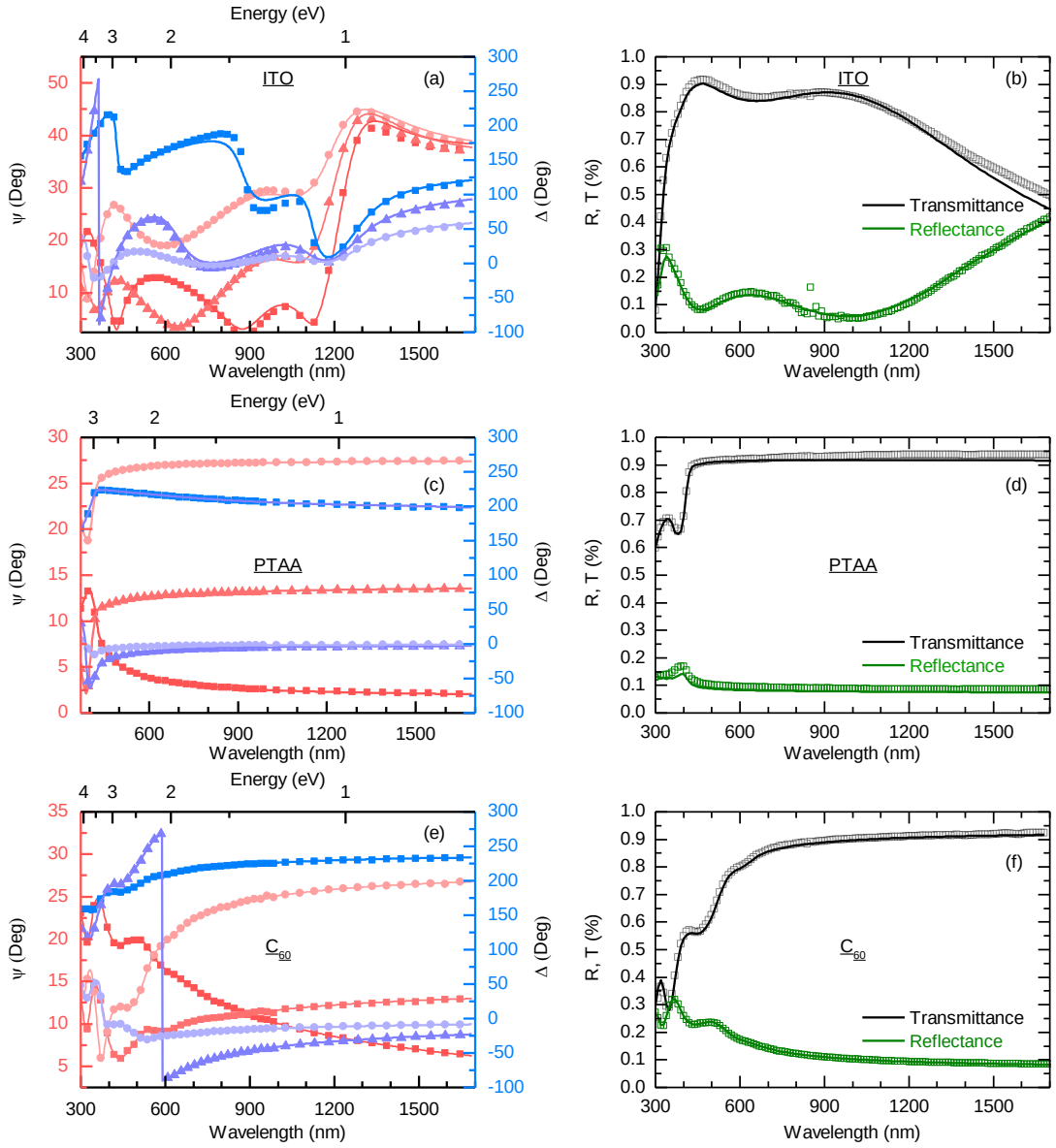

Figure C-5. Simulated (line) and measured (symbol) (a,c,e) SE spectra (b,d,f) reflectance and transmittance spectra of front ITO, PTAA and C_{60} on glass.

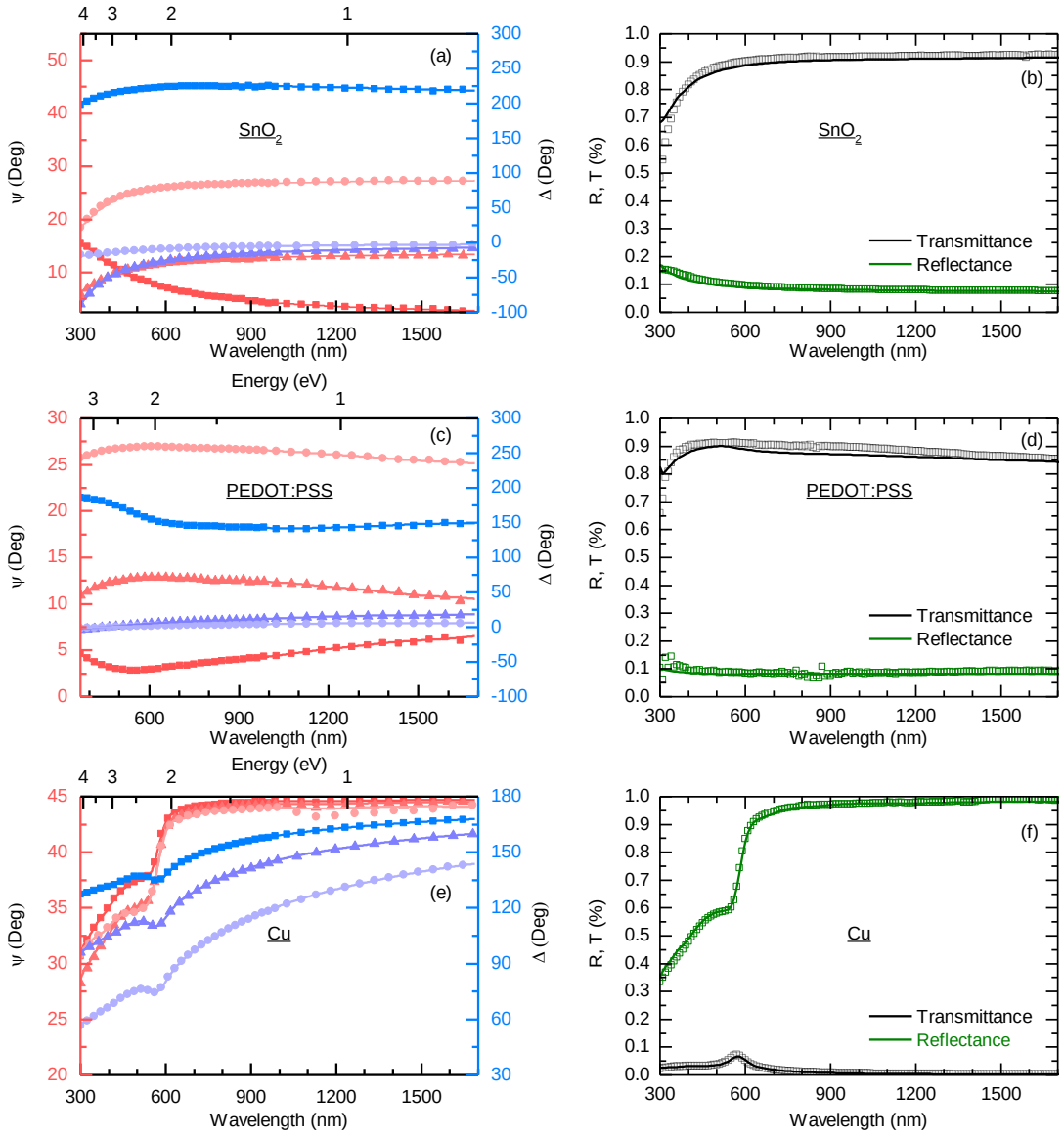

Figure C-6. Simulated (line) and measured (symbol) (a,c,e) SE spectra (b,d,f) reflectance and transmittance spectra of SnO_2, PEDOT:PSS and Cu on glass.

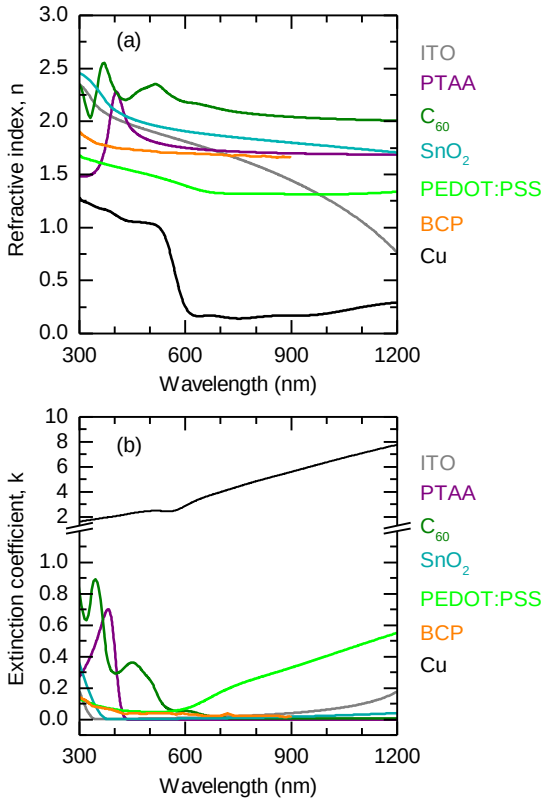

Figure C-7. Refractive indices of different layers used in single junction and tandem simulations and as determined from SE and spectrophotometry. (a) refractive index (b) extinction coefficient.

3. Thicknesses used in the optical simulations

Table C-2. Thicknesses (in nm) used in the SunSolve optical simulations of single junction perovskite solar cell shown in Figure C-3.

Layer	Thickness
Glass	1 mm
ITO	115
PEDOT:PSS	37
Perovskite	485
C_{60}	30
BCP	6
Cu	80

Table C-3. Thicknesses (in nm) used in the SunSolve optical simulations of perovskite/perovskite tandem solar cells.

	Figure 6-3	Figure 6-5	Figure 6-6
Layer	Thickness	Thickness	Thickness
Glass	1 mm	1 mm	1 mm
ITO	115	115	60
PTAA	5	5	5
Perovskite	365 nm Eg = 1.8 eV	200-590 nm Eg = 1.8 eV	100-690 nm Eg = 1.56–1.9 eV
C_{60}	10	10	10
SnO_2	10	10	10
ITO	10	10	10
PEDOT:PSS	30	30	20
PTAA	5	5	5
Perovskite (E_g=1.22 eV)	1000 nm	200-1480 nm	1500 nm
C_{60}	20	20	20
BCP	6	6	6
Cu	80	80	80

4. 2-diode model for efficiency calculation of tandems

To calculate the efficiency of 2T perovskite/perovskite tandem we adopted a 2-diode model for both top- and bottom-cell, given by Equation S1.

$$J(V) = J_{sc} + \left(J_{o,rad} + J_{o,SRH}\right)\left(1 - e^{\frac{qV}{k_B T}}\right) \quad \text{(S1)}$$

Here k_B is the Boltzmann constant, T is the temperature. All calculations are performed with T=300 K. The emission loss associated with radiative recombination is modeled with an ideality factor of 1 and corresponding saturation current is represented by the term $J_{o,rad}$. In addition to take into account the bulk and interface recombination in top- and bottom-cell we include a $J_{o,SRH}$ term to represent the associated recombination current-density. Again we assume an ideality factor of 1. Short-current density (J_{sc}), taking device structure,

parasitic absorptance and reflectance losses into account, is calculated through simulations in SunSolve. Resulting EQEs from SunSolve are used to calculate $J_{o,rad}$ according to Equation S2.

$$J_{o,rad} = q \int_0^\infty EQE(E)\phi_{bb}(E)\, dE \tag{S2}$$

Here q is the elementary charge of electron and ϕ_{bb} is the black body spectrum given by Equation S3.

$$\phi_{bb}(E,T) = \frac{2\pi E^2}{h^3 c^2} \frac{1}{\left[\mathrm{e}\left(\frac{E}{k_B T}\right) - 1\right]} \tag{S3}$$

h is the Planck's constant, c is the speed of light and T is the temperature. Finally $J_{o,SRH}$ for top- and bottom-cell is assigned a value that lowers the corresponding bandgap single-junction cell efficiency to 75% of its detailed-balance efficiency. In the end to calculate the tandem efficiency, top- and bottom-cell each are represented by separate Equation S1. Then these two equations are solved simultaneously taking limiting sub-cell current to be the tandem current and assuming current-matched condition to find the top- and bottom-cell voltage and tandem current-density at maximum power point. Tandem efficiency is then defined as:

$$\eta = \frac{J_{mpp,tandem}\left(V_{mpp,top} + V_{mpp,bottom}\right)}{P_{IN}} \tag{S4}$$

Here P_{IN}, $J_{mpp,tandem}$ and $V_{mpp,top}$, $V_{mpp,bottom}$ are incident power, tandem current-density and voltage of top- and bottom-cell at maximum power point, respectively.